Interlaminar Reinforcement of Carbon Fiber Composites from Unidirectional Prepreg Utilizing Aligned Carbon Nanotubes

By

Diana Lewis

MS. Mechanical Engineering
University of New Hampshire, 2007

SUBMITTED TO THE DEPARTMENT OF AERONAUTICS AND ASTRONAUTICS IN PARTIAL FULFILLMENT OF THE REQUIREMENTS FOR THE DEGREE OF

MASTER OF SCIENCE IN AERONAUTICS AND ASTRONAUTICS
AT THE
MASSACHUSETTS INSTITUTE OF TECHNOLOGY

February 2016

Signature of the Author:……
Department of Aeronautics and Astronautics
January 26, 2015

Certified by:……
Brian L. Wardle
Professor of Aeronautics and Astronautics
Thesis Supervisor

Accepted by: ……
Paulo C. Lozano
Associate Professor of Aeronautics and Astronautics
Chair, Graduate Program Committee

Interlaminar Reinforcement of Carbon Fiber Composites from Unidirectional Prepreg Utilizing Aligned Carbon Nanotubes

By

Diana Lewis

Submitted to the department of Aeronautics and Astronautics on January 28, 2016 in partial fulfillment of the requirements for the degree of Master of Science in Aeronautics and Astronautics

ABSTRACT

Advanced laminated composites suffer from a lack of out-of-plane strength and toughness, leading to delamination and other types of interlaminar failure. Aligned carbon nanotubes (A-CNTs) placed at the interlayer between plies of an aerospace grade carbon fiber reinforced plastic composite (CFRP) have been shown to increase interlaminar toughness while improving laminate strength. While this architecture, known as 'nanostitch', has proven beneficial, morphological changes in the A-CNT layer and their effect on the composite properties has not been studied. This thesis explores the effect of varying the A-CNT height and the layup technique on the resulting interlaminar region morphology and static short beam strength (SBS) in shear, of a quasi-isotropic layup using Hexcel IM7/8552 carbon fiber aerospace composite prepreg. In addition, fatigue testing was performed on a selected A-CNT height to generate a SBS fatigue life curve. Interface morphology and laminate damage were imaged via optical and scanning electron microscopy of cross-sections and crack surfaces, and micro-computed tomography was used to generate 3D reconstructions of some coupons. Results from static testing indicate that the A-CNT reinforcement of the interlaminar region increase the SBS by 8.5%, regardless of height (in the 5-65 micron range studied) or the two different layup techniques. This indifference to forest morphology is attributed to damage primarily occurring outside of the reinforced area, indicating that the interlaminar region is sufficiently reinforced by all A-CNT heights considered. Fatigue-life data shows a threefold increase in lifespan for the A-CNT reinforced material. All A-CNT forests affected the interface morphology, increasing the average interlayer thickness by inducing resin agglomerations near the CNT layer. This agglomeration results from resin-rich defects in the original prepreg material. Ancillary tasks involved in generating this thesis included inventing a method of measuring A-CNT forest height using an optical microscope, introducing water into the CNT growth process and controlling the furnace starting temperature to stabilize the height, altering the layup method to generate desired morphologies, and proposing a 'hot-load' system for the furnace to increase the CNT forest production tenfold.

Thesis Supervisor: Brian L. Wardle
Title: Professor of Aeronautics and Astronautics

Contents

List of Figures

List of Tables

Nomenclature

a	amplitude of sine wave used to quantify waviness (nm)
d_2	Numerical modifier of $\bar{R}$ to obtain standard deviation
F^*	Calculated test value to compare variance
$F_{0.01,2,2}$	Critical value of F that indicates significance for 99% confidence of a two-specimen vs. two-specimen variance comparison
G_0	Mode 1 fracture toughness of unreinforced material (J/m^2)
G_{ss}	Steady-state Mode 1 fracture toughness including toughening mechanisms (J/m^2)
L	Line length of nanotube measured in SEM image (pixels)
L_{CNT}	Length of CNT pullout (nm)
N	Cycle count in fatigue testing
p	Position along length of nanotube calculated from sine wave (nm)
r	Nanotube radius (nm)
R	Run number used when determining influencing parameters on forest growth
$\bar{R}$	Statistical estimate of variance from two samples
sL	Straight length of nanotube measured in SEM image (pixels)
t	Growth time (s)
T	Starting temperature (°C)
v_{CNT}	Volume fraction of CNTs
w	Water bubbler setpoint (arbitrary units, rotameter scale)
x	Horizontal position of chip from center of furnace (mm)
Z	Vertical position of chip in furnace (1 or 4)
z	Vertical position along nanotube (nm)
λ	Wavelength (nm)
τ_c	Interfacial shear strength in pull-out fracture model (MPa)

Acronym

A-CNT	Aligned carbon nanotube
CFRP	Carbon fiber reinforced plastic
CNT	Carbon nanotube
CCVD	Catalytic chemical vapor deposition
CVD	Chemical vapor deposition
GNPT	Guaranteed non-porous Teflon
ILSS	Interlaminar shear strength
MFC	Mass flow controller
MicroCT	Micro-computed tomography
OOA	Out of autoclave
RTM	Resin transfer molding
SBS	Short beam strength
SE	Standard error
SEM	Scanning electron microscopy
SST	Shear stress transport (option in modeling CVD flow)
TEM	Transmission electron microscopy
VARTM	Vacuum assisted resin transfer molding

1 Introduction

Advanced fiber composites, notably carbon fiber reinforced plastics (CFRPs) have become ubiquitous in the aerospace industry. Due to their high specific strength and modulus, they are desirable in applications where weight reduction has a significant impact on performance and fuel economy [1]. CFRPs are typically produced in a laminate configuration, with thin (~100μm) layers (plies) of carbon fiber built up to a desired thickness and bound together with a polymer. While the freedom to change the fiber orientation in every ply allows for tailorable in-plane properties, the multiple layers are left vulnerable in the through-plane direction. Interfaces between plies contain only the relatively weak and brittle polymer, which leads to various issues including delamination. The weak interfaces in advanced laminated composites have been mitigated by many methods, such as z-pinning, stitching and tufting, however macroscopic methods often degrade in-plane properties of the resulting laminate, making their use a tradeoff that is beneficial only in certain applications [2] [3] [4] [5].

Carbon nanotubes have similar measured mechanical properties to carbon fibers [6] [7] [8] [9] [10] [11], however they exist with diameters as small as 0.4nm [12] and can grow to tailorable lengths as long as 550 millimeters [13]. This unique nanoscale fiber provides the opportunity to create a multi-scale composite material that is strong and tough in all three planes. The nanotubes are small enough to interdigitate between the carbon fibers without disturbing their in-plane orientation, making them an ideal prospect for reinforcing the aforementioned weak interlaminar regions in advanced fiber composites if the morphology, particularly alignment and packing, can be successfully controlled.

Work done by Garcia [14], Blanco [15] and de Villoria [16] indicate that using aligned carbon nanotubes in the interfaces of CFRPs improves Mode I and II toughness and can result in 3D improvements in strength by strengthening and toughening the interface. This thesis will extend that work and aims to discover the influence of the aligned carbon nanotube's structure on the resulting composite's property, namely short beam shear strength.

2 Background

Carbon fiber reinforced plastic (CFRP) composites have made a significant contribution to aerospace structures in the last 40 years, due to their high specific strength. The ability to reduce weight while maintaining the strength of a structure has precipitated the move from aluminum and titanium to these advanced materials. As carbon fiber composites have become well known, their use in aircraft structures has increased. The airbus A350 and Boeing 787 Dreamliner are both comprised of over 50% by weight CFRP [1].

2.1 Aerospace Laminated Carbon Fiber Reinforced Plastic Composites

This high strength to weight ratio is due to the unique properties of CFRPs. These composites consist of two materials; carbon fiber and a polymer resin. The carbon fiber is produced through carbonization of either pitch-based or (usually) PAN (polyacrylonitrile) based filaments [17]. These carbon fibers are extremely strong in the axial direction, up to 6 GPa [18] and have diameters in the 5-7 micron range [19] [20]. To utilize these microscale, strong fibers, a few thousand are collected into a tow for handleability, then those are used to make flat sheets, woven materials, or used in filament winding or braiding. These carbon fibers are then impregnated with a polymer resin to bind them together. For aerospace applications, this resin is typically an epoxy.

Production of parts from carbon fiber usually requires forming on a mold. The carbon fibers are manually applied to the mold layer by layer (hand layup), or filament wound or braided onto the forms. The orientation of fibers in each layer can be changed arbitrarily to optimize the final laminate's properties (the direction of highest strength is in the axis of the carbon fiber). Frequently, a layup will alternate between a series of angles to result in a quasi-isotropic laminate (a laminate that behaves elastically like an isotropic material in-plane).

The polymer resin is most typically combined with these fibers in one of three ways. First, each layer of carbon fiber can be soaked with resin as it is applied to the mold; each layer is compressed before the next one is put on. Second, the resin can be infused in a technique called resin transfer molding (RTM), where the whole part is laid up, sealed in the mold and the polymer is infused by pumping resin into the mold. A variation on this technique, vacuum-assisted RTM (VARTM) uses a vacuum to help degas, compress and infuse the resin into the part. Finally, sheets of carbon fiber (either woven or unidirectional) can be purchased pre-impregnated with uncured resin, called prepreg. Prepreg is laid up in the same manner as a wet-layup, compressing each layer of prepreg to the stack as it is applied. Once the layup is complete, it is placed into a vacuum bag and cured under elevated pressure and temperature, usually in an autoclave, although there are materials that are designed for out-of-autoclave (OOA) curing. The high pressure combined with vacuum reduces the amount of voids in the resulting laminate, among other benefits.

Typically prepreg is used in aerospace composites, and frequently a quasi-isotropic layup is produced to create a material that has similar in-plane stiffness properties in all directions. Due to the layered structure of the composite material and the alternating directions of carbon fiber in each layer, there are resin-rich regions in each interface between the plies (Figure 2-1). This resin rich region results primarily from the alternating angles of carbon fibers; they are unable to mesh together, creating a distinct boundary between the layers.

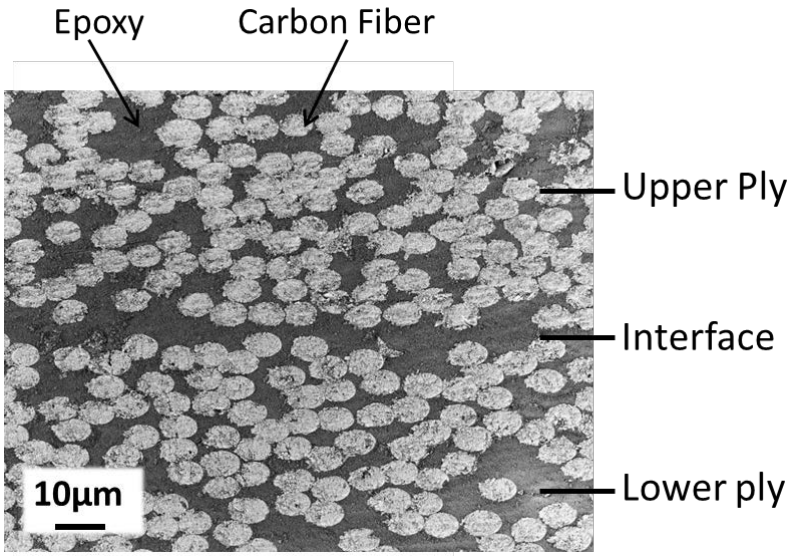

Figure 2-1: SEM image of an interface in a carbon fiber composite.

The through-thickness direction of CFRP laminates is relatively weak compared to the in-plane properties, due to the lack of carbon fibers aligned in that direction. In particular, the resin-rich interfaces are a prime spot for failure, as they not only do not have the benefit of aligned carbon fibers, but they also lack out-of-plane carbon fibers that can act as crack arrestors. One of the most common failures for carbon fiber composites is delamination, caused by the ability of cracks to propagate relatively unimpeded along this weak interface. Many methods have been developed to mitigate this failure mode, and more are being developed.

2.2 Carbon Fiber Composite Interlaminar Reinforcement

Because of the weakness in the out-of-plane direction (z-direction) from the resin-rich interlaminar regions that lead to delamination, a number of techniques have been developed to reinforce the z-direction of the material. Macroscopic z-reinforcement methods such as z-pinning, stitching, and tufting are common, as well as using toughenners or micro/nano scale reinforcement of the epoxy to delay the onset and prevent propagation of microcracks that lead to delamination [4].

Macroscopic methods such as z-pinning and stitching have a drawback that prevents them from ubiquitous use. In particular, these methods necessarily displace and break the in-plane carbon fibers as they pass through the material. This leads to undesirable degradation of in-plane strength. Despite this shortcoming, these methods have found success in composite joints and areas where fasteners and/or out-of-plane forces exist [2].

Microscopic reinforcement of the epoxy, in particular the use of toughеners in the resin, are ubiquitously used in the aerospace industry. Frequently these formulations of epoxy with specific toughеners are trade secrets, with the consumer (or graduate student) only able to find out that the epoxy is toughened, without specifications. These toughеners can form microbeads that arrest cracks. In addition, thermoplastic sheeting is sometimes interleaved with the CFRP plies to generate a thicker interface that resists delamination [21]. However, these methods are still on the micro-scale, and the use of microbeads or the thermoplastic sheeting can reduce in-plane strength due to the limitations on the packing fraction of carbon fibers in the plies reinforced with these materials.

Nanoscale reinforcements are being seen as the next evolution in composite materials. Because of their size, these nanoscale particles and fibers can reinforce the epoxy matrix without displacing the microscale carbon fibers. Research has been conducted using nanoscale materials including nano-graphene and silica platelets, alumina nanofibers, carbon nanofibers and carbon nanotubes [22] [23] [24] [25] [26] [27]. The nanoscale reinforcement utilized in this thesis is aligned carbon nanotubes.

2.3 Carbon Nanotubes (CNTs)

2.3.1 Carbon Nanotube Structure and Properties

Carbon nanotubes are nanometer-diameter cylinders made of carbon. This carbon is pi-pi bonded and its structure resembles that of a sheet of rolled-up graphene. The way that this graphene is rolled results in different chiralities of carbon nanotubes, which have significance for properties such as electrical conductivity. If, for instance, the carbon nanotube is rolled up such that the carbon atoms result in a zigzag pattern oriented around the diameter of the carbon nanotube, this structure is called a ‘zigzag’ nanotube and is semiconducting. If the graphene sheet is rolled up such that the carbon nanotubes form an alternating plateau type pattern around the diameter, the carbon nanotube is an ‘armchair’ nanotube and is metallic (conductive). For the purpose of this thesis, the chirality of the carbon nanotube is not important as mechanical properties are not significantly affected by these small structure differences. Carbon nanotubes can consist of a single wall, or have multiple walls (concentric cylinders) of this graphene structure (see Figure 2-2). This thesis focuses on multiwalled carbon nanotubes.

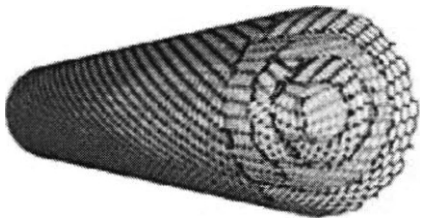

Figure 2-2: Idealized Multi-walled CNT [28].

Multiwalled carbon nanotubes are strong and light, with measured strengths up to 100GPa and a modulus of about 1TPa [6], with a density of only 1.46 g/cc [29] [30]. These properties make them ideally suited for reinforcement of composite materials used in aerospace applications. In addition, the length of carbon nanotubes can be tailored by the growth process, to be anywhere from a few nanometers to 55 centimeters in length [13].

2.3.2 Growth of Aligned Carbon Nanotubes

While there are many methods of growing carbon nanotubes (eg. arc-discharge and laser ablation), the one utilized in this work is a substrate-bound catalytic chemical vapor deposition (CCVD) process that results in an aligned morphology.

On its face, the substrate-bound CCVD method for growing carbon nanotubes is simple. A thin layer of a metal catalyst such as iron is deposited on a substrate, becoming a metal oxide upon being exposed to ambient air. It is placed into a reaction chamber, then heated to a high temperature (500-900°C) under hydrogen to reduce the metal oxide and cause the catalyst to form nanoscale islands. Then a carbon-containing source is introduced into the reaction chamber, which decomposes on the metal surface, precipitating the carbon and growing carbon nanotubes. The carbon nanotubes are spatially confined by each other, causing growth to predominantly occur in the vertical direction. This produces an aligned morphology, called a nanotube 'forest', shown in Figure 2-3.

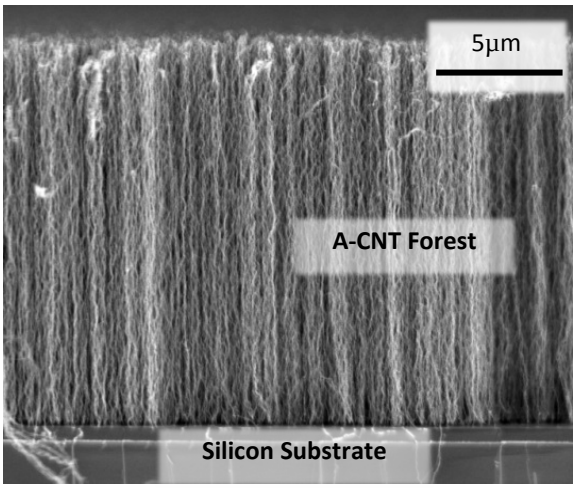

Figure 2-3: Carbon nanotube forest on a silicon substrate.

2.4 Carbon Nanotube Reinforcement of Composites

Carbon nanotubes (CNT) have been a popular research topic in the area of composite reinforcement for many years [31] [32] [33] [34] [35] [36] [37] [38] [39]. There are three main types of reinforcement; randomly dispersed in the epoxy matrix, grown or placed directly on the carbon fibers, and placing aligned carbon nanotubes between the plies to reinforce the interface.

The first type of CNT reinforcement, dispersion in the epoxy matrix, should be a good way to reinforce the entire composite material. Unfortunately, many researchers have had difficulty with dispersing the carbon nanotubes and/or infusing the resin once they've obtained dispersion. Much work has been done to prevent nanotube clustering through different surface functionalizations [40] [41] [42] [43] [44] [45], and shear mixing [46] [47], but even when that is achieved, the viscosity of the resin is greatly increased due to the high surface area of the CNTs [48]. This high viscosity causes a limit to the amount of CNTs that can be put in the resin and still allow it to penetrate the carbon fiber tows during infusion. In spite of these difficulties, in 2014 Zyvex Technologies began utilizing carbon nanotubes and nanographene in a commercially available aerospace material, citing a 195% improvement in fracture toughness and 20% improvement in interlaminar shear strength [49] [50] [51].

Another type of reinforcement grows carbon nanotubes directly on carbon fibers [52] [53] [54] [33] [55] [56], colloquially named 'fuzzy fiber' in MIT's aligned carbon nanotube work [57]. This type of reinforcement circumvents the issues with dispersing the carbon nanotubes, as they are already distributed along a fiber in a uniform configuration. In addition, because the nanotubes are aligned, capillary forces increase the ability of the resin to infiltrate the carbon fiber, rather than reduce it as in the random case [58]. Many groups have attempted the growth of carbon nanotubes directly on carbon fibers, however most see a decrease in fiber strength due to the degradation of carbon fibers during the CNT growth process [59] [60] [61]. In response, a few groups have attempted to place carbon nanotubes on the carbon fibers using electrophoresis rather than growing them, which has had some degree of success.

The final type is interlaminar reinforcement using aligned carbon nanotubes in an architecture known as 'nanostitch'. Aligned carbon nanotubes forests are grown on a silicon substrate in a chemical vapor deposition process, then transferred to the prepreg plies, maintaining their aligned morphology. The aligned nature of the nanotubes allows resin infiltration by capillary forces, and is thought to bridge the interface region, reinforcing the critical interlaminar region at the nanoscale potentially without disturbing the in-plane properties of the carbon fiber composite. This is the architecture that will be studied in depth in this thesis.

2.5 Prior work with Nanostitch Architecture

The use of aligned carbon nanotubes as interlaminar reinforcement has been sparsely studied in the literature, rarely identified by the term 'nanostitch' [62] [63] [64] [65] [66]. 'Nanostitch' was coined in the first paper by MIT's NECSTLAB group [67], and will be used to describe this architecture due to this thesis being a continuation of that work.

The concept of utilizing aligned carbon nanotubes in the interface stems from the theory that the carbon nanotubes can act as nanoscale pins or stitches, which must pull out or fracture for a crack to propagate through them (Figure 2-4). Prior work presents an equation of the toughness enhancement through the pullout of small-diameter fibers [68]. It shows that the enhancement is proportional to the length and surface area of the fibers, both of which nanotubes have in abundance. Because CNTs can be grown to any length, they can be tailored to bridge the interface without creating an added interlayer, and because they are nanometers in diameter and are grown in a low density forest, they can interdigitate between the carbon fibers, preserving the carbon fibers' in-plane orientation and strength.

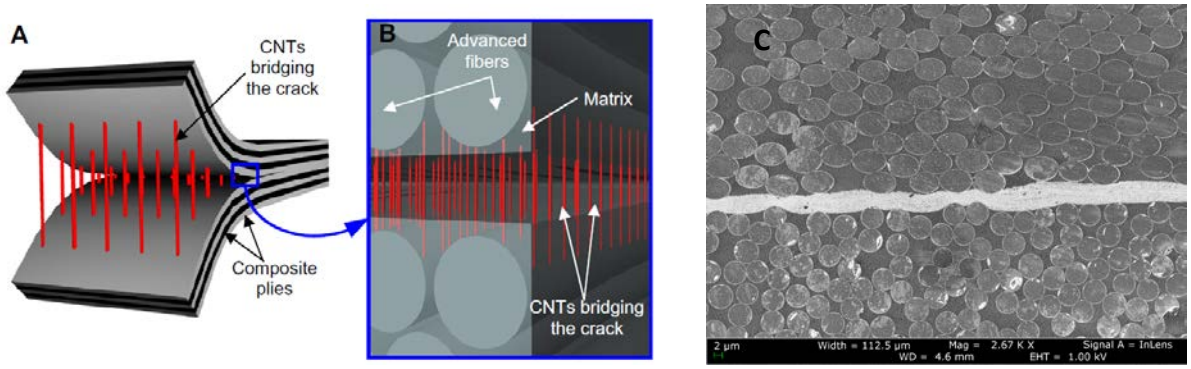

Figure 2-4: Nanostitch architecture. (A) CNTs (red) shown bridging crack faces during delamination [67] (B) Illustration of CNTs in an interface [67] (C) SEM image of aligned CNTs in an interface.

Prior work shows improvements in Mode 1 toughness, although the resulting improvements are highly variable [62] [67]. In addition, it has been shown that reinforcing the interface can lead to a 30% gain in the usable strength of the carbon fiber material (see Figure 2-5) [69].

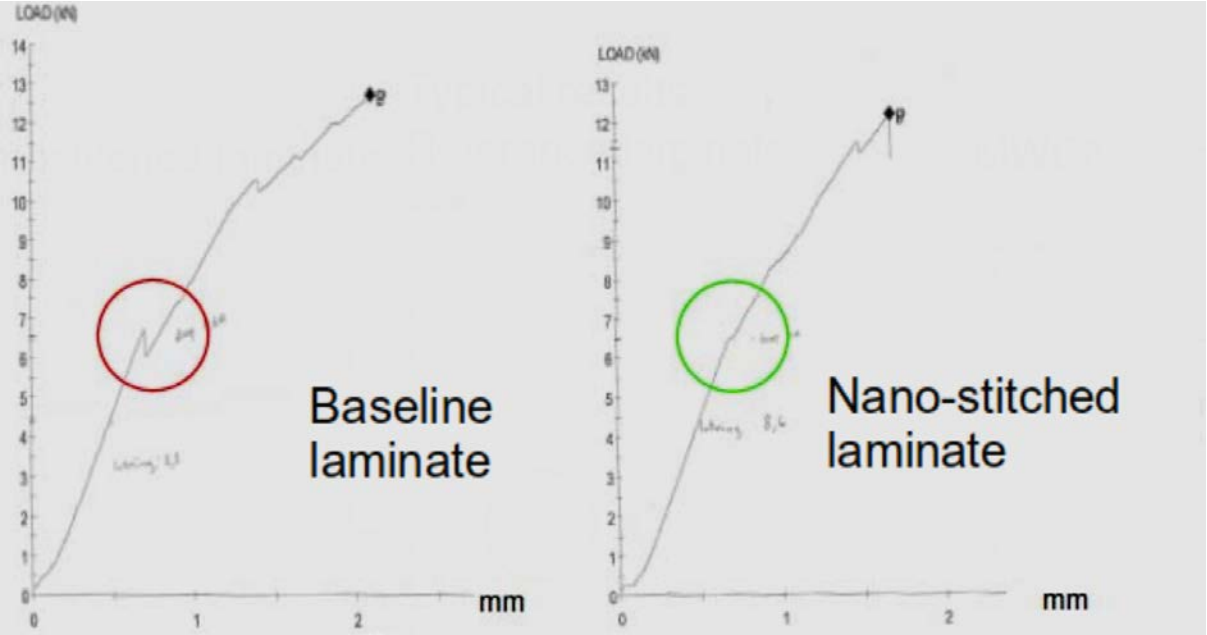

Figure 2-5: Nanostitch suppression of initial load drop (due to delamination) leads to a 30% increase in bolt-bearing strength [69].

Unanswered questions from the prior research include the effects of aligned-CNT structure changes on the resulting properties of the composite material. Changing the initial CNT structure (such as the height) or the process used to make the A-CNT reinforced composite may result in changes to the structure of the A-CNT reinforcement or the interface, and those resulting structure variations may result in alterations to the CFRP composite properties. This thesis aims to explore the differences between two layup techniques and A-CNT height variations.

3 Thesis Objectives and Outline

Aligned carbon nanotubes (A-CNTs) have been shown to improve carbon fiber composite properties across a range of mechanical testing, however morphological changes in the A-CNT and their impact on the resulting composite properties have not been studied. This work will specifically explore the effect of varying A-CNT height and the layup technique used to integrate them into composites made from unidirectional IM7/8552 Hexcel aerospace carbon fiber prepreg to establish process-structure and structure-property relations, the latter focused on interlaminar shear strength. Short beam strength (SBS) testing was chosen for the mechanical test due to its small sample size, ease of coupon manufacturing, and the ability to probe interlaminar properties. The thesis will be heavily reliant on experimental data.

The summary of the work is sectioned into four areas; synthesis of A-CNTs, composite layup, mechanical testing, and interface and damage analysis:

1. Synthesis of A-CNTs

All of the aligned CNTs used in this thesis are produced in-house by the substrate-bound catalytic chemical vapor deposition (CCVD) method. The particular "growth" recipe in our lab was previously optimized for all known control variables (substrate, catalyst metal and its layer thickness, ratios and flow rates of reaction gases, and temperature) to produce the tallest forest at the midplane of the furnace, however this thesis stabilizes this growth process to ±2µm over large 30x40mm planar areas through the use of water and control of the furnace starting temperature. Heights were varied from 5-65 microns by altering the growth time. In addition, methods were undertaken and proposed to increase the CNT forest production rate by orders of magnitude. First, a quartz boat was employed to hold ten wafer chips at a time, increasing throughput tenfold simply by being able to process ten at a time. Second, a method of hot-loading was proposed to reduce the growth cycle time from 50 minutes down to ~6 minutes, again increasing the throughput by an order of magnitude.

2. Composite Layup

In order to incorporate the A-CNTs into the prepreg, two new methods of transferring the nanotubes were developed. In both methods, the nanotubes are transferred to individual plies of unidirectional prepreg by placing the nanotube-laden wafer chips (A-CNT side down) onto the prepreg surface, then heating the prepreg to a specified temperature. Once heated, the prepreg epoxy wicks into the nanotubes, adhering them to the prepreg, and the chips can be peeled away while leaving the nanotubes behind. The first method heats the prepreg to 40°C and also uses a roller to exert pressure on the chips to aid the adherence, which results in a compressed forest morphology. The second method heats the prepreg to 60°C and allows the forest to wick in substantially before layup, resulting in a different nanostich morphology. Both

methods achieve > 90% transfer of nanotubes to the prepreg. The individual plies are then laid up in a standard process to form quasi-isotropic $[0/90/\pm45]_{2S}$ composites and autoclaved using a cure cycle according to manufacturer's specifications. Two unidirectional composites were also produced to compare to the short beam shear strength reported by the manufacturer.

3. Mechanical Testing

The completed composites are cut using a diamond bladed bandsaw into coupons for short beam shear (SBS) testing. These coupons are polished to 1200 grit, with some being polished to mirror finish for SEM imaging. Static SBS tests were performed on forest heights of 5-65 microns. Fatigue testing in the SBS configuration was performed on composites with forests of 12.5 micron average height.

4. Interface and Damage Analysis

One coupon from each sample is polished to mirror finish. These coupons are SEM imaged to analyze the interfaces and the nanotube structure in the interface. Once the coupons are tested in short beam shear, they are re-imaged to determine the effects of nanotubes on the crack locations, the extent of nanotube pullout in the regions where cracks propagate through the forest, and the percentage of the cracks that propagate in the interface and nanostitch regions versus the baseline samples. In addition, some samples were imaged in a micro-computed tomography (microCT) system to obtain a 3-dimensional image of damage. Two nanostitch and two reference samples were fatigued to 10k and 100k cycles without failure, then imaged in the microCT in an attempt to observe crack formation and propagation without the obscuring effects of damage from the ultimate failure.

4 Synthesis of Aligned Carbon Nanotubes (A-CNTs)

The carbon nanotubes for this work are grown in-house using a thermal CVD process to produce A-CNTs (forests) on a silicon wafer substrate. The process is performed in a 2" three-zone tube furnace (Lindberg BlueM – clamshell design) and utilizes iron catalyst with ethylene as the carbon source. To obtain the substrate, 150mm, <100> p-doped test-grade silicon wafers are obtained and processed in MIT's MTL (Microsystems Technology Laboratory) clean room. They are cleaned using the RCA process, and then put through a thermal oxidation step that results in a surface layer of ~500nm SiO_2. An e-beam evaporator (Temescal VES-2550) is then used to deposit the 10nm Al_2O_3/1.0nm Fe support and catalyst layers from crucibles of high-purity materials. The Al_2O_3 support layer is deposited first to limit Fe mobility during the anneal step and thereby create the nanometer-sized catalyst particles needed for CNT growth [70].

Wafers are cleaved into ten 3cm x 4cm chips (due to test size requirements), then cleaned using Scotch tape to remove any dust or other contaminants. While it is not strictly necessary to clean the chips after cleaving, the cleaving process can generate silicon dust that lands on the chip surface, and the ambient lab air contains dust particles that can contaminate the surface. These minute dust particles can interfere with growth in a radius of a few microns, which leaves pinprick holes in the resulting forest. It has been found that cleaning with Scotch tape, when done properly (ensuring no bubbles or wrinkles as the tape is laid down), does not leave any residue and works better than blowing them off with nitrogen (the lab air seems to be entrained by the gas stream and negates the cleaning effort by depositing more dust on the surface).

4.1 Original Growth Method

The original method used for growing carbon nanotube forests was adapted from prior work done from this lab [71]. The furnace and mass flow controllers are controlled with a natural-language program, Ansari, written by a former grad student [72]. The automation allows much better repeatability than manual methods, and the parameters are input using a text file written in normal language (ie. "Turn helium on" is a command). See Appendix A for growth recipe. The growth method, depicted simply in Figure 4-1, was as follows (note all temperatures in this section are reported from the furnace thermocouple reading):

1. **Load and Purge**: The furnace begins below 200°C (usually room temperature, but could be hotter from a previous run). One 3cm x 4cm wafer chip is placed in the center of the furnace. The furnace lid (top half of clamshell) is closed and the tube is sealed. All gas lines (hydrogen, helium and ethylene) are turned on at 400sccm for three minutes to purge, and then helium is flowed for five minutes at 2000sccm to ensure an inert environment.

2. **Growth Cycle**:
   a. *Catalyst anneal*: Once the helium purge is complete, helium is turned off and hydrogen is turned on at 1040sccm for 15 minutes. All three zones (note that in all cases the 3 zones are controlled together, effecting a single-zone furnace) of the furnace are set to the 680°C and ramp to that value over a period of approximately 8 minutes (±1 min, dependent on the starting temperature of the furnace), then holds at that temperature for the rest of the anneal and growth. Regardless of the ramp time, the anneal step lasts a total of 15 minutes.
   b. *Growth*: Ethylene is turned on at 400sccm for a time period specified by the desired height of the forest. For example, a 20µm tall forest would result from a 30 second growth. During this step the hydrogen continues flowing at 1040sccm, resulting in a H_2:C_2H_4 ratio of 2.6.
   c. *Delamination*: While hydrogen continues to flow, ethylene is turned off and helium is turned on at 500sccm for 5 minutes. This step is done to allow the forest to be easily removed from the chip. It is thought to etch the nanotubes at the carbon-iron interface, which effectively releases the forest from the chip.
3. **Cool-down**: The furnace is shut off once the step 2c is complete. Hydrogen is also shut off and the furnace is allowed to cool under helium. Once the furnace temperature drops to ~600°C, the furnace lid is opened to increase the cooldown rate. Once the furnace temperature reaches 225°C (10 minutes), the helium is shut off and the process is considered finished.
4. **Chip Removal**: The tube is opened and the wafer chips removed when the furnace is at or below 200°C.
5. **Bake-Out**: After a number of growths, the tube becomes blackened to opacity with excess carbon, hydrocarbons or other by-products of the reaction. It is standard practice to do a 'bake-out' cycle at the end of the day or after 4-5 growths to clean the tube. This process simply heats the furnace to 750°C while open to air. Some researchers leave the furnace at 750°C for twenty minutes, while others just heat it to 750°C then immediately cool it down again. The choice of time and temperature is somewhat arbitrary; the oxygen burns off the carbon deposits, returning the tube to its clear, 'clean' state.

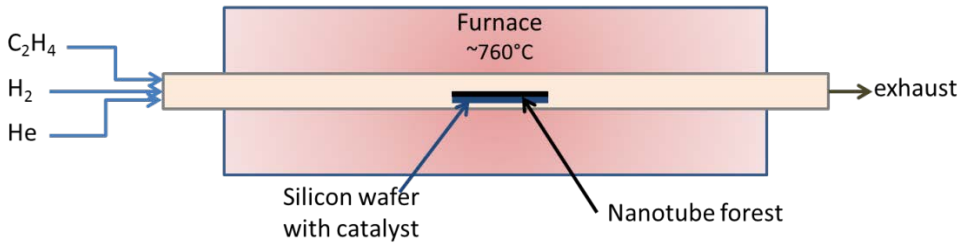

Figure 4-1: Depiction of carbon nanotube growth apparatus.

The total cycle time for a growth is 32 minutes plus growth time (~20seconds per 10µm height), not including chip loading and unloading time. A bake out-cycle takes an additional 25 minutes (plus hold time), every 5 growths. Depending on the skill of the operator, loading and unloading take 5 minutes, resulting in a total cycle time of ~45 minutes.

This method of growing carbon nanotubes created forests with variable heights growth to growth. For instance, an attempt to grow a CNT forest to 20 microns could result in heights anywhere from 3-30 microns. Because the original growth method produced these variable results at a slow rate, the process was analyzed and modified to produce more consistent forests at a higher production rate. In addition, a process for measuring the height of the forests using optical microscopy was invented to aid in the growth stabilization experiments (see section 4.4.1).

4.2 Water Addition, Position and Furnace Temperature Effects

As the thesis objective is specifically targeted at identifying the effect of forest height on its reinforcement ability, heights needed to be controlled as tightly as possible. The goal was to produce CNTs with heights within ±2µm, and the variations in the forest height from the original growth method were unacceptable. An investigation was undertaken to determine the root cause.

Most uses of A-CNTs in the lab require tall (1mm) forests, and there was some difficulty in obtaining the tallest heights. Common folklore in the lab regarding growing tall forests:

- "First growth of the day is best!"
- "Rainy days grow better than sunny days."
- "I can't get good growths in winter, so I try to grow everything I need in the summer."
- "You have to bake out the tube after a while because it gets black. Make sure you do it the night before though, otherwise you won't get a good first growth of the day."
- "Get your own tube. Other people growing in your tube will mess up the chemistry, and the tubes age over time"
- "Make sure you center the tube and your wafer chips, the growths don't get as tall if you don't."
- "It is impossible to control the height of the forests. The best you can hope for is order of magnitude."

From these observations, it was hypothesized that water and position were the main issues that could be solved through experimentation and tighter control. Quartz tube aging appeared to be a possible factor as well, but was not analyzed in this thesis.

4.2.1 Position

4.2.1.1 Horizontal Position

It is well known amongst lab members that the position of the tube within the furnace as well as the wafer chip placement inside the tube significantly affects the forest height. The tube should be precisely centered within the furnace, and to obtain tallest growths, the chip should be precisely positioned at the center of the furnace. Previous furnace characterization has shown that the growth of carbon nanotubes has been optimized to produce the maximum height at the center of the furnace. Growth about the center drops off parabolically, with no growth occurring outside of 20cm away from the center (Figure 4-2).

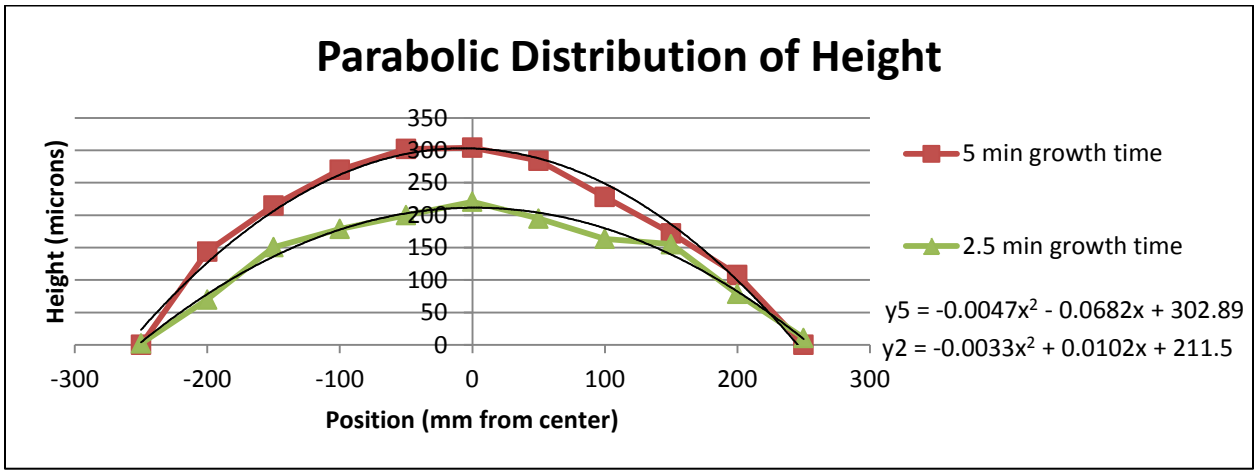

Figure 4-2: Parabolic distribution of forest height in the furnace, shown for two different growth times.

For a 15µm target growth, the parabolic distribution only results in a 2 µm drop in height from the center to ±100mm away from the center. The growths were restricted to this region to maintain a tighter distribution on the forest heights.

It should be noted that these experiments did not include any water addition, however all experiments from this point forward utilized a water bubbler to infuse ppm-level water vapor into the furnace during growths (see section 4.2.2 for details).

4.2.1.2 Vertical Position

To facilitate the timely completion of this work, it was decided to produce multiple chips per run. To that end, a custom quartz boat was ordered from G. Finkenbeiner Inc. to carry 3cm wide Si wafer chips. This boat is 200mm long and has four levels, spaced 3mm apart. It can carry five 3x4cm chips on each level, for a total of 20 chips. Unfortunately, it was quickly

discovered that all four levels could not be used, as the chips were too close together and proximity effects cause the nanotubes to grow much shorter (or not at all) on the lower chips (it is hypothesized that this is a result of restricted gas flow). Therefore only the top and bottom of the boat were utilized, allowing the growth of up to ten chips per cycle.

Previously, all chips were placed directly on the inner diameter (floor) of the tube. With the new boat, multiple levels could be used, and the height variation caused by vertical placement needed to be assessed. The minimum vertical placement with respect to the tube floor with the boat was 15mm, with a maximum of 35mm. An experiment was undertaken to determine the height variation across the different levels of the boat. Multiple wafers were placed in random arrangements (to account for the horizontal position effect) on the boat in multiple growths. On average, with no chips on the shelves above, the chips on the bottom of the boat for a 15µm target height were one micron shorter. For a 20µm target height, initial experiments showed the top of the boat averaged 18µm vs. 16µm on the bottom, a 2µm difference.

Because the height increased towards the center of the furnace and increased for growths at the top of the boat, to maximize height uniformity across the chips, four chips were positioned at a downwards angle in the boat and the center position was skipped to cancel out the two effects (See Figure 4-3). In addition, it was discovered that the forest height increased on the leading and trailing edges of chips with no adjacent chips: to eliminate this effect, small wafer scraps were added near those edges. This setup produced four uniform-height forests per run.

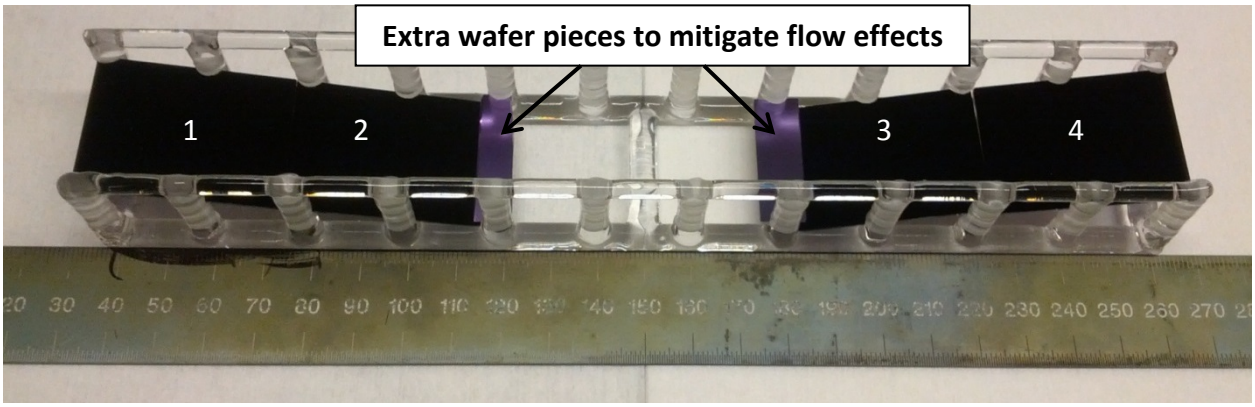

Figure 4-3: Four-chip configuration to produce maximum uniformity, shown after growth. Wafer chips are angled and extra pieces are added near chip edges to produce a uniform forest height across all chips.

When growing for this thesis, multiple heights were needed; in this case the top and bottom shelves were used fully and ten forests could be produced per run (Figure 4-4a). A leading edge spare piece was again used on both the top and bottom of the boat to mitigate the leading edge effect. This configuration led to a distribution of forest heights. On average,

with the top chips shielding the bottom ones, the bottom layer was five microns shorter than the top. Due to the increased amount of catalyst in the system, the chips towards the downstream end of the boat were shorter than upstream, and the top upstream chip was four microns taller than the rest (Figure 4-4b).

In addition to the analysis of the average height of the chip, two chips from 10-chip runs were measured at 1-2mm increments along the entire cross-section (leading to trailing edge). This gave a detailed height profile along the chip (Figure 4-4c). It was surprising to discover that a 20µm tall forest had variations from 15-25 µm, and that this variation had a consistent pattern on the two chips tested, despite being from different furnace positions and grown on different days. (It should be noted that the measurement repeatability is ±2µm, see section 4.5.2 for more details.) It is suspected that the gas flow around the chips may influence this height pattern, however modeling and many more forests need to be measured to confirm this finding.

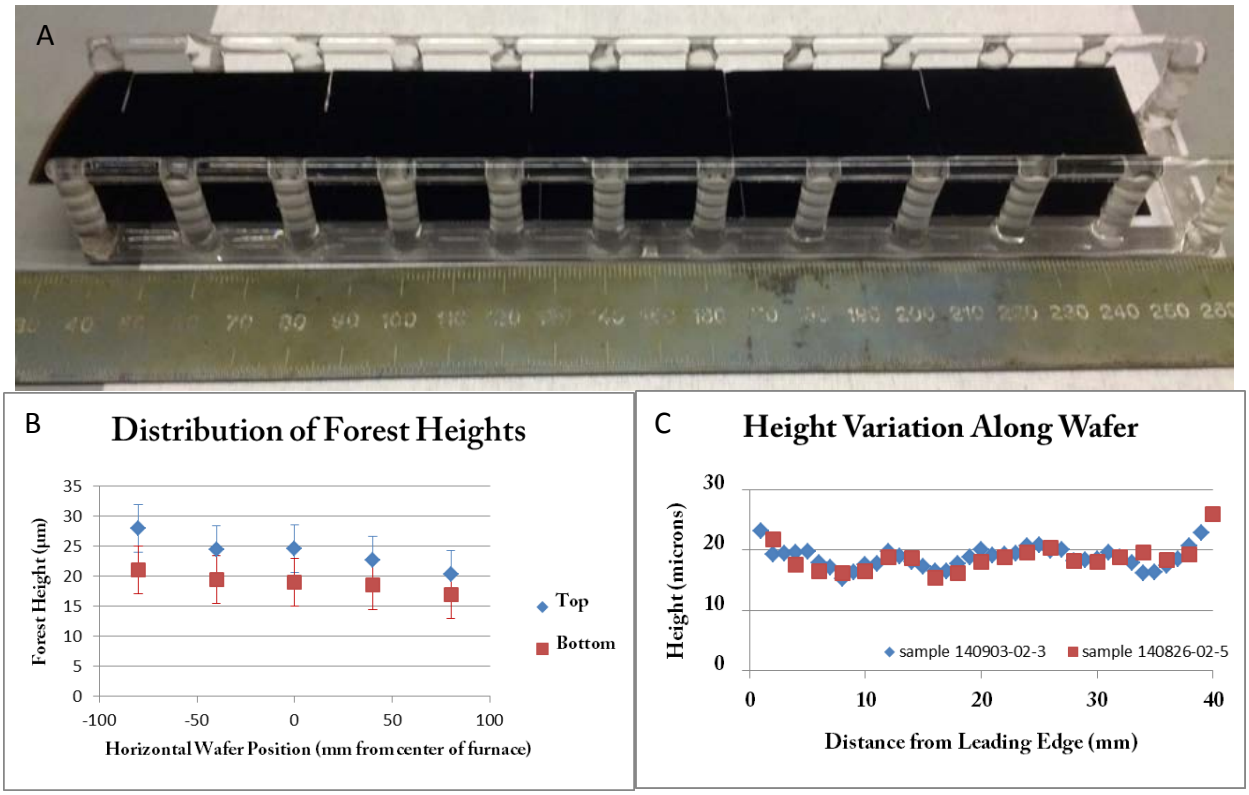

Figure 4-4: Top– Ten chip configuration to produce the maximum amount of forests per run. A scrap wafer piece was added to the inlet side of the boat to remove the leading-edge effect of 2-5µm increased forest height on the first chip. Bottom Left- Distribution of forest heights generated from this configuration from a set of 15 runs with the same growth time. Bottom Right – Height variation along two chips measured at 20 microns.

4.2.2 Water Addition

It is well known that water has a large impact on the growth of carbon nanotubes and is frequently used for 'super growth' [73] [74] [75] [76] . The lab folklore suggested that there was some ambient water being adsorbed into the system while the furnace was left open (anytime it was not doing a growth). The "first growth of the day" would have had the furnace left open overnight, allowing the maximum amount of water to be adsorbed (and, as the fourth comment supports, is nullified by doing a bake out). A paper in 2013 confirmed this suspicion, showing that after a furnace is left open, the humidity in the reactor is ~15% of the room's humidity (~1500ppmv from 40% relative humidity) during growth, and decreases by half in a subsequent growth or if a bake-out is performed [77].

Due to these observations, a DI water bubbler line was installed on the furnace. A small flow of helium (~30sccm), controlled by a rotameter, is put through a bubbler that saturates the helium at room temperature. This saturated helium flow then joins the rest of the gases at the furnace inlet. Because the lab space was climate controlled, the room temperature (and therefore water temperature) was a steady 22°C, and allowed for a simple table to be created (see Table 4-1) of water content inside the furnace vs. bubbler flow rate. At 22°C, a saturated gas will consist of 2.641% water. The water content during growth, listed in parts per million (ppmv), is calculated assuming the helium is saturated and the bubbler flow rate joins standard growth recipe flow rates of 1040sccm hydrogen and 400sccm ethylene.

Table 4-1: Water ppmv calculation from rotameter scale.

Rotameter Scale	He Flow (sccm)	H20 Flow (sccm)	ppmv water
1	16.6	0.4	300
2	33.1	0.9	594
5	82.8	2.2	1436
7	115.9	3.1	1968
10	165.6	4.4	2724
15	248.4	6.6	3886
20	331.2	8.7	4939

An experiment was performed using the standard growth recipe set at a 40s growth for eight different runs. Three of the runs were standard growths, one performed as the 'first growth of the day', another performed directly after a bake-out cycle, and one performed in the middle of the other runs. For the water experiments, the tube was baked out before every growth, and then a set amount of water was added using the water bubbler. The lowest level of water (600ppmv) was chosen because it was in the range of water detected from ambient in [77], and runs were performed at ~2000 and ~3000ppmv to determine the effect of increasing

the water. Three runs were performed at the 600ppmv water level to compare the standard deviation of the forest heights to that with no water added. Results, shown in Figure 4-5, clearly indicate that baking out the tube before growth and adding a controlled amount of water effects a stable, repeatable process. Three repeated runs at zero and 600ppmv added water show that water addition significantly (determined by F-test, F* = 2459, $F_{0.01,2,2}$ = 99) reduces the standard deviation from 28 to 0.58. Further, the addition of water produces a linear response in the height of the CNT forest over the range measured.

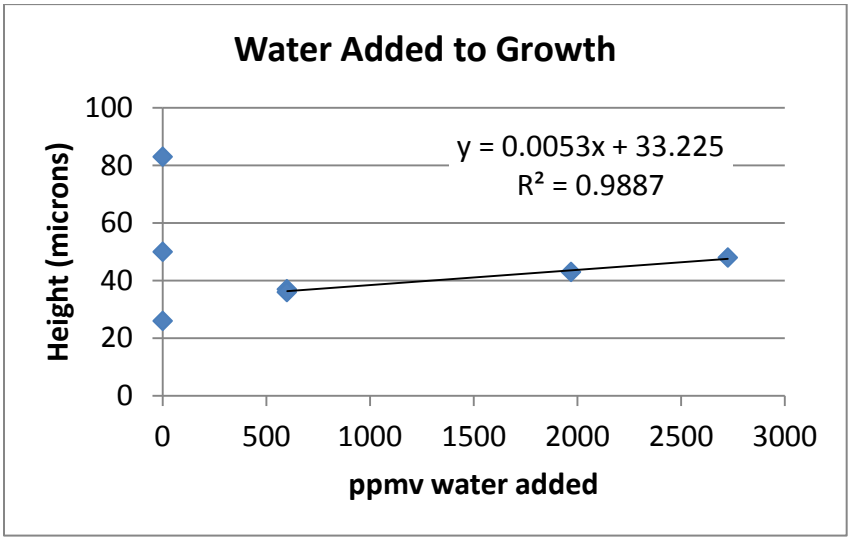

Figure 4-5: Stabilization of forest height using a bake-out and water. Note that there are three points at 600ppmv that overlap due to the very low standard deviation.

Because of the success of this method, water was added to the standard growth recipe. A water addition of 600ppmv was chosen to keep the water level within the same range as it was suspected to have been operated in previously due to ambient conditions, while being high enough that low levels of humidity (such as having the furnace open for fifteen minutes between runs) would not significantly affect the water level in the furnace. The resulting CNT forests were analyzed for similarity to previous growths (CNT diameter, number of walls, waviness, orientation), and found to be indistinguishable. (see section 4.5 for details).

It should be noted that 'super growth' papers that use water to increase rates and prolong carbon nanotube growth usually input water at a ~100ppmv level [75] [78]. It is unclear what humidity is native in the reactor and therefore unclear whether the 100ppmv is in addition to the ambient humidity effect.

A series of growths aimed at producing a consistent 10±2µm tall forest were conducted using just this modification to the original growth recipe (see section 4.1) and the four-chip angled boat configuration. Results showed that forest height control was significantly improved (Figure 4-6). The average height was 9.6µm with a 2.1µm standard deviation.

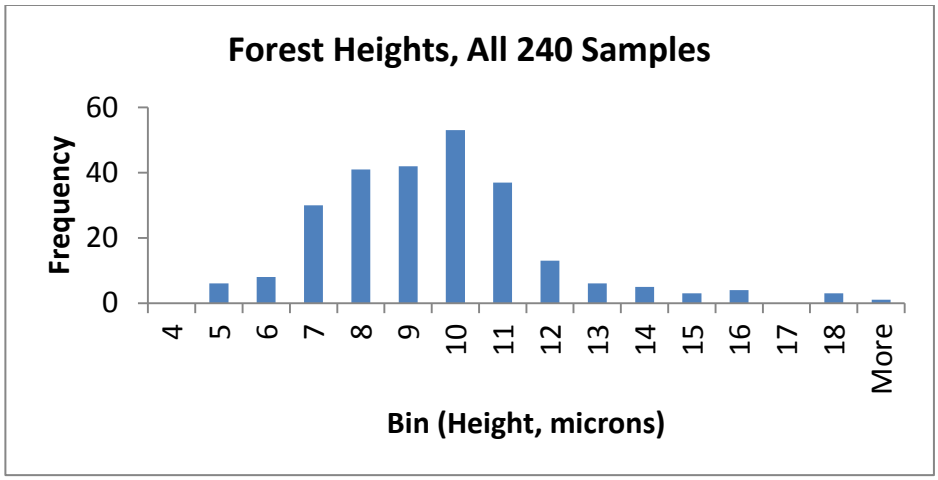

Figure 4-6: 60-growth study to determine the stability of the growth process with water added.

The very first growth performed in this study was an aberration that produced four forests at 16,18,18, and 20; this growth alone increased the standard deviation by 0.25µm. It was later discovered that the aberrations from 'first growth of the day' (like that growth) not only had a water component, they also had a temperature aspect that needed to be controlled (see section 4.2.3.2).

4.2.3 Furnace Temperature

It should be noted that everywhere in this thesis the furnace temperatures are reported approximately. This is due to the furnace being in a transient state for the entire growth cycle, and the thermocouples of the furnace not matching the internal temperature of the quartz tube. For instance, if the furnace (all zones) is set to 680°C (the standard growth temperature) and left on to stabilize for two hours, the temperature will stabilize to 738±2°C (as read by two independent thermocouples placed in the center of the furnace), as opposed to the furnace thermocouple readings of 682±2°C. This is a 56 degree offset. Furthermore, as will be elucidated by the following experiments, the furnace significantly overshoots that steady-state temperature and gradually returns to 738°C. This means that the growth will always occur hotter than 738°C. Unless otherwise specified, this thesis continues the practice of reporting the setpoint temperature rather than the in-tube temperature.

4.2.3.1 Furnace Calibration

Before starting experiments, the furnace temperature profile was checked using an independent thermocouple placed inside the furnace tube (no endcaps, open to ambient). The temperature was measured from both ends of the furnace in two separate runs. The first run inserted the thermocouple as far as possible (40cm) into the furnace from the inlet side. The furnace was allowed to heat up for 32 minutes, then the temperature profile was measured by retracting the thermocouple 5cm every 2 minutes, ending at the furnace inlet at a time of 64

minutes. This experiment was then repeated from the outlet side. During this test, it was noticed that the in-tube temperature was significantly higher than the furnace thermocouple reported, and decreased over time. Due to the furnace being in a transient state, there is a temperature difference between the inlet and outlet measurements because the temperature measurements were taken at different times (Figure 4-7).

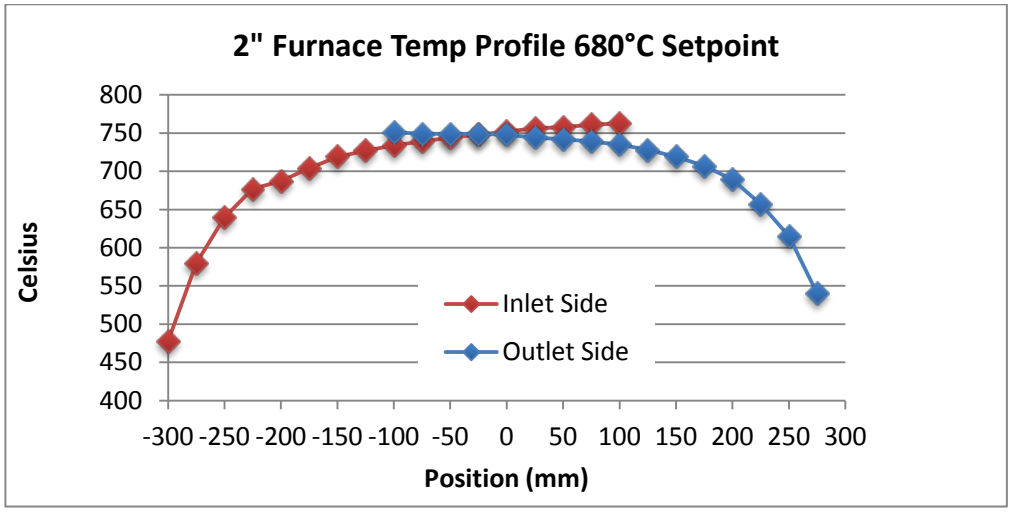

Figure 4-7: In -furnace temperature profile. Note that the temperature is still transient during these measurements, causing the measurements from the inlet and outlet side to differ due to the different times at which they were measured.

After this initial experiment, two separate thermocouples, both K type, were used to check the transient in-tube temperature at the center of the furnace. One thermocouple was shielded and did not register as great of a temperature overshoot as the other, however the temperatures recorded at steady state (after two hours) were within three degrees. Both thermocouple calibrations were checked using boiling DI water and icewater. The unshielded thermocouple was used in the following testing to more accurately determine the furnace temperature overshoot. The thermocouple was inserted into the furnace tube, the furnace was turned on with a setpoint of 680°C (all three zones) and left for two hours. Temperature readings were taken at least every minute for the first twenty minutes, then every five for the remainder of the two hour period. The furnace thermocouples showed a steady increase to 680°C in 6 minutes, then stabilized to 682±2°C. However, the in-tube thermocouple showed that the temperature drastically overshot the setpoint, reaching a maximum of 800°C in 8.5 minutes. It then decreased and began to asymptote to a lower value. After 90 minutes, the temperature stabilized to 738±2°C and remained there for the second hour (Figure 4-8). Not only does this suggest that the furnace thermocouples are offset by -56°C (either because of their placement or because of how the reader converts the data), it shows that the furnace undergoes a significant transient as it heats up, and the actual temperature during growth is

significantly hotter than previously suspected, especially for the short growths (<1 min) used in this thesis.

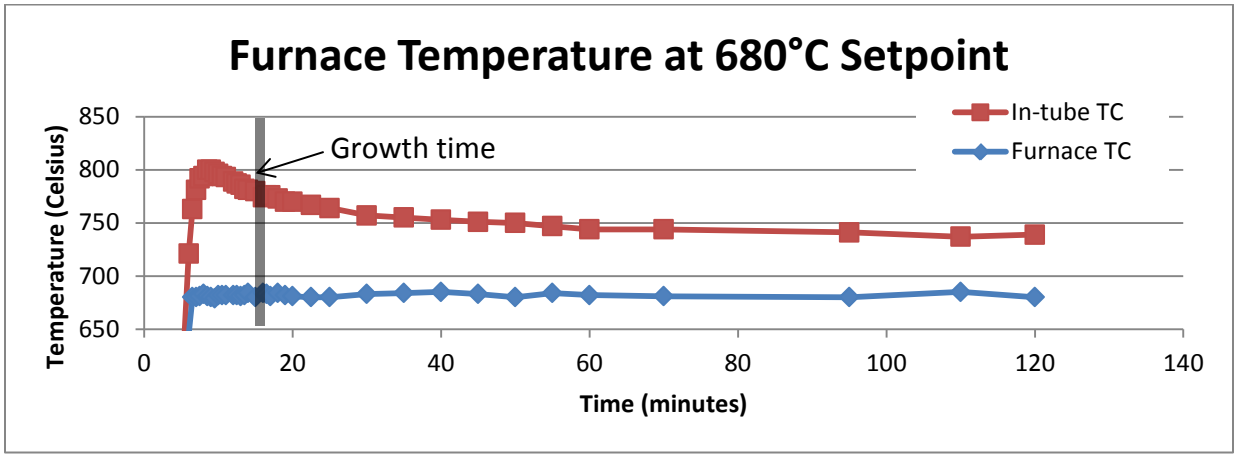

Figure 4-8: Furnace temperature over time at a 680°C setpoint, begun from 60°C. The growth occurs at 15 minutes into furnace heatup, and therefore is ~100°C hotter than recorded by the furnace.

4.2.3.2 Furnace Starting Temperature vs Growth Temperature

The growth process purges the gas lines for three minutes, sets the furnace zones to a 680°C setpoint, then waits for fifteen minutes before the ethylene is turned on to grow the CNTs. As a result, the furnace will be in a transient state, and the growth temperature different than the furnace thermocouples are recording. Multiple runs were conducted using the in-tube thermocouple to determine the actual growth temperature and the maximum temperature overshoot. In all experiments, the furnace zones were set to 680°C and the temperature was recorded using both the furnace thermocouple and the in-tube one. Because the recipe used for this study did not include the gas line purge, the 'growth' (the time at which growth would begin in a normal recipe) would begin at 15 minutes and last 30-60 seconds (see Figure 4-8). The 'growth temperature' is reported as the in-tube thermocouple temperature at 15 minutes.

After performing multiple runs, it was discovered that the amount of temperature overshoot on startup as well as the growth temperature (read from the in-tube thermocouple) was dependent on the starting temperature of the furnace (read from the furnace center thermocouple). The peak of the overshoot always occurred 8.5-9 minutes after starting the heat up, regardless of the initial temperature. The maximum amount of overshoot occurred if the furnace started from room temperature (~20°C), which corresponds to the first growth of the day. The temperature overshoot reached 830°C (set point 680°C) at 9 minutes and then decreased to 801°C at 15 minutes (the growth time). As the starting furnace temperature is increased, the overshoot and growth temperature decrease until reaching a minimum with a starting furnace temperature of 160°C. If the furnace is started from 160°C, the in-tube temperature overshoots to 785°C and the temperature decreases to 768°C at the growth time.

At starting temperatures greater than 160°C, the overshoot and growth temperature begin to increase, however are within a few degrees in the starting temperature range of 150°C-180°C. See Figure 4-9 for visualization of these trends. Starting temperatures higher than 190°C were not explored because it is unlikely to start the furnace at a temperature higher than that (due to previous growths ending at 200°C).

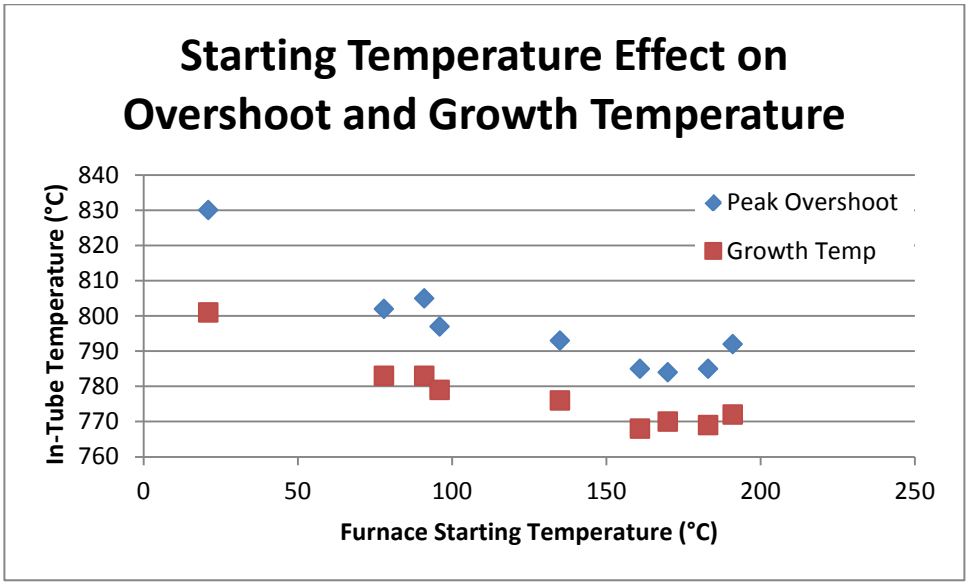

Figure 4-9: Graph showing that the starting temperature of the furnace affects the temperature overshoot as well as the growth temperature. In-tube temperatures are a maximum when the furnace starts heating from room temperature, and reaches a minimum when the furnace starts heating from 160°C.

Note that the 'first growth of the day' phenomenon can be explained by the large discrepancy in growth temperatures. Assuming an Arrhenius model, reaction rates increase with increasing temperatures; the first growth of the day is at least +20°C and a maximum of +33°C hotter than any other growth, which would cause an increased growth rate, which would lead to an increased forest height for the same growth time. All other common furnace starting temperatures (100-180°C) are within ±5°C – the discrepancy between the first growth of the day is five times larger than the variation between other growths. Therefore the 'first growth of the day' phenomenon is at least partially, and likely substantively, caused by the growth temperature difference.

One run was performed with helium flowing at 1000sccm to determine if the gas flow would affect the furnace temperature overshoot or growth temperature. The run, beginning at 167°C, exhibited the same growth temperature as the 170°C run with no gas (770°C), and a similar maximum overshoot temperature (790°C vs 785°C). We therefore conclude (preliminarily) that gas flow does not affect the in-tube measured temperatures.

The idea of inserting a furnace temperature hold at 200°C for five minutes to stabilize the starting temperature was attempted and discarded. Due to the addition of the water to the growth, no CNTs were grown if this temperature hold was used while water was on. In addition, no CNTs were grown if the water was turned on after this temperature hold, up until the furnace temperature reached 600°C or more. Due to the manual process of turning on and setting the flow rate of the water at the time of this study, it was decided that there would be less variation if the water was turned on at the beginning of the process and the growth started at a particular temperature, rather than waiting until a high temperature to turn on the water mid-process.

When accounting for starting temperature, the standard deviation of the set of growths plotted in Figure 4-6 (section 4.2.2) decreases to 1.3µm (see section 4.2.4 for detailed regression analysis). This means that with just controlling the water and starting temperature, 87.4% of the forests grown will meet the goal of ±2µm.

4.2.3.3 ANSYS Fluent Modeling of Chip Positions and Gas Flow

In an effort to understand the chip positioning effect, and to try to find an optimum chip configuration, ANSYS Fluent 14.5 was used to model the gas flow in the furnace around the 10-chip configuration.

The quartz tube dimensions and placement in the furnace were measured, and the dimensions of the inlet and outlet replicated in the model. The boundary condition at the tube wall was assumed to be no-slip, with a set-temperature boundary condition. The temperature profile of the tube wall was input in a user-defined function following the temperature profile recorded during the furnace calibration experiments (see Figure 4-7 in section 4.2.3.1). The gas flow was input as pure hydrogen at 1440sccm (the total gas flow of hydrogen + ethylene during growth) with a uniform velocity profile and 300K inlet temperature. The exit was modeled as a pressure outlet at one atmosphere (future work could modify this pressure value to analyze its effect). The chip dimensions and placement were measured and input into the furnace model, however the quartz boat was omitted to simplify mesh generation. Boundary conditions on the chips were modeled as adiabatic, no slip. A full tube was modeled at a sparse mesh density (4,260,648 elements) to ensure that the recirculation regions were symmetric about the midplane, then a half-tube model was run with a symmetry condition at the midplane. This was done to be able to increase the mesh density around the inlet and chips while keeping the solver time under a day. In the half-tube model, the generated mesh consisted of 8,074,568 elements. Both meshes were automatically generated using automatic inflation layers around the chips and inlet.

The first model (both full tube and half-symmetric) runs were done using realizable K-ε with standard wall function and buoyancy enabled. The results (Figure 4-10) show large

recirculation regions at both the entrance and exit of the furnace. The entrance recirculation region extends 41 cm into the furnace, to within 12 cm of the chips, showing the importance of the placement of the chips in the furnace. The exit recirculation region is marginally smaller, but also extends backward into the furnace 40 cm. This shows that the accumulation of carbon deposits at the exit may be able to reenter the furnace and influence the A-CNT growth.

It should be noted that the recirculation regions are dependent on entrance and exit conditions. In the first iteration of the model, the exit was modeled as a hole rather than the first 10cm of pipe, which resulted in a much smaller recirculation region at the exit (~20cm). The inlet was also switched to the bottom of the tube (gravity reversed), which resulted in the entrance recirculation region growing to within 10cm of the chips. This indicates that the inlet position and orientation may have a significant effect on the growth of CNTs.

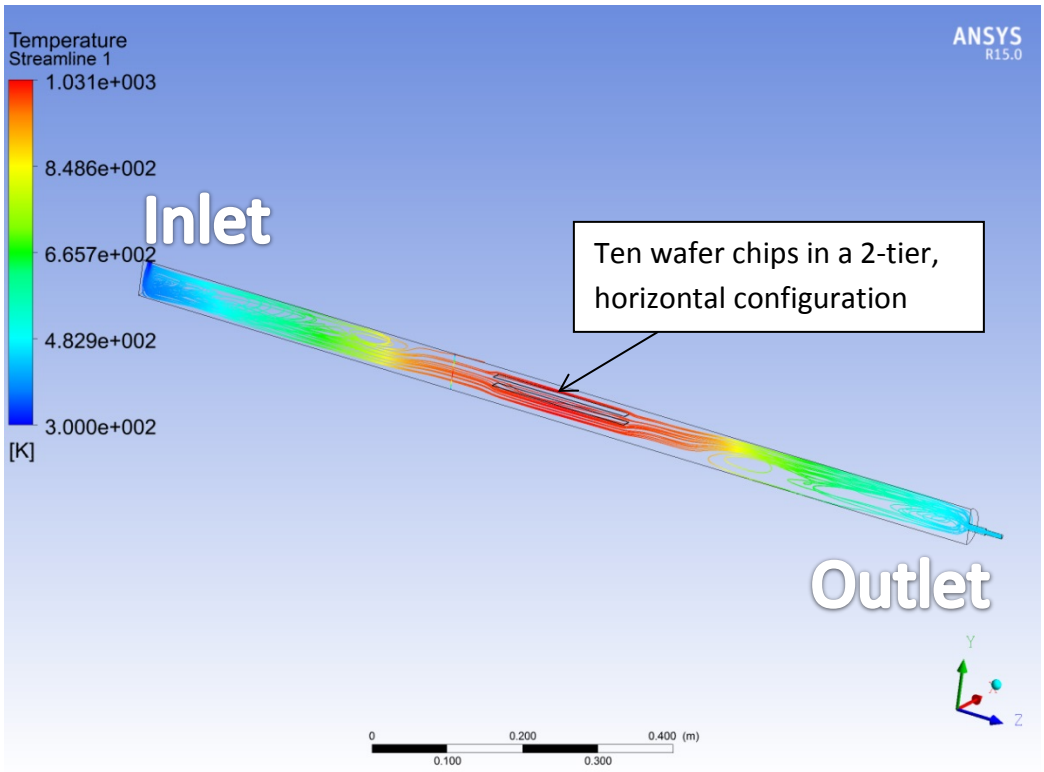

Figure 4-10: ANSYS Fluent model of gas flow during A-CNT growth. Streamlines (colored by temperature) show recirculation regions at inlet and outlet. Gravity is in the –y direction, and wafer outlines can be seen in the center of the furnace.

The half-tube model was run again using realizable K-ε with enhanced wall function, Reynolds with both standard and enhanced wall function, and shear stress transport (SST) to ensure accuracy. Differences between the models were negligible with regards to recirculation region, velocities and temperature profiles. Turbulent kinetic energy around the chips was

negligible and ranged from ~3e-10 J/kg from the SST model to ~6e-12 J/kg for the Reynolds with enhanced wall function. (Laminar kinetic energy was in the range of 0.004 J/Kg.)

The chip region was analyzed for velocity profile over the chips and temperature distribution. The temperature varies across the chips; the center chip is 1031K (756°C), while the outer chips are at 1001K (726°C). This temperature difference may explain the difference in heights between the growths from the center of the furnace and the growths from 100mm off center. The velocity along all chips is shown to be relatively constant (Figure 4-11, right), although due to the constriction between the upper and lower chips, the velocity in that region is 3.75cm/s vs the 6.25cm/s at the top of the boat. This may explain the 5µm difference in heights between the top and bottom of the boat (bottom is shorter), as the carrier gas would be providing less fresh reactants to the chips at the bottom of the boat.

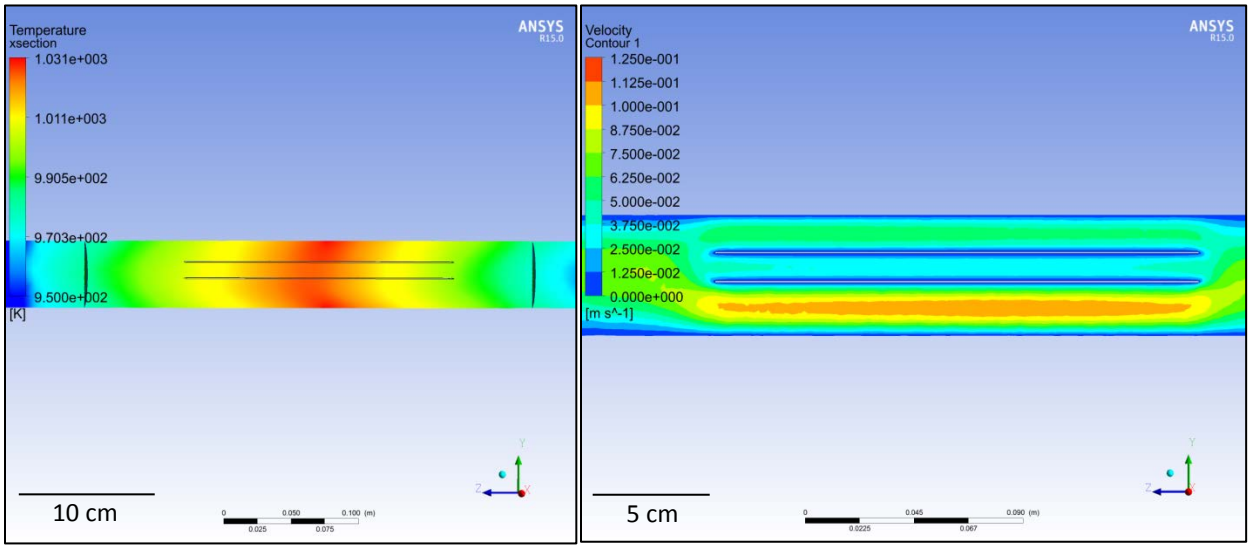

Figure 4-11: ANSYS model results around the chips. Inlet is from the right. Left - temperature distribution around the chips. Right- velocity distribution around the chips. The ten 625µm-thick chips are oriented horizontally in the furnace, in two rows, 3cm wide in the x-direction and 4 cm (x5) in the z-direction.

The chip size and orientation in the furnace was changed to determine the effects on the velocity profile. A symmetric half-tube model was again performed with ten 3.5cm square chips oriented vertically and spaced 2cm apart. Results show that the upstream velocity profile and recirculation region is unchanged. A similar temperature distribution across the chips is also noted, although each chip is now at a uniform but different temperature (Figure 4-12). The velocity of the gas adjacent to the chip face is an order of magnitude lower than in the horizontal chip case, but is uniform across all chips. Due to this uniformity, a vertical wafer placement is suggested for future work. While the lower velocity might result in shorter forest heights, the uniformity across all wafers will allow for easier optimization and the slower growth rate will be beneficial for obtaining more exact forest heights.

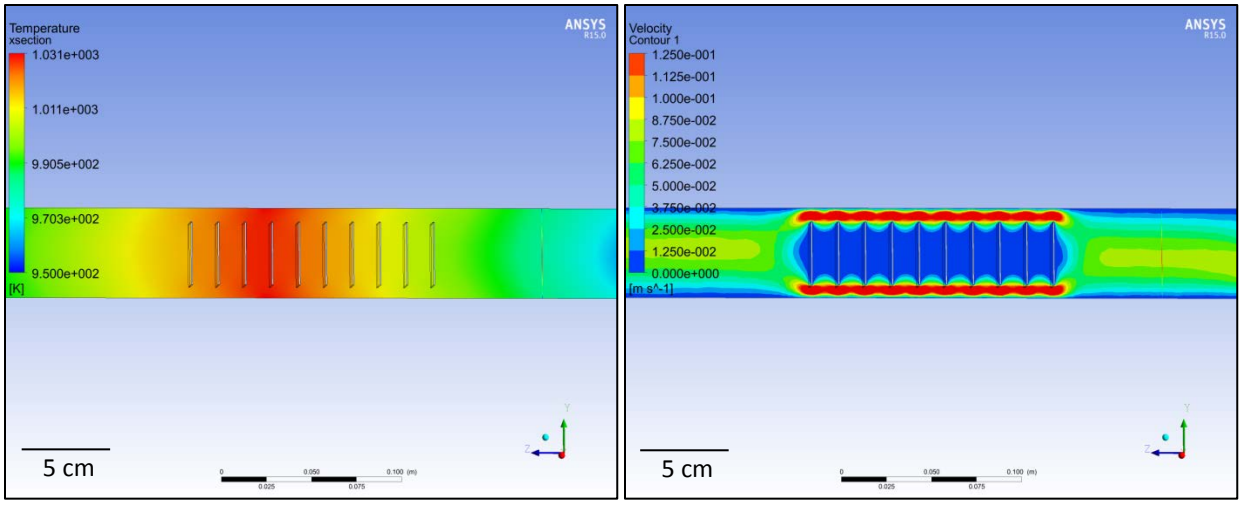

Figure 4-12: Left - temperature distribution in the furnace with vertical chips. Right - velocity profile with vertical chips. Chips are 625µm thick and 3.5cm x 3.5cm square.

The preliminary modeling with the two chip configurations show that the upstream and downstream temperature and velocity profile (±14cm from center of furnace) doesn't change with chip orientation, allowing future modeling to reduce the model to just the tube section that contains the chips (thereby increasing the achievable mesh resolution). Future modeling can explore chemical reactions on the chips, allowing the exploration of growth conditions by altering gas flow rates and ratios, chip orientation and size, as well as adjusting the furnace temperature. This modeling could yield more samples per growth and improve forest uniformity.

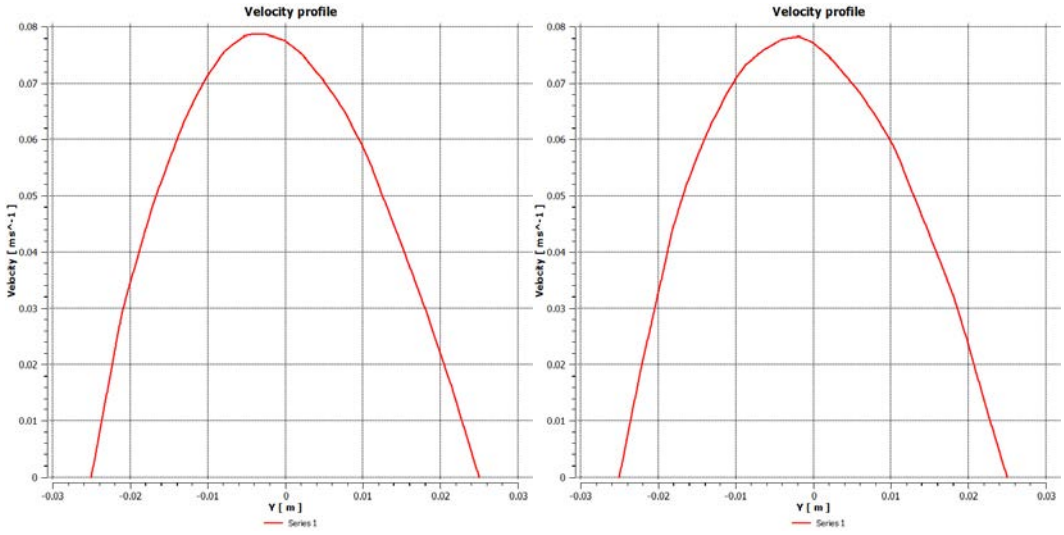

Figure 4-13: Velocity profile from a cross section taken 4cm upstream of the chips in the horizontal (left) and vertical (right) chip configurations, showing that the upstream velocity is independent of chip orientation, and therefore the tube section containing the wafers can be modeled independently, allowing greater resolution.

4.2.4 Carbon Nanotube Height Prediction

A set of previous growths were data mined to create a prediction of height given water vapor level, furnace starting temperature, growth time, and furnace position. 65 initial growths while experimenting with water and boat position were analyzed using JMP software. A regression analysis was performed with growth time (15-45 seconds), bubbler setpoint (2-5), furnace starting temperature (20-170°C), linear and quadratic horizontal position (-100 to 100mm) and vertical positions (top and bottom of boat) considered as parameters. In addition the tube age was tested as well. It should be noted that for these initial growths, the starting temperature never exceeded 160°C, and therefore the parameter estimates only showed a linear dependence on starting temperature. The parameter significance for each was calculated and is shown in Table 4-2; a value of less than 0.02 is significant.

Table 4-2: Parameter significance calculated from JMP (<0.02 is significant and colored orange, red if borderline).

Parameter Estimates

Term	Prob>|t|
Intercept	<.0001*
seconds	<.0001*
bubbler setpoint	<.0001*
starting temp	<.0001*
horizontal (mm from center)	0.0195*
vertical (boat level, 1 = bottom)	<.0001*
horizontal (mm from center)*horizontal (mm from center)	0.0998
Run #	0.2148

The equation generated from that model was as follows, where t = growth time, w= water bubbler setpoint, T = starting temperature in Celsius, x is the horizontal position from the center of the furnace and Z is the vertical position:

Equation 1:

$$height = -14.5644 + 1.1786t + 1.0454w - 0.0349T - 0.009413x + 0.8022Z$$

The set of runs done with the four-wafer configuration (Figure 4-3) were then analyzed to determine the height dependence on starting temperature and growth time (water and position were kept constant throughout the growths and therefore could not be added into the model). The resulting equation shows a linear dependence on time, and a quadratic dependence on starting temperature:

Equation 2:

$$height = -2.9994 + 0.8250t - 0.0217T + 0.000248 * (T - 128.698)^2$$

The ten sample configuration was then analyzed for a set of 50 runs done over a two week time span to obtain the model for this system setup. Again, the water was set at a bubbler setpoint of 3 (see Table 4-1 for ppmv estimate) for all growths so there is no water dependence reported in this study. Also, the furnace temperature was always started below

170°C, which means that the starting temperature was again reported as linear rather than quadratic. Other parameters that were checked were the run number, run number after bake-out, and the wafer batch. The only one of those that had a correlation was the run number; because this was disproven for the other models, it is suspected that the cause was misalignment of the seals that were reseated partway through this run set, and this parameter should be far less significant than shown. For the ten wafer configuration, the quadratic dependence on horizontal position (x-placement) is also negligible, again owing to the short forest heights and the restricted growth region about the center of the furnace. See Table 4-3 for parameter estimates.

Table 4-3: Ten-wafer configuration parameter estimate and significance (<0.02 is significant).

Term	Estimate	Std Error	t Ratio	Prob>|t|
Intercept	-4.804058	3.402444	-1.41	0.1586
z height	5.0182261	0.28733	17.46	<.0001*
x placement	-0.035256	0.00254	-13.88	<.0001*
growth time	0.3773059	0.063513	5.94	<.0001*
start temp	-0.048408	0.007888	-6.14	<.0001*
#after bakeout	-0.185776	0.137469	-1.35	0.1771
run	0.087671	0.012103	7.24	<.0001*
wafer batch	-0.755591	0.48864	-1.55	0.1226
(x placement+0.44444)*(x placement+0.44444)	-4.178e-5	5.356e-5	-0.78	0.4357

The ten-sample height prediction is then as follows, where z is the boat position (1 for bottom, 2 for top), x is the position from the center of the furnace (negative is upstream), t is growth time, T is the furnace starting temperature in Celsius, and R is the run number:

Equation 3:

$$height = -4.804 + 5.018Z - 0.035x + 0.377t - 0.0484T + 0.0876R$$

4.3 New Growth Method

Based on the analysis presented in this chapter, a new growth method and recipe was established. Large differences between the old growth method in section 4.1 include the use of a bake-out step before the first growth of the day and every third growth thereafter, the start of the growth when the furnace temperature is 165±10°C, the use of water throughout the growth, a quartz boat to hold ten chips, and a shortened delamination time. See Appendix B for the new growth script.

1. **Bake out**: Because the furnace tube adsorbs water from ambient humidity and accumulates hydrocarbons/amorphous carbon during growths, it must be cleaned periodically. The bake out must be done if the furnace has cooled to room temperature or if three growth cycles have been completed since the last bake out. The furnace is initially at room temperature, then the quartz tube is heated to 750°C while open to the air to

remove any of the contaminants from previous growth cycles. The furnace is ramped to a 740°C setpoint in approximately 10 minutes, and then held at 740°C for 3 minutes before the furnace is shut off and allowed to cool down.

2. **Load and Purge**: Ten 3cm x 4cm chip pieces are inserted into the center of the quartz tube on a quartz chip carrier (Figure 4-4), the tube is sealed and the furnace lid is closed. When the furnace temperature drops from the bake-out temperature to 165±10°C, the growth cycle is initiated. This temperature was chosen because the time required to remove the previous growth's chips and insert the new ones causes the furnace temperature to drop below 180°C, and allowing the furnace to drop to 165°C yields the least variability in the growth temperature for small changes to the starting temperature. All lines are purged at 400sccm for one minute, then the tube is purged with helium at 2000sccm for five minutes to ensure an inert environment.
3. **Growth Cycle**:
    a. *Catalyst anneal*: During this time approximately 600ppmv water is introduced into the furnace by bubbling helium through a water bath. With the setup used in this thesis, the helium flow rate through the bath is controlled by a hand rotameter (all other flow rates and furnace temperature are controlled through the use of a computer program), so the precise amount of water in the furnace can only be estimated to within 100ppmv. The furnace is set to 680°C and ramps to that temperature over a period of seven minutes. Eight more minutes pass for a total of fifteen minutes in the anneal step.
    a. *Growth*: Once the anneal is complete, ethylene is turned on at 400sccm for a time period specified by the desired height of the forest. For example, a 20μm tall forest would result from a 30 second growth. During this step the hydrogen continues flowing at 1040sccm, resulting in a H_2:C_2H_4 ratio of 2.6.
    b. *Delamination*: While hydrogen and water continue to flow, ethylene is turned off and helium is turned on at 500sccm for 30 seconds. Because of the water still flowing in the reactor, this is a more effective etch than hydrogen alone and takes much less time (30 seconds vs. 5 minutes) to make the CNT forest easily delaminate.
4. **Cool-down**: The furnace is shut off once the delamination step is complete. Hydrogen is also shut off and the furnace is allowed to cool under helium and water. Once the furnace temperature drops to 550-600°C, the water is shut off and the furnace lid is opened to increase the cooldown rate. The longer the water is left on, the easier the forest delaminates: however if one forgets to turn the water off while the furnace cools, the forest will completely delaminate from the chip and result in a "magic carpet" that will float off the chip while it is being removed from the furnace. Once the furnace temperature reaches 225°C (10 minutes), the helium is shut off and the process is considered finished.

5. **Chip Removal**: The tube is opened and the chips removed as soon as the process is finished, while the furnace is still at 225-200°C. This is done to avoid the necessity of baking out the tube again after each growth; the boat can be reloaded and the next growth can then be started as soon as the furnace cools to 160°C.

The total cycle time for a growth is 32 minutes plus growth time (~30seconds per 20µm height), not including the bake out and chip-loading time. The bake-out step takes 25 minutes and loading/unloading chips while the furnace drops to 160°C takes approximately ten minutes. Averaging one bake-out per three growths, the total growth process takes 50 minutes.

It should be noted that each of the uncertainties in the growth process (using a hand-rotameter to input water, beginning the cycle at 150-170°C, opening the furnace at 550-600°C) and other variables such as chip positioning cause variability in the final height of the forest. In addition, the growth times (~30s) are short compared to the residence time (~84s) of gases in the tube furnace at our current flow rates (calculated assuming laminar flow of 1440sccm in a 50mm diameter, 1m long tube), meaning that at no time during the growth is the gas concentration steady-state. Recall also that the temperature of the furnace is not at steady state at any time during this process (see Figure 4-8 and associated discussion), and these factors contribute to the variability in the forest height.

4.4 Proposed Hot-Load System

The current growth method is very slow (50mins) compared to the actual growth time (~30 seconds). Producing enough forests for desired laminate test matrices is time consuming, even for the small sample size of the short beam shear testing. To consider doing other tests (such as mode 1, bolt-bearing and compression after impact), a faster method needs to be developed. In response to this, a new growth method is proposed to enable keeping the furnace hot at all times. This will eliminate the need for a bake-out step, as well as the heat-up and cool-down portions of the growth process – thereby reducing growth time from 50 minutes to 5 minutes (2 minute purge on either side of the ~1min growth + delamination time).

The 'hot-load' system will consist of a simple replacement of the downstream endcap on the furnace (Figure 4-14). The new endcap will have a pass-thru for a 1/8" diameter thermocouple rod that will also act as a push/pull rod for the quartz boat. The exhaust will exit out of a port that is connected to the pass-thru, acting as a counter-flow barrier if the o-ring seal in the pass-thru has a small leak. The o-ring seal should be made of high-temperature material, eg Kalrez 4079 [79], so that the push rod will not damage it when it is pulled out of the hot furnace (the current o-rings on the furnace tube itself are viton). The quartz boat can easily be loaded into the downstream end, connected to the push rod and the system sealed with the new end cap. When the furnace is left on at a 680°C setpoint, this end of the tube will be at ~200°C. Once the system is purged, the quartz boat can be pushed into the already-hot furnace,

and the growth cycle can commence immediately. Once the growth cycle finishes, the quartz boat can be pulled back out to the cool tube end. The tube will be purged with helium again, and then the system can be opened and the cycle repeated.

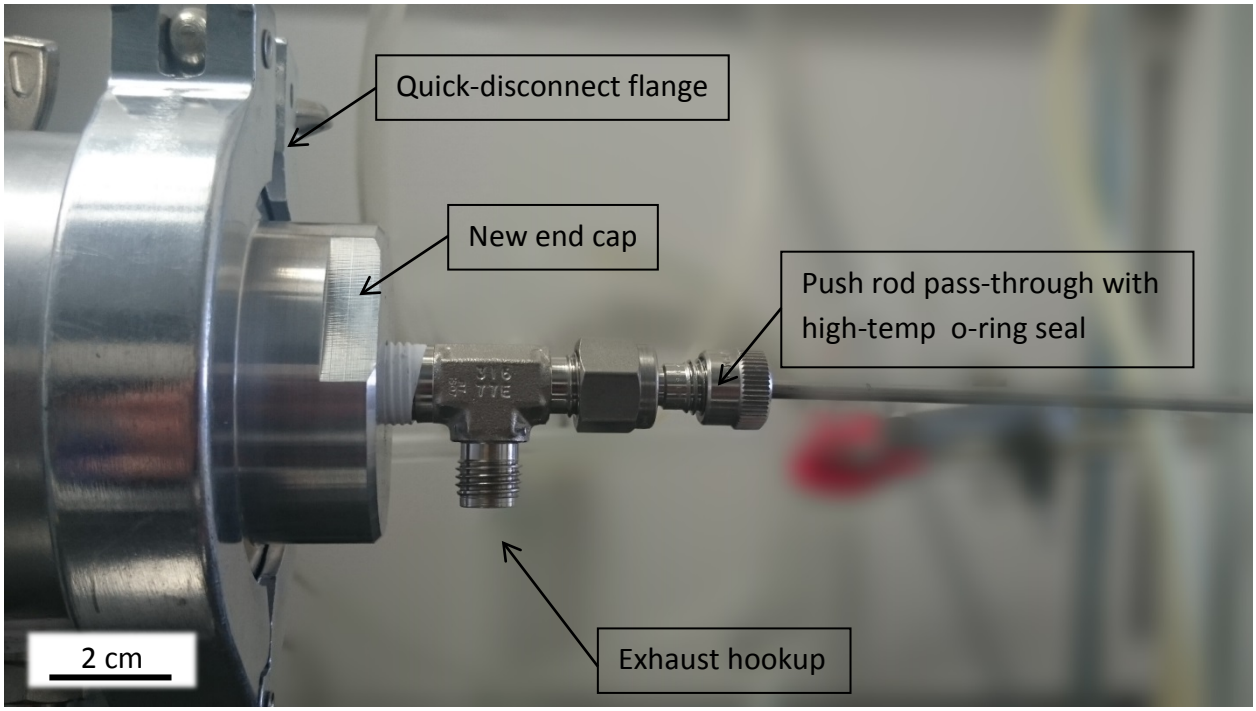

Figure 4-14: Hot-load end cap and pass-through (exhaust side).

The safety systems need to be upgraded in order for this system to work. A LabVIEW program or Ansari script must be written so that the hydrogen cannot be turned on without a helium purge first. An oxygen or water sensor should be installed and the program set up such that hydrogen cannot be turned on if there is more than 2.5% oxygen (the upper explosive limit of hydrogen is 95% in oxygen. 2.5% oxygen would be a safety factor of 2). The program should also be set up to discontinue hydrogen flow if the water level suddenly increases during a growth (indicating an oxygen leak).

The growth recipe may need to change to accommodate this new growth method. It is suspected that the anneal time can be drastically decreased or even eliminated with the hot-load technique. This is due in part to the instant exposure to high temperatures, which will reduce the iron catalyst layer immediately. Work from Carl Thompson's group at MIT [80] suggests that hydrogen only needs to be turned on concurrently with growth, with no separate anneal step. The difference in the resulting catalyst layer may require slightly different growth parameters, such as a modified temperature or gas flow rates, to be effective. It is unclear from literature whether the hydrogen:ethylene ratio will need to be changed, or if the water content will need to be altered when switching to this hot-load method. Bake-outs will not be necessary

as the furnace will be opened to air at high temperature every cycle, burning off the carbon deposits (and water will not adsorb at those temperatures).

So far, a new mass flow controller (MFC) box that included a MFC for the water bubbler and ports for a water sensor and pressure sensor was installed. The water sensor was purchased and is a Kahn Cermet II hygrometer and the pressure sensor port can be used with a standard pressure sensor from McMaster-Carr. Neither have been installed on the furnace yet, but have been purchased and exist in the lab. A vacuum pump and needle valve were also purchased for possible use in adjusting the growth pressure, but have not been installed either. The new end cap was installed and tested in the standard growth cycle, to ensure that there was no change due to the addition of the pullout rod and its seal. Unfortunately, the growth showed signs of a very minor oxygen leak (nonuniform growth near edges – this is indicative of not enough water, or too much oxygen: a slightly increased oxygen leak results in less dense forest growth overall), suggesting that a second seal should be added before this method is used in actual growths. In addition, MIT EHS was consulted to determine the safety of the system. They strongly recommended that the entire process be able to be kept in the hood, so the furnace will need to be moved such that the pullout rod can fit entirely inside the hood when extracted.

4.5 Carbon Nanotube Characterization

Aligned carbon nanotube (A-CNT) forests used in this work were grown in house using a catalytic CVD method. Because the growth method was changed from prior work, forests from both the original growth method (section 4.1) and new growth method (section 4.3) were analyzed. The forests were analyzed in a variety of ways to determine their structure. SEM was used to give an approximate spacing used to estimate the density, and the images analyzed in ImageJ to determine the overall orientation and individual nanotube waviness. TEM was used to determine the diameter of the individual nanotubes and obtain the average number of walls. A crude attempt using a mass balance sought the density of the A-CNT forest and amount of water adsorption. And finally, of paramount importance to this work, a way of measuring the forest height using an optical microscope was invented, providing a nondestructive method of measuring every forest.

4.5.1 SEM and TEM Image Analysis

TEM images were taken from samples from a dry (zero added water) and a 600ppmv water growth using the 'new growth recipe' to compare to the samples grown with the 'original growth recipe'. It was suspected that water addition at the 600ppmv level will reproduce the conditions in the 'original growth recipe' due to the ambient conditions providing water (see 4.2.2 for discussion). Nanotube outer diameter and number of walls was measured from the images. As shown in Figure 4-15, the number of walls is consistent between the two growths (2-

6 walls), however the diameter of the nanotubes in the dry recipe had a bimodal distribution with a mode of 5.5nm. The wet growth had an 8nm average diameter. The reported outer diameter and number of walls from the old growth recipe was 8nm and 3-7 walls [81]. From this data it was confirmed that the wet growth was most similar to prior growths (confirming prior growths were affected by water), and that the new growth recipe maintains the structure of the forests.

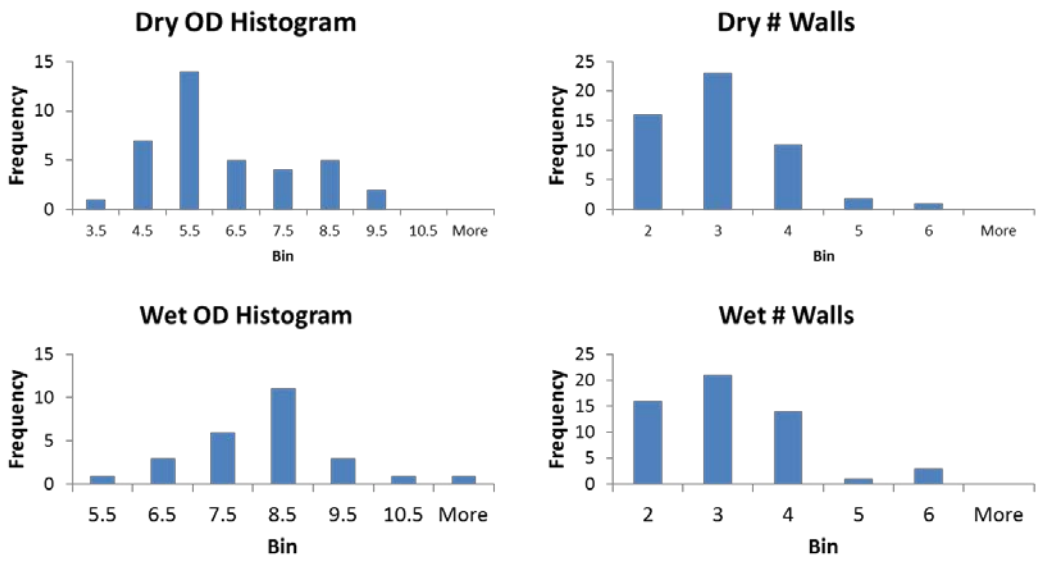

Figure 4-15: Histograms of diameter and number of walls from a dry growth (top) and wet growth (bottom).

In addition, another forest from the new growth recipe (including water) was TEM imaged to get a better statistical measurement of the diameter. The diameter was measured for 62 distinct nanotubes in those images, and averaged 7.04nm, with a standard deviation of 1.5nm. Note that the histogram (Figure 4-16) shows that the mode is again at 8nm. The number of walls was more difficult to discern in these images, and the total number of tubes analyzed was 11. The median number of walls was 4, however the modes were at 3 and 5 walls.

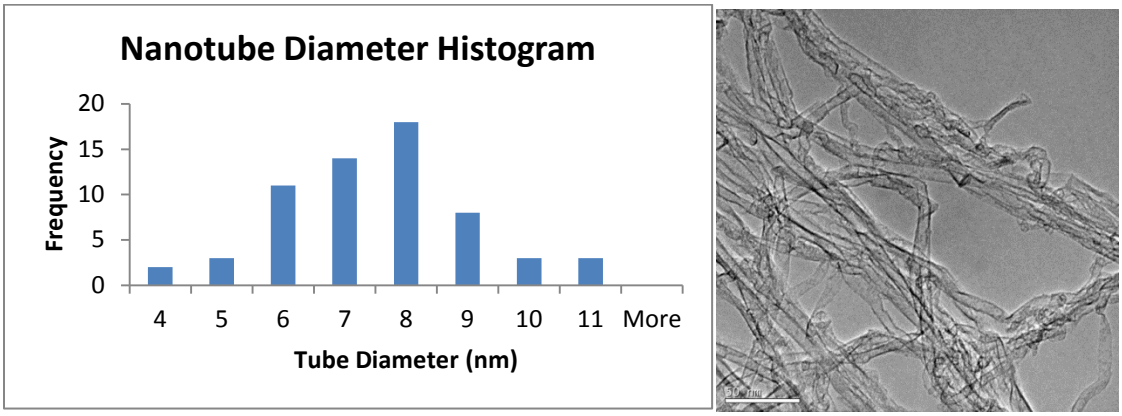

Figure 4-16: Left- histogram of nanotube diameter from a forest made with the 'new growth recipe'. Right – a representative TEM image of the nanotubes.

SEM images were obtained using a JEOL 6700 at the Institute of Soldier Nanotechnologies (MIT). Representative forests from the 'original growth method' and from the 'new growth method' were cleaved through the center and the cross-sections SEM imaged. Forests were imaged at a low magnification first to obtain a height measurement, then images were obtained at 25,000x and 50,000x to use for orientation, waviness and density measurements. The images were processed and analyzed in ImageJ.

Nanotube spacing was calculated from fifteen images at 50,000x in two ways. First, a hand count was performed, simply counting the number of nanotubes that were at the same apparent depth (i.e. brightness). Second, the same count was done by contrast enhancing the images, normalizing the brightness, then generating a line plot across the image (Figure 4-17). The distinct peaks above a brightness of 150 were counted. This number was chosen to make the peaks correlate with the visible nanotubes in the first image analyzed. The process was then automated with a macro in ImageJ to analyze the remaining images. The width of the image was divided by these counts to obtain the nanotube spacing. From the hand count, the center-to-center spacing was determined to be 65.7±10nm. The automated line count produced a spacing estimate of 67.3±9nm, within standard deviation of the hand count. Subtracting the average nanotube diameter of 8nm, the average inter-tube spacing is then ≈58nm.

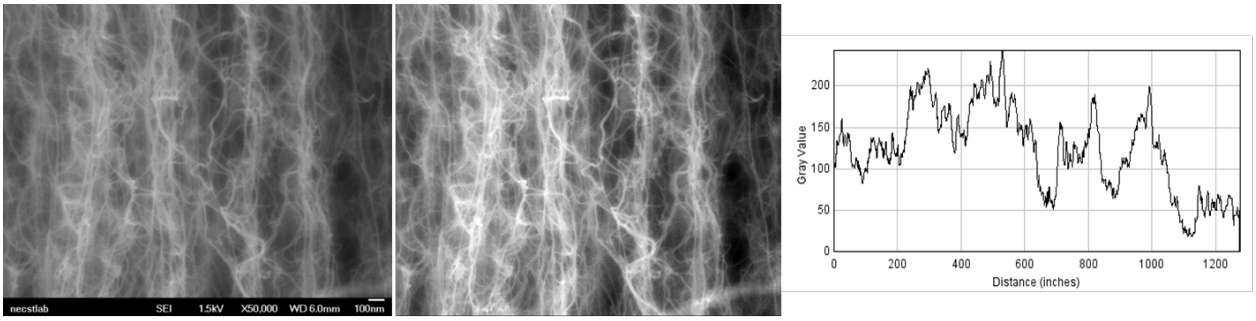

Original SEM Contrast Adjusted Line Plot of Brightness

Figure 4-17:ImageJ analysis of nanotube spacing. Original SEM image was contrast enhanced, then a line plot was generated across the center of the image. Bright peaks were counted to obtain average nanotube spacing.

To estimate volume fraction, this inter-tube spacing measurement was input into a model reported recently [82]. The volume fraction was calculated to be 0.0134 (1.34%). From this value and the density of an 8nm, 3-wall tube (1.46g/cc) [29] [30], the forest density is estimated to be 0.0195g/cc.

A crude attempt at calculating the density through using a mass balance was also performed. This method simply put an A-CNT-laden silicon wafer chip onto a mass balance, weighed it, then scraped the A-CNT forest off (easily accomplished due to the delamination step in the growth recipe) and re-weighed the chip. The difference was the weight of the forest. Height was measured using the microscope technique in section 4.5.2. Three sacrificial forests

were measured in this technique, and resulted in an estimated density of 0.0444 g/cc. If one again assumes a skeletal density of 1.46g/cc, this predicts a volume fraction of 0.03 (3%). It is suspected that water adsorption resulted in an increased weight measurement, and a recent study reported that ~50% of the mass of the CNT forests in ambient conditions was due to adsorbed moisture [83]. In that report, it was shown that the ratio of the wet and dry CNT array mass at a volume fraction of ~1 vol. % CNTs is ≈2.14±0.18 [83], which would yield an estimated CNT volume fraction of ≈1.42±0.12%, in excellent agreement with the volume fraction estimated from inter-tube spacing. To estimate the dry mass of the A-CNT forests studied here, an attempt was made to desorb the water using a BET surface area analyzer, similar to the previous study [83], however the instrument was unable to accurately measure the small weight of the A-CNT forest. Another attempt was made by baking a sample at 200°C for two hours before weighing. Due to the readsorption of water, the mass began to immediately increase, similar to what was previously observed for ~1 vol.% A-CNTs [83], and did not stabilize for 50 minutes. The final weight (1.88302g) was subtracted from the zero-time weight (1.88215g). The forest was then scraped off the wafer as before, and the wafer re-weighed. The re-weighed mass was greater than the dry measurement, suggesting that a more accurate scale or larger volume of A-CNTs (i.e. larger mass) would need to be used in the future to accurately estimate the mass of the A-CNTs in this way.

NeuronJ, an add-on to Image J, was used to measure the waviness of the nanotubes. This addon traces lines of relative brightness from a selected starting point to a selected endpoint. Once the desired lines have been traced in the image (Figure 4-18), the program measured the length of all lines in pixels. The height of the image in pixels was used as the straight line reference value. The line length (L) was subtracted from the straight length (sL) and divided by the sL to get a length ratio. For these forests, the length ratio was 0.142 with a standard deviation of 0.101. To account for three-dimensional effects, an average viewing angle of 45 degrees was accounted for. This length ratio is then 0.201 with a standard deviation of 0.143 From the length ratio, an equivalent sinusoidal wave $p=a\cos(2\pi z/\lambda)$ and its corresponding amplitude could be calculated, equating λ with the length of the image With this method, the waviness ratio (a/λ) was calculated to be 0.178±0.14. Recent studies report the length ratio as 0.185±0.1 for ~1 vol.% A-CNTs [18] [84] [85] [86].

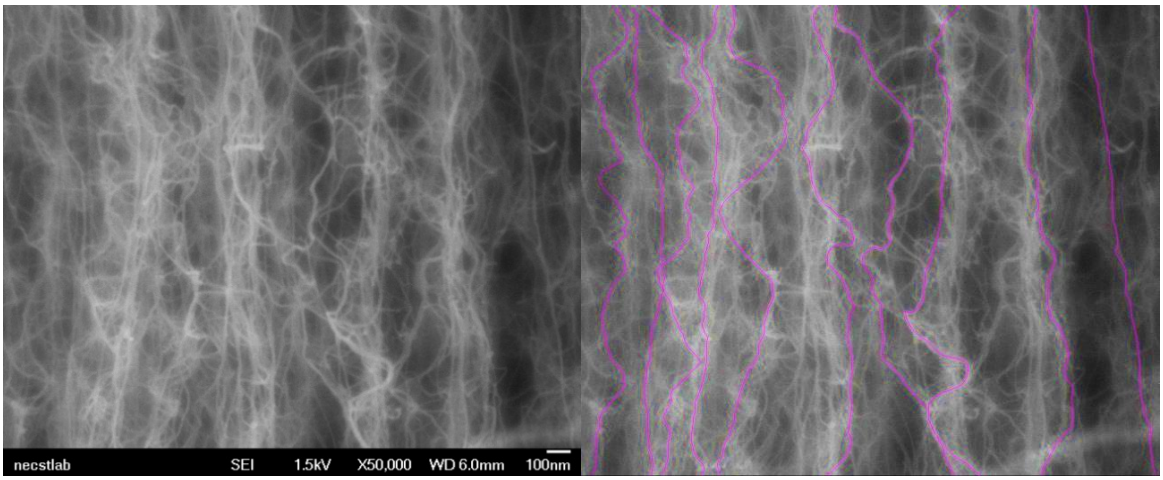

Figure 4-18: Left – original SEM image. Right - SEM image with multiple nanotubes traced with NeuronJ (purple lines).

To compare the waviness to other work done using A-CNTs [87], the images were also put through another ImageJ add-on, OrientationJ. This program calculates the majority orientation in an image and then calculates a 'coherency factor' to that orientation. It is calculated in a similar manner to Herman's Orientation Parameter, except that Herman's Orientation Parameter requires a direction to be specified and measures alignment with that direction. Prior work shows that an as-grown forest has a Herman's Orientation Parameter of 0.37 [87]. The images processed through OrientationJ yield a coherency of 0.3-0.5, however these numbers are highly subject to image processing techniques. See Appendix A for details on calibration checks for OrientationJ calculation of coherency.

4.5.2 Height Measurement with Optical Microscope

Because A-CNT forest height is a parameter being explored in this work, the exact measurement of each forest was crucial to obtain meaningful data. The standard thin film techniques were considered and discarded. SEM measurements are accurate, but it is a time consuming and destructive test that can only be used on representative samples. Non-contact methods such as ellipsometry could not be used due to the low reflectance of the A-CNT forest. Non-contact laser profilometry was attempted, but the equipment used could not simultaneously detect the silicon wafer chip (high reflectance) and the nanotube forest (very low reflectance). In addition, that method required the forest to be scraped off of a portion of the chip (so that the chip was visible), which was undesirable if the forest was to be used. AFM and stylus profilometry were considered, however two issues caused these options to be discarded. First, the tips would sometimes scrape the A-CNT forests off the wafer (note that these forests have been through the delamination step and can be easily removed), and second there was concern that due to the pressure on the tip, the forest could be deformed, resulting in an inaccurate measurement.

Fortunately, a convenient manual solution was found in the lab. An optical microscope in dark field mode could be used to focus on the substrate at the chip edge. The z-axis (vertical) position was recorded, and then the microscope refocused on the top of the forest. This z-axis position could then be subtracted from the previous to determine the height of the forest. The dark field mode on an optical microscope directs light at the sample at an oblique angle; only light reflected from nonuniformities in the sample surface will be seen in the viewport. The top of the A-CNT forest looks like a starfield in this mode. Conveniently, on every edge of the chip there was ~1µm that did not grow nanotubes; this edge could be focused on (Figure 4-19). If the edge was too difficult to focus on by iteself, one could usually find a defect site on the edge; these defects frequently had circular particles that were easy to focus on.

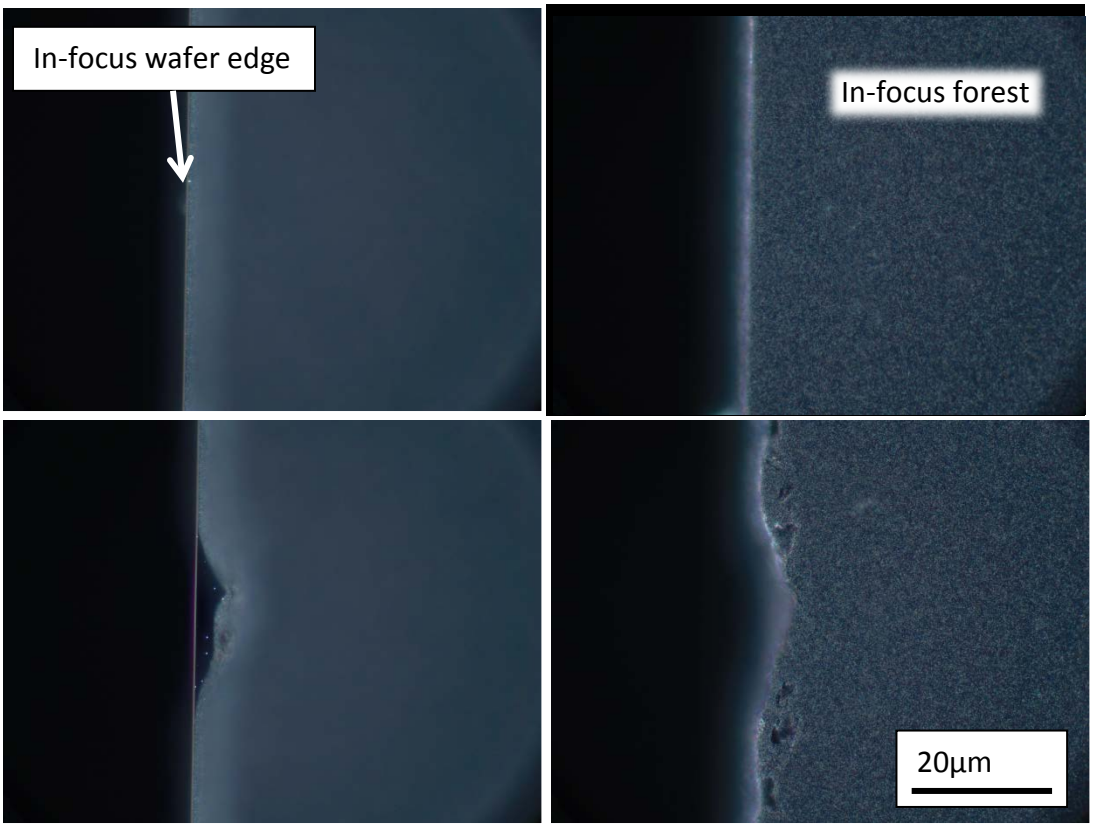

Figure 4-19: Images of chip/forest in dark field mode. Left –focus on chip; right, focus on the top of the nanotube forest. Top – pristine edge measurement. Bottom – defect on edge that allows easier discernment of the chip focal plane.

The technique to measure the A-CNT height this way does take some practice. The low light level in dark field mode requires the light to be turned up to full intensity and the acquisition time to be increased to at least 100ms. In addition, it is sometimes difficult to find the edge of the wafer in dark field mode, so an easier solution is to switch to light field mode to find the silicon wafer edge, then switch back to dark field mode to take the measurements (the

silicon wafer edge can be focused on in either light or dark field mode once found, however the forest is difficult to see in light field mode).

For short forests (<50µm), it is best to use the 50x objective because this objective has a focal depth of 1µm, which reduces error in the measurement. The 20x objective must be used for taller forests because the forest will otherwise touch the objective while the chip's position is being measured. The z-axis position is measured from the handle, and has a precision of 0.5µm and a reported repeatability of 2µm due to the backlash in the gears. This can be somewhat mitigated if the z-axis height is adjusted in the same sequence for every measurement. For example, moving the position down through the focal plane, then slowly back up until the forest/substrate is in focus.

A study was done to determine the accuracy and repeatability of the measurement. To determine the accuracy, three forests were measured using the optical microscope, then cleaved and measured in the SEM. For those forests, the optical microscope underpredicted the heights by 1-1.5µm, therefore the measured accuracy is -1.17µm. Repeatability was studied by measuring ten forests, in two positions, twice each. The gauge variance was calculated from these measurements using the formula, $\hat{\sigma}_{gauge} = \frac{\bar{R}}{d_2}$, where $\bar{R}$ is the average difference in the measurements from a single spot, and d_2 is a coefficient determined by the number of measurements (in this case 2). This formula gives a gauge standard deviation of 0.78µm, meaning that the microscope repeatability is within ±1µm 80% of the time, and within ±2µm 99% of the time. It should be noted that the accuracy (-1.17µm) and repeatability (±2µm) may be different depending on the user of the microscope.

5 Composite Layup and Sample Production

Laminate testing was done using IM7-G/8552 35.2% 160AW unidirectional prepreg from Hexcel [88]. For clarity, we define a *panel*, *sample*, and *coupon* as follows (see Fig. 5.1): ten test coupons are cut out of a given sample, where the sample refers to each interface having the same nanostitch height (or being a baseline). Typically, as in Figure 5-1, 9 samples are fabricated in a single panel, each sample yielding 10 coupons for testing. Each sample is 30 x 40 mm in planform, corresponding to the A-CNT planform of each chip (see Figure 5-1). All samples were made in a quasi-isotropic layup, except two samples (nanostitched and baseline) made in a unidirectional layup to compare the short beam strength (SBS) to the reported values from the manufacturer and literature. The number of plies was determined from the test requirements for short beam strength testing in ASTM D2344 [89]. The minimum thickness is 2mm, which requires 13 plies of the 0.156mm nominal thickness material. For a quasi-isotropic layup the minimum number of plies was then 16 (2.496mm overall nominal thickness). A total of four 30.5cm x 30.5cm (12in x 12in) quasi-isotropic panels were made; an initial panel with seven A-CNT forest heights (samples) was made for static testing, then two panels were made with five and six samples of varying forest heights to compare transfer techniques, and finally one panel with three samples of the same forest height (20µm) was made for fatigue testing. All nanostitched and baseline samples for one transfer technique were made in a single panel to ensure identical processing. A fifth panel, a unidirectional composite layup, was 10cm x 10cm (4in x 4in) and made with the same number of plies to ensure comparable results.

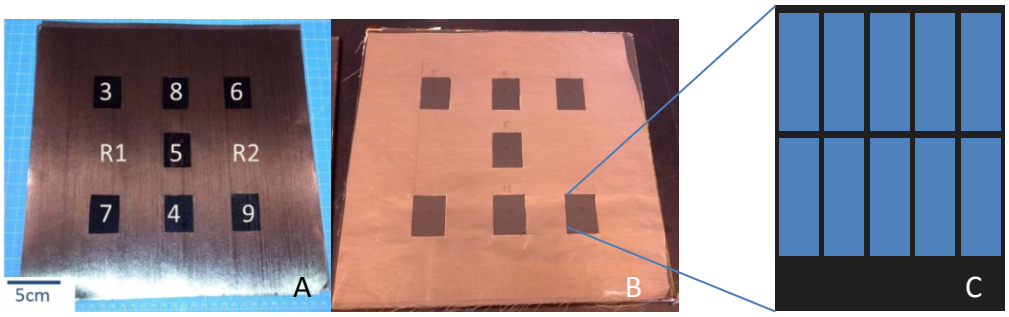

Figure 5-1: Layup of panel 1. A) individual 0- degree ply showing nanostitch placement and sample numbers. B) GNPT template overlaying the cured panel for marking. C) Schematic of coupon cutout from sample.

Because the sample production involves concurrent techniques that may be difficult to conceptualize all at once, the chapter is broken up into three parts; the layup technique used in section 5.1 (involving both the standard layup procedure and the A-CNT transfer technique), the actual sample production in section 5.2, and the analysis of the resulting samples' interface morphology in section 5.3.

5.1 Layup Technique

Both the standard layup and nanostitch transfer techniques are described, as well as factors affecting transfer quality.

5.1.1 Standard Layup Procedure

Prepreg was obtained from Hexcel in a 1.23m (4ft) wide, 30.5m (100ft) long roll. According to manufacturer's specifications, it was stored in a freezer at -20°C to preserve its one-year shelf life. At room temperature, the prepreg has an 'out-life' of 30 days before it becomes unusable; every time the roll is removed from the freezer, the time at room temperature is recorded to ensure the total time does not exceed this specification.

The first step in preparing a laminated composite was to remove the prepreg from the freezer and let it warm up to room temperature while protected inside its sealed plastic bag. The warming process must be done inside the plastic because condensation from ambient humidity will otherwise be absorbed by the prepreg, later causing voids during cure. This warming process takes 3-4 hrs. Once the prepreg reached room temperature, it was removed from the plastic bag and hung on a rod to make dispensing easier. To make the quasi-isotropic layup, the prepreg was unrolled and cut into 30.5cm (12in) and 43.2cm (17in) swaths: the 30.5cm swaths were used to prepare the 0° and 90° plies by cutting into precise 30.5cm squares, and the 43.2cm swaths were used to prepare the 45° plies by cutting the 30.5cm x 30.5cm square from a rotated angle. Care was taken to ensure squareness and precision by using a Teflon-backed ruler and a cutting mat with a square grid. A brand-new razor was used for the cuts, and replaced every 3-4 cuts to maintain the sharp edge: this prevented displacement of carbon fiber caused by dragging with a dull blade. Once the swaths were cut, the rest of the prepreg was resealed in its plastic bag and returned to the freezer.

It should be noted that the recommended layup procedure occurs in a clean-room environment [90]. While the lab bench, surrounding areas, tools and labcoat were cleaned and kept as pristine as possible, the lab where the layup was performed was not a clean-room. Because of this, a protective film – vacuum bagging material (blue roll found in lab, no product number) – was laid over the prepreg as it was unrolled from the large spool to protect the prepreg surface from ambient dust, and wasn't removed until the prepreg ply was put onto the layup. The underside of the prepreg is already protected by a backing material.

Once the prepreg plies were cut, they were laid up in the following manner. First, a piece of polyester peel ply (a product used to give surface finishes, provide an air migration path and isolate the prepreg from the rest of the vacuum materials, e.g., Airtech Econoply J) was cut to ~35cm x 35cm (~14in x 14in) and taped to the work surface. The prepreg plies were piled in the sequence in which they were to be laid up, the orientations checked prior to starting. The first ply's protective film was removed and it was placed exposed-side down

directly onto the peel ply (roughly centered). A 10cm-wide roller was used with high hand pressure to flatten, remove air pockets and stick the prepreg ply to the peel ply. The backing was removed from that ply, then the next ply was laid onto the first in the same manner (Figure 5-3). To maintain the 30.5cm x30.5cm (12in x 12in) dimensions of the layup, the subsequent plies were laid up by carefully aligning one edge and corner to the stack below it (the chosen corner and side were the same for all plies) by hand (no jig was used). When compressing the stack with the roller, the rolling direction should be parallel to the fiber orientation in the ply that is currently on top – this minimizes the fibers migrating in the uncured epoxy. Once the final ply was adhered to the stack, a second piece of peel ply was cut and put on the top of the stack. The peel ply was trimmed close (within a few mm) to the sample on three sides. The fourth side of the peel ply was left untrimmed and folded next to the sample – this was done for two reasons: first to have a continuous air migration path next to the sample and secondly to have an accessible section for easy removal after cure. The completed stack (panel) was then ready to be packaged for the autoclave.

To package the panels for the autoclave run, the following materials were needed: a 30.5cm x 30.5cm (12in x12in) Al caul plate, two sheets of 35cm x 35cm (14in x 14in) guaranteed nonporous Teflon film (GNPT) and one of 28cm x 28cm (11in x 11in), and flash tape (Airtech Flashbreaker 1). The caul plate was cleaned, flatness was checked with a straightedge, and then it was wrapped using the 28cm x 28cm piece of GNPT and one 30.5cm x 30.5cm piece of GNPT. The smaller GNPT piece was put on top of the caul plate, and the large piece was wrapped around the underside and secured to the GNPT on top with the flash tape. Once wrapped, the underside of the caul plate was then checked to ensure there were no wrinkles or bumps in the surface (as these surface features would be transferred to the composite). Then the prepreg stack was placed on the second piece of 14in x 14in GNPT, the wrapped caul plate placed directly on top (with the underside making contact with the prepreg stack). The edges of the 14in x 14in GNPT were then taped to the top of the caul plate package as was done with the previous sheet, making a complete package containing the prepreg stack.

Figure 5-2: Complete package ready for autoclave. Caul plate (grey) wrapped in GNPT (brown), placed on top of the laminate (black) wrapped in peel ply (yellow). The whole thing is wrapped in GNPT.

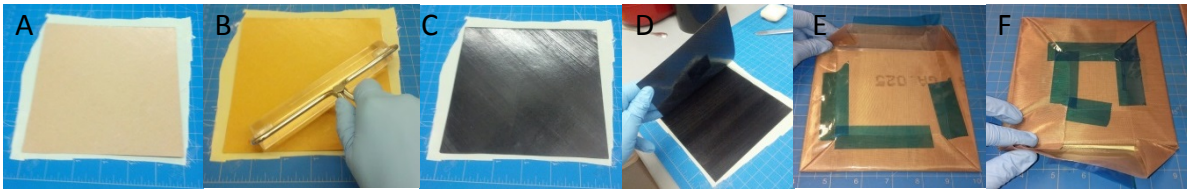

Figure 5-3: Layup procedure on a 15cm x 15cm (6in x 6in) panel. A) Begin by putting first prepreg ply facedown on top of peel ply (yellow). B) Use roller with high pressure to flatten. C) Remove Backing (-45 degree ply shown) D) Put another piece of prepreg down in the same manner on top of the first. Repeat B-D until layup is complete. E) Cover caul plate using a piece smaller than the plate on top and wrapping a larger piece around the whole thing, securing to the top with flash tape. F) Once this is done, place layup on another piece of GNPT, put caul plate on top and again wrap the GNPT around to the top and secure with flash tape.

The autoclave used in this work was off campus, at Natick Army Labs. Therefore, the autoclave run could not be done on the same day as the layup and packaging. Due to this, the caul plate package was sealed in a plastic bag and refrozen until the run could take place. Once at Natick, the caul plate package was vacuum bagged using the following procedure. The caul plate package was placed prepreg-side-up on top of breather material, such that when vacuum was applied, the vacuum bag was directly in contact with the prepreg side. As vacuum was being applied, care was taken to ensure no wrinkles on top of the prepreg stack. Note that this method essentially uses the caul plate as a baseplate, with no rigid top plate (section X2.4, technique #3 in [90]). The composite was then cured according to manufacturer's specifications for monolithic parts [88]:

1. Apply full vacuum (1 bar).
2. Apply 7 bar gauge autoclave pressure.
3. Reduce the vacuum to a safety value of 0.2 bar when the autoclave pressure reaches approximately 1 bar gauge.
4. Heat at 1- 3°C/min (2-8°F/min) to 110°C ± 5°C (230°F ± 9°F)
5. Hold at 110°C ± 5°C (230°F ± 9°F) for 60 minutes ± 5 minutes.
6. Heat at 1-3°C/min (2-8°F/min) to 180°C ± 5°C (356°F ± 9°F)
7. Hold at 180°C ± 5°C (356°F ± 9°F) for 120 minutes ± 5 minutes.
8. Cool at 2 - 5°C (4-9°F) per minute
9. Vent autoclave pressure when the component reaches 60°C (140°F) or below.

5.1.2 Transfer Techniques

To create nanostitch, aligned carbon nanotube (A-CNT) forests must be placed between each layer of carbon fiber prepreg during layup. In order to transfer the carbon nanotubes to the prepreg, the prepreg must be warmed to decrease the viscosity of the epoxy and provide a tacky surface so that the carbon nanotube forest will reliably transfer when the CNT-laden silicon wafer chip is pressed onto it. In previous work, the prepreg was taped to a roller, heated with a heat gun, and then rolled over the chip to transfer the forest [14]. In this work, the prepreg was heated in a more controlled manner by using a hot plate. Two methods have been developed, varying the temperature and pressure of transfer. The first, Method 1, uses a 40°C

temperature to just make the prepreg tacky, then pressure is applied by hand with a roller to transfer the forest by adhering it to the prepreg. Method 2 uses a 60°C temperature and a longer time to transfer without rolling (no pressure applied) by allowing the prepreg epoxy to wick into the forest. The methods are summarized below.

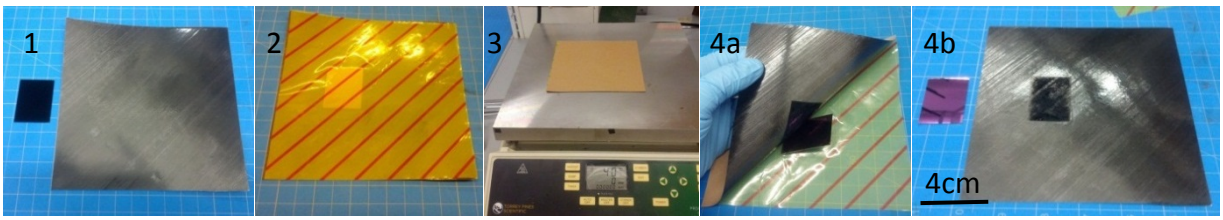

Figure 5-4: Layup procedure, Method 1. Left to right – 1. Begin with prepreg (45 degree ply shown) and A-CNT laden chip, 2. Press chip facedown onto prepreg and cover with protective film. 3. Heat for 2 mins at 40°C, chip side down (then apply pressure, not shown), 4a.Remove protective film; chip easily peels away, 4b. leaving nanostitch behind.

Method 1 (see Figure 5-4):

1. Begin with forest on wafer chip and a ply of prepreg.
2. Press chip facedown onto prepreg, then cover with protective film
3. Place chip-side-down on hot plate, heat for 2 min at 40°C, then apply pressure with roller
4. Remove protective film: a) chip easily peels away, b) leaving nanostitch behind

Plies can then be laid up as normal (roller each layer with heavy hand pressure)

Method 2:

1. Begin with forest on wafer chip and a ply of prepreg
2. Place chip facedown on prepreg
3. Place prepreg chip-side-up onto hot plate, heat for one minute at 60°C
4. Remove chip, leaving nanostitch behind. Return prepreg to hot plate until forest wicks into epoxy (Figure 5-5). The forest is seen to turn grey when this happens. The time required is dependent on the forest height, about 1 min per 5µm.
5. Place the ply onto the prepreg stack, then return stack (new ply side up) to hot plate for one minute to allow forest to wick into the adjacent ply.
6. Remove stack from hot plate and roller the stack as normal.

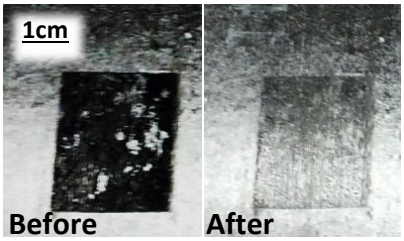

Figure 5-5: Greying of CNT forest as epoxy wicks in (step 4, Method 2). 89% transfer of forest shown.

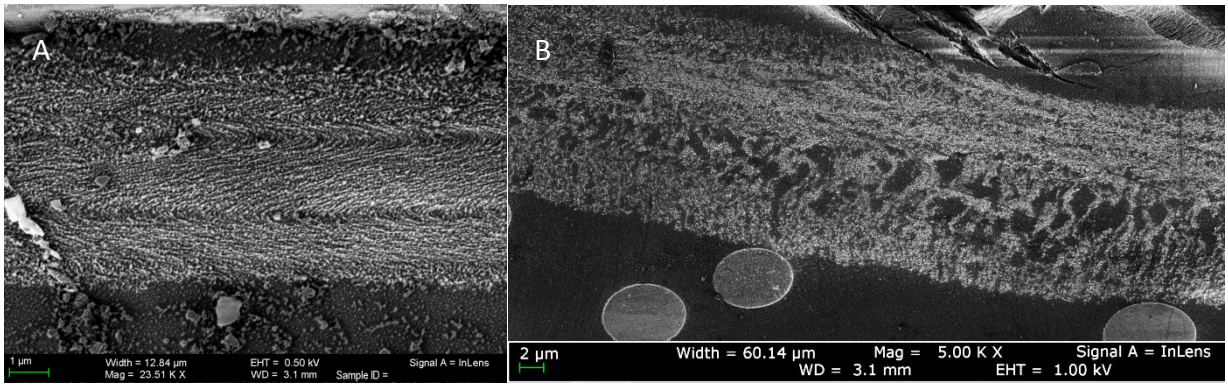

Figure 5-6: Interlaminar region morphology differences between Method 1 (A) and Method 2 (B). Note the difference in scale; while both forests began at 20µm tall as-grown, the left nanostitch is 5µm tall, while the right is 19µm.

The two methods yield drastically different A-CNT morphologies in the composite, as shown in Figure 5-6. Method 1 compresses the forest into a tight band (~5µm), while Method 2 more closely preserves the original CNT forest height.

The ability to change the morphology of the forest is extremely interesting from a modeling perspective, and may have an impact on the resulting composite properties. For instance, the higher packing fraction of CNTs in Method 1 may be expected to reinforce better than Method 2. The effect on SBS is discussed in Chapter 6.

5.1.3 Factors Affecting Transfer Quality

The success of the transfer methods is foremost dependent on the delamination step in the growth process. If the nanotube-catalyst interface is not sufficiently etched, the forest will not detach from the wafer chip in one piece, resulting in patchy, partial transfer, regardless of the soundness of the transfer method. If the transferred forest shows distinct holes (Figure 5-7), the delamination step in the growth process should be lengthened.

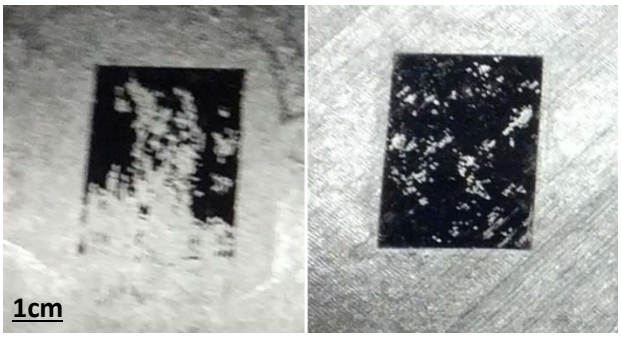

Figure 5-7: Two transfers to prepreg showing transfer defects attributed to insufficient delamination time in the growth. Left – very poor transfer (55%), most likely from an operator error that shut off water too early, Right – 90% transfer showing small missing patches, indicating delamination time should be increased.

The amount of pressure applied as well as the technique is very important in Method 1. If insufficient pressure is applied, the A-CNTs will only transfer on the peaks – namely the high points of the texture caused by the carbon fibers. In addition, better transfer is obtained if

pressure is applied to the prepreg side rather than the chip. The prepreg is flexible and with pressure will conform to the chip. Conversely, if pressure is applied to the chip it can result in uneven pressure on the prepreg (due to its texture). This can result in striated transfer as shown in Figure 5-8a. In Method 2, it is very important that the prepreg is macroscopically flat. Striated transfer can result if the prepreg isn't flat, as very little pressure (the weight of the chip and any errant finger pressure during placement) is applied to the chip and parts of the forest that are not in any contact with the prepreg will not transfer at all (Figure 5-8b). Small amounts of pressure in Method 2 on the back of the chip while it's on the hot plate (during step 3) can mitigate this, but can result in interesting finger patterns if not done carefully (Figure 5-8c).

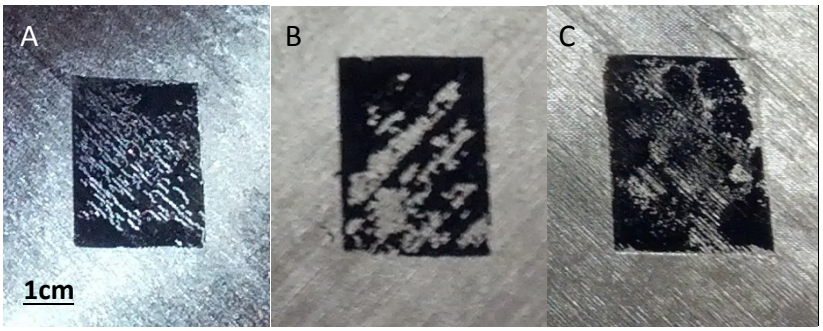

Figure 5-8: Defects in nanostitch due to pressure inconsistencies. A) striations due to insufficient pressure in Method 1. B) striations due to uneven prepreg during Method 2 layup. C) finger marks apparent from uneven prepreg and an attempt to gently push it flat from the back of the chip (Method 2).

In addition, the transfer step must be done fastidiously. If the chips are adjusted during placement, or shift while moving the prepreg to the hotplate, the forest can split and shift in independent blocks, leaving places in the prepreg where the forest has bunched together, and others where there are no nanotubes (Figure 5-9).

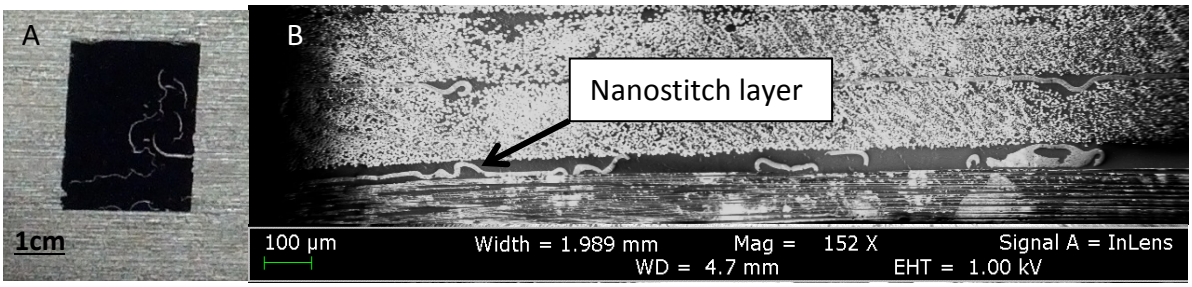

Figure 5-9: Defects in nanostitch due to the chip shifting during transfer. A) macroscopic picture showing visible gaps in the transferred forest. B) SEM of a nanostitch layer that has the bunching and gaps associated with this transfer error.

5.2 Sample Production

Three sets of samples were produced in this thesis. The first sample set was a preliminary test done to explore A-CNT height's effect on the resulting short beam shear strength (SBS). The first sample set used Method 1 transfer and a quasi-isotropic layup (Panel 1) for height exploration and a unidirectional layup (Panel 2) to compare the unidirectional SBS to the values

reported in literature and on the Hexcel data sheet [19]. The second set of samples explored the two different transfer techniques as well as continued the height exploration for each. Two quasi-isotropic panels were created: Panel 3 used transfer Method 1, and Panel 4 used transfer Method 2. Finally, a third sample set was produced for fatigue testing. This sample set consisted of a single quasi-isotropic panel, with three samples of an A-CNT height of 12.5µm laid up with Method 1.

5.2.1 First Sample Set – Height Exploration with Method 1 Transfer

The interface thickness (the resin-rich region between two plies) was reputed to be 7µm, and the IM7 carbon fibers in the plies have a diameter of 5µm. It was hypothesized that the ideal A-CNT forest height for nanostitch would be the interface thickness plus one to two carbon fiber diameters. This would be sufficient to bridge the resin interface and interdigitate with the first layer of carbon fibers on each side of the interface, without creating an additional interlayer that could be expected from longer forests that might not be able to migrate deeper into the ply. Therefore the height of the A-CNTs should be 12-17µm. To determine if this hypothesis was correct, the preliminary testing for Method 1 transfer was undertaken using a range of heights 5-25 micrometers. A-CNT forests were grown at heights between 4 and 29 micrometers, and binned into seven groups at 5, 10, 12.5, 15, 17.5, 20, and 25 micrometers. A separate set of 20µm forests was grown to test nanostitch in a unidirectional composite. To create a sample, fifteen forests were needed in each height group to reinforce each interface in a 16-layer composite. All forest heights had a tolerance of ±1µm except the 25µm, which contained forests ±3µm.

To create Panel 1, seven A-CNT sample heights were laid up in a single 30.5cm x 30.5cm (12in x 12in) quasi-isotropic laminate from Hexcel UD prepreg (IM7-G/8552, 35.2%, 160AW: Part #110845, Lot DP12716-14, Spool 13). The placement of the varying heights and the two reference samples were randomized to negate any possible effects of nonuniformity in laminate quality (see Figure 5-1A). A-CNT forests were spaced at least 2.5cm apart and sufficiently far from the laminate edges to prevent interfering effects. To keep the A-CNT forests aligned throughout the laminate thickness, placement was done using a GNPT template Figure 5-1b. Windows 3.0cmx4.0cm were cut in the 30.5cm x 30.5cm template. One corner and edge of the template was carefully lined up by hand with the corner and edge of the prepreg ply, and then the A-CNT laden chips were placed forest-side-down in each of the windows. The GNPT template was carefully removed while keeping the chips in place, and the protective film put in place over the top of the chips. Method 1 (Section 5.1.2) was used to transfer the forests. When laying up the composite, the same corner and edge were used to line up the prepreg plies, resulting in the A-CNT patches being directly on top of one another. An error during layup resulted in a $[0/90/+45/-45/90/0/+45/-45]_S$ quasi-isotropic laminate, rather than the intended

$[0/90/+45/-45]_{2S}$. Because the layup remained symmetric, it was not thought to significantly impact the results of this preliminary investigation.

The unidirectional panel (Panel 2) was made in a similar way with 4in x 4in size prepreg sheets and an appropriate GNPT template. The small size of the laminate is due to only needing two sample areas (one nanostitch and one reference); a 2.5cm boundary could still be maintained around all edges. Figure 5-10 shows the forest placement. Fifteen 20µm forests were used to reinforce each interface in the 16 layer unidirectional composite. All layers were oriented at zero-degrees to the laminate axis obtain the unidirectional composite panel.

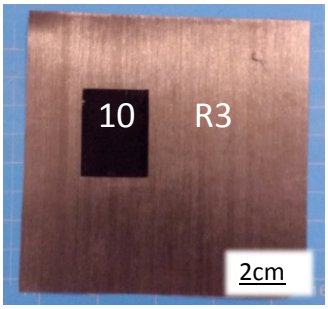

Figure 5-10: Unidirectional layup of panel 2.

All A-CNT transfers were photographed and the percentage transfer estimated. When possible (when the images had high enough contrast), the percentage transfer estimate was verified by ImageJ by converting the image to binary and measuring the percentage of black pixels in the transfer region. The quasi-isotropic layup had 84-99% transfer success, depending on the height of the forest and the position relative to the corners that were handled. The best transfer was observed on the A-CNT forests nearest to the corner that was held while moving the prepreg to the hot plate. The worst transfer was seen on the opposite corner, possibly due to the wafer chip shifting during the movement of the prepreg. Otherwise, transfer efficiency increased with increasing forest height, as shown in Figure 5-11. This is most likely due to the increasing conformability of the taller forests to the microscopically rough prepreg surface. The unidirectional panel had 99% transfer on its 20µm forests, due to the small sample size and ease of handling just one wafer chip at a time.

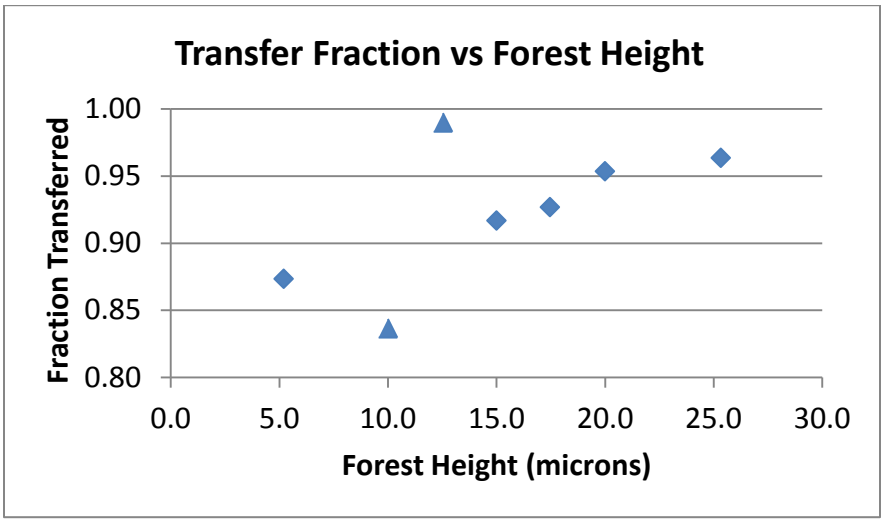

Figure 5-11: Transfer fraction vs. forest height for panel 1, Method 1. Data shows trend of increasing transfer fraction with increasing height. Handling nonuniformities (triangular data points) are noted.

Both panels 1 and 2 were autoclaved in the same run according to manufacturer's specifications. Nanostitch and reference sample areas (3cm x 4cm) were identified, labeled and cut out of the composite panel using a wet cutoff tile saw (Dewalt, 6000rpm max) with a Dewalt 10in wet diamond circular saw blade. The sample thicknesses were measured to determine the necessary width and length of the test coupons. The average was 2.555mm, 2.12% thicker than the nominal 2.496mm. There were no statistical differences between the reference (2.58±0.01mm) and the nanostitched samples (2.55±0.05mm), and there was no correlation of thickness to nanostitch height. (± here and throughout refers to standard deviation unless otherwise noted.) From ASTM D2344 [89], the coupon width and length were required to be 2.0x the laminate thickness (5.1mm) and 6x the thickness (15.3mm), respectively. These samples were then cut into 11 coupons in the configuration shown in Figure 5-1.

To cut out the coupons, each sample was adhered to a sacrificial substrate (fiberglass) using double-sided tape and mounted to a Bridgeport x-y stage, and a dremel with a 0.5mm width diamond cutting disc (SE DW13) was fixed overhead. This tool was used due to its small 0.8-mm wide kerf, which allowed the 30mm-wide samples to be cut into five 5.2mm wide strips (26mm+3.2mm = 29.2), from which two 15.4mm long coupons were cut per strip (see Figure 5-1c). In addition, one coupon from the remaining piece was cut at a 90-degree orientation for possible use in other tests (eg. density, void content). During cutting, a shop vacuum with a hepa filter was used with the nozzle mounted ~3cm from the sample to aspirate the generated particles. All samples were then wet-polished to final dimensions of 5.1x15.3mm using 800, then 1200 grit sandpaper on a polishing wheel. An edge on one coupon from each sample was polished to mirror finish (using 4000 grit sandpaper, then 0.3µm polishing compound) and plasma etched for SEM imaging. See Table 5-1 for final dimensions and tolerances.

SEM images of the sample interfaces showed that the A-CNT forests, regardless of initial height, were distorted and compressed to ~5µm in the interface (discussed in more detail in section 5.3). This gave impetus to develop a new transfer method (Method 2) towards preserving the original forest morphology, and a new round of samples to compare Method 1 and Method 2 transfer was made.

5.2.2 Second Sample Set– Comparing Method 1 and Method 2 Transfer

Two $[0/90/+45/-45]_{2S}$ quasi-isotropic composite panels were made with the same stock of UD prepreg, one with each type of transfer method. Panel 3 (see Figure 5-12a), made with Method 1, expanded the range of nanotube heights, exploring the 15-62.5 micron range with six forest heights (15,20,30,45,55,and 62.5µm). The A-CNT height of 15 and 20 µm were chosen to compare to the previous layup, and the increased height range to determine if there would be an optimum in that range. Panel 4 (see Figure 5-12b), made with Method 2 was produced

with five forest heights in the 10-35 micron range. Again the placement of heights was randomized, and a GNPT template was used to align the A-CNT nanostitch on each ply.

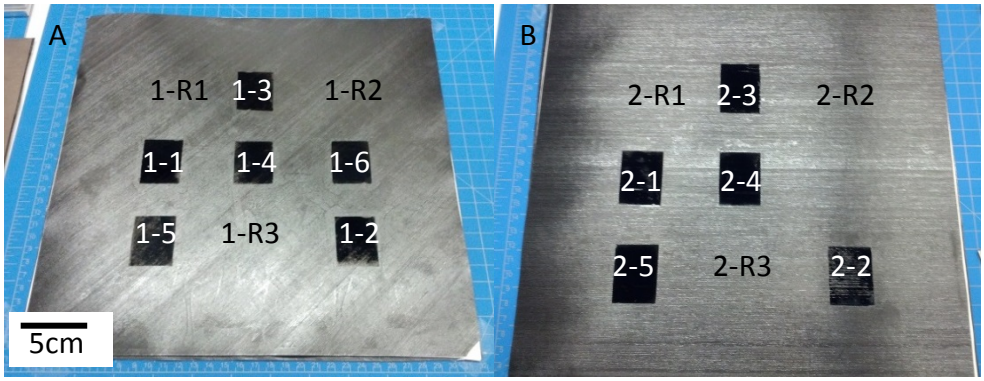

Figure 5-12: Placement of forests in composite panels. A) Method 1, panel 3. B) Method 2, panel 4.

Transfer of the forests to the prepreg plies was less optimal for the second round samples (see Figure 5-13). Transferring shorter forests (10-15µm) with Method 2 was difficult due to the imposed restriction on pressure application. If the prepreg was rippled/undulated, the transfer did not work well for the shorter forests. In Method 2, the low transfer percentage for the 10µm sample was due to three incomplete transfers on layers 7 (55%), 8 (50%) and 9 (40%). The bad transfers are very close to the center of the composite, and they are suspected to heavily influence the resulting interlaminar shear strength of that sample. The 15µm Method 1 sample had one very bad transfer (20%) at a 90/45 interface that brought down the average. All other samples averaged 93% transfer, with half of the transfers achieving 100% transfer for both methods.

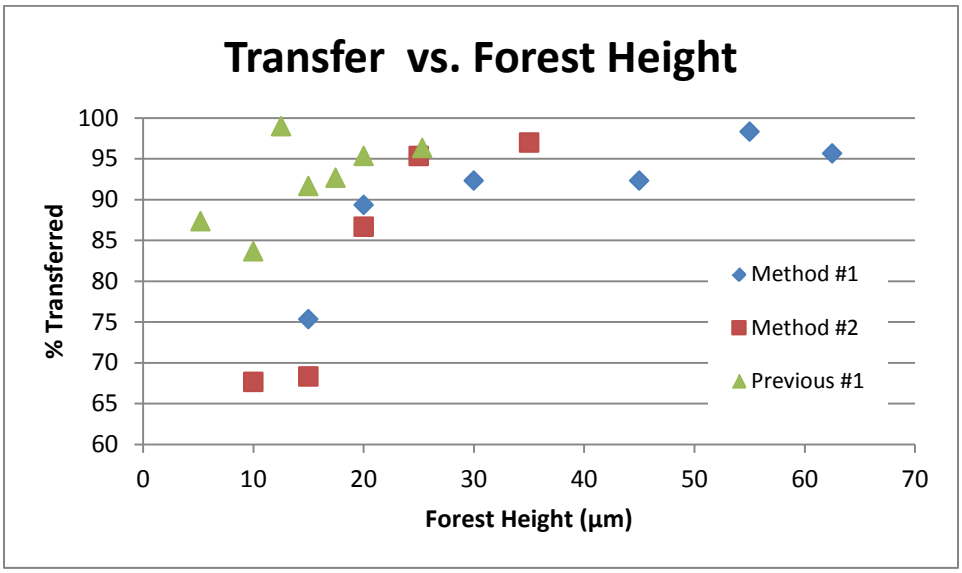

Figure 5-13: Transfer percentage vs. forest height, sample sets 1 and 2.

Laminate thickness vs. height was measured in these samples, and for these laminates the forest height range was large enough to discern the trend in Figure 5-14. For Method 1, the composite thickness remained within standard deviation of the reference samples until the A-CNT height reached 30µm, then increased as a function of the square of the A-CNT height to an addition of 60 µm for a 62.5µm tall forest. Note that there are 15 ply interfaces each with a 62.5µm forest, while the added thickness equates to an addition of 4µm per interface. For Method 2, the laminate thickness increased an average of 40µm for all nanostitched samples 10-35µm, an average of 2.7µm per interface.

Assuming full resin infiltration, 1.5 vol% fraction of grown A-CNTs would yield a thickness increase of 0.015microns/micron of forest per interface, or with fifteen interfaces, 0.225µm added thickness to the laminate per micron of forest (eg. A 10µm tall forest would yield a minimum added laminate thickness of 2.3µm, while 62.5µm gives a minimum 14µm increase in laminate thickness). The disparity between the minimum increase and the actual increase may be due to the nanotubes wicking in and retaining extra polymer that would otherwise find its way out of the composite. Alternatively, the nanotubes might locally alter the density of the polymer through altering its crystallinity and chain organization. Both hypotheses explain the differences seen in the Method 1 vs. Method 2 samples, however neither was tested in this thesis.

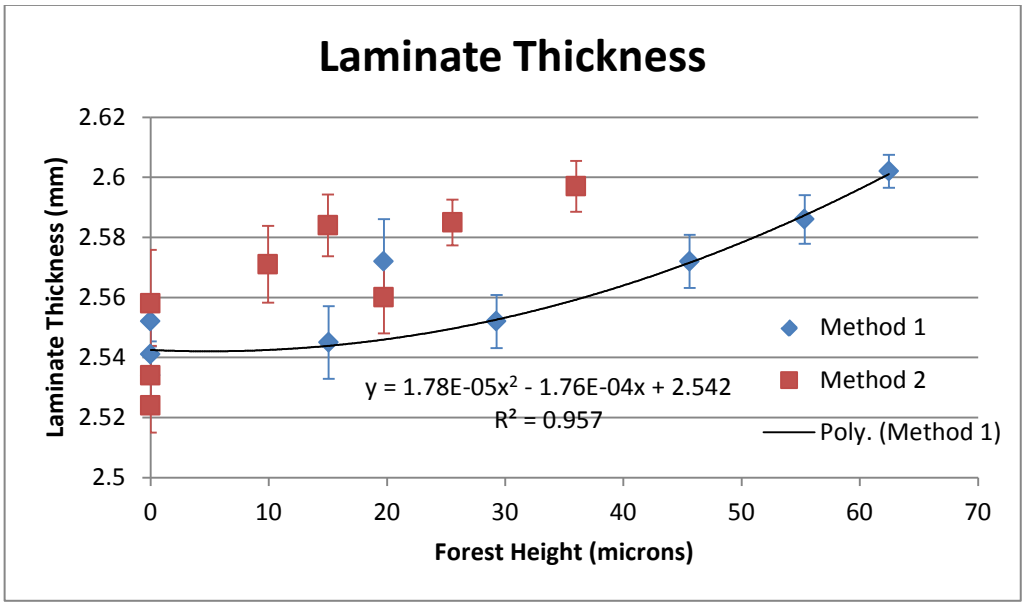

Figure 5-14: Laminate thickness for round 2 samples, plotted with 95% confidence on the means (2SE). A polynomial is fitted to the Method 1 data, excluding the 20µm data point.

The second sample set laminates were autoclaved according to manufacturer's specifications in the same manner as the previous laminate, and again the samples were cut out using the wet cutoff saw with an abrasive diamond wheel. Eleven coupons were cut out of

each sample in the same manner as the first sample set samples, and polished with 1200 grit sandpaper to final dimension of 5.1x15.3mm. One coupon from each sample was polished to mirror finished and plasma etched for SEM imaging.

5.2.3 Third Sample Set - Fatigue Samples

Once the static short beam shear strength testing was complete, a set of sample were created for fatigue testing. Again a 30.5cm x 30.5cm (12in x 12in) quasi-isotropic $[0/90/+45/-45]_{2S}$ laminate (panel 5) was produced from IM7/8552, 0.156 nominal thickness material (IM7-G/8552, 35.2%, 160AW). The composite was made with three nanostitched areas of the same forest height to produce 30 samples for fatigue testing. The height and layup method were chosen based on the second round samples. The undesireable potential laminate thickness increase deterred the use of Method 2 and encouraged the use of short (<20µm) forests transferred by Method 1. A height of 12.5µm was chosen to minimize the chance of laminate thickness increase while maximizing transferability. See Figure 5-15 for sample placement.

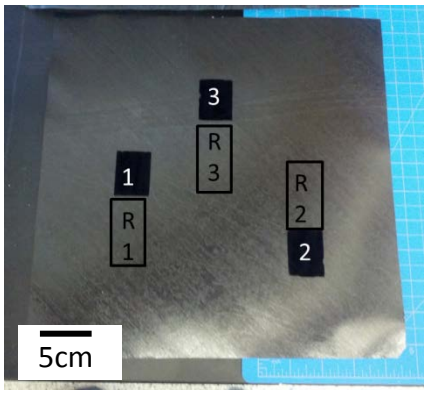

Figure 5-15: Panel 5, fatigue sample layout on 45 degree ply.

The transfer of A-CNT forests in this layup was effectively 100%. Only four of the 45 forests had any defects and those were minimal (>98% transfer). The increase in transfer yield from 93 to 100% was most likely due simply to increased proficiency in handling the samples. The panel was autoclaved according to manufacturer's specifications, the nanostitched samples plus three reference samples (Figure 5-15) cut out of the panel using a wet diamond saw and the coupons cut out of the samples in the same configuration as before (see Figure 5-1c). Coupons were polished to approximate dimensions of 5.0x15.3mm (Table 5-1).The average thickness of the coupons was 2.599mm with no statistical difference between reference and nanostitched samples.

Table 5-1: Average sample measurements (10 coupons per sample)

Sample	Forest Height (μm)		Thickeness (mm)		Width (mm)		Transfer
	Average	StDev	Average	StDev	Average	StDev	% Transfer
First Sample Set, Panel 1, Method 1							
ref1	0		2.576	0.015	5.036	0.080	
ref2	0		2.586	0.019	5.056	0.075	
8	5.2	0.7	2.500	0.021	5.100	0.055	87
9	10.0	1.0	2.562	0.020	5.096	0.029	84
3	12.5	0.5	2.476	0.015	5.102	0.004	99
4	15.0	0.8	2.574	0.024	5.066	0.066	92
5	17.5	0.5	2.642	0.007	5.074	0.027	93
6	20.0	0.7	2.544	0.016	5.072	0.040	95
7	25.3	2.1	2.534	0.024	5.084	0.050	96
First Sample Set, Panel 2, Unidirectional, Method 1							
Ref3	0.0		2.566	0.026	5.068	0.015	
10	19.8	0.9	2.572	0.047	5.052	0.019	99
Second Sample Set, Panel 3, Method 1							
1--ref1	0		2.552	0.013	5.072	0.202	
1--ref2	0		2.541	0.023	5.126	0.030	
1--ref3	0		2.534	0.018	5.100	0.047	
1--1	15.1	1.3	2.545	0.019	5.074	0.098	75
1--2	19.7	2.2	2.572	0.022	5.102	0.037	89
1--3	29.3	1.6	2.552	0.014	5.095	0.036	92
1--4	45.6	2.2	2.572	0.014	5.114	0.034	92
1--5	55.3	1.2	2.586	0.013	5.106	0.027	98
1--6	62.5	3.3	2.602	0.009	5.128	0.044	96
Second Sample Set, Panel 4, Method 2							
2--r1	0		2.534	0.016	4.896	0.217	
2--r2	0		2.558	0.028	4.905	0.151	
2--r3	0		2.524	0.014	5.064	0.054	
2--1	9.9	1.5	2.571	0.020	5.115	0.067	68
2--2	15.0	1.2	2.584	0.016	5.120	0.070	68
2--3	19.7	2.3	2.560	0.019	5.113	0.057	87
2--4	25.5	0.8	2.585	0.012	5.119	0.055	95
2--5	36.0	2.0	2.597	0.013	5.112	0.059	97
Third Sample Set, Panel 5, Fatigue Samples, Method 1							
F-Ref	0		2.613	0.024	4.951	0.040	
F-nano	12.5	1.5	2.584	0.033	4.952	0.027	100

5.3 Interface Characterization

Interface morphology is paramount to the understanding of the CNT effects on the laminate interfacial strengths reported in Chapter 6. Quantities such as interface thickness and the variation thereof must be obtained. In addition, the morphology of the forest in the composite material can change significantly – CNTs can bunch together during capillary driven wetting, compress under loads from the layup technique, and change waviness or orientation. Moreover, the percentage of the interface that is filled with CNTs may have a large effect on the data and must also be evaluated.

To quantify the interface morphology, coupons from every sample in every panel were highly polished (800-4000 grit wet polish, then polished with 0.3µm alumina polishing compound), plasma etched (ISN, Harric PDC-32G plasma cleaner, with 'high' and 'low' power settings) for 30 seconds to 1 minute, and SEM imaged. The samples from the first sample set were plasma etched for one minute on 'high' power in air. The images showed that the carbon fibers were being damaged by this process (see Figure 5-16, left), so subsequent samples (Sample sets 2 and 3) were plasma etched on 'low' power in air for only 30 seconds. It is unclear whether the plasma etch step is necessary for future work; it was intended to ablate a surface layer of the polymer (especially any remaining polishing scratches) so that the nanotubes would be more visible. Figure 5-16, right shows the difference between a one-minute plasma etched area and an area that was masked. The left-hand side of that image shows the irregular surface and visible nanotubes left from the aggressive plasma etch; the lower right hand corner shows a typical polished-only surface for panel 1 samples, where the nanotube layer is visible but individual CNTs/bundles of CNTs are not.

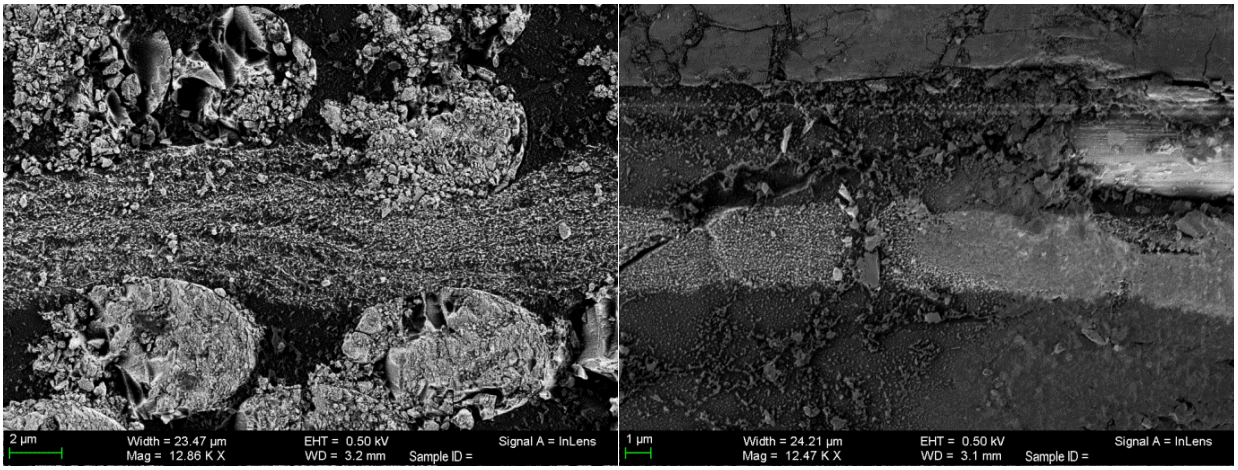

Figure 5-16: Left: damage to carbon fibers from one minute plasma etch. (Image from Panel 1, sample 4) Right: Inconsistent plasma etch. Image's left shows one minute plasma etch; the lower right corner does not appear to be plasma etched (Image from panel 2, sample 10).

Each interface in every polished and plasma etched coupon was imaged. The interface thickness, nanostitch height, and percentage of the interface filled with nanotubes were

measured from every image by measuring the total area of the interface and dividing by the width of the interface. The total area of the interface was obtained by making a polygon from peak-to-peak of the carbon fibers on either edge of the interface (see Figure 5-17). The analysis tool was then used to calculate the area of the polygon. The outline of the forest was traced in the same manner and the area measured in the same way. The percentage fill was calculated by dividing the nanostitch area by the interface area.

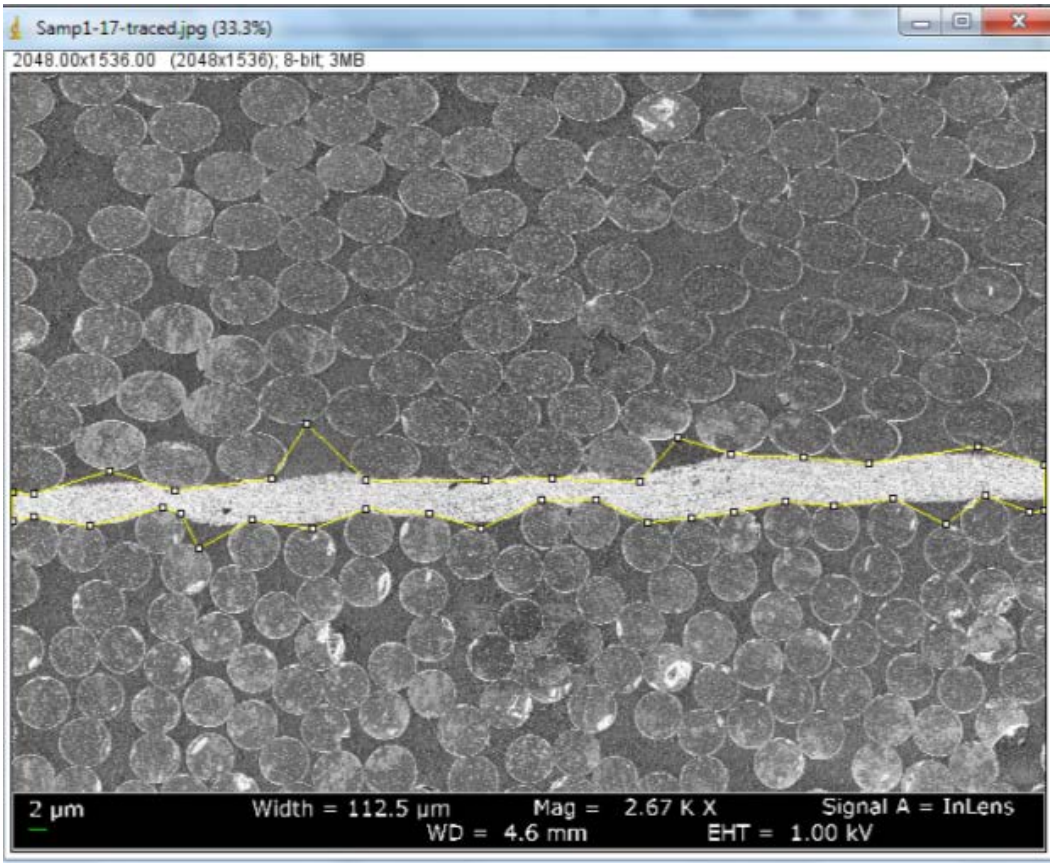

Figure 5-17: Traced outline of interface (yellow) in a nanostitched coupon to determine the interface area in ImageJ. Interface from panel 3, sample 1-1.

5.3.1 First Sample Set

The first samples were imaged at a magnification of 2,000x, yielding an image width of 150µm. In the unidirectional sample, it was impossible to determine the locations of the interface in the majority of cases due to the ability of the plies to nest together. The interface location could be estimated by using the nominal ply thickness of 156µm to spatially map where the interface should be, but an exact location could not be seen (see example in Figure 5-18). In addition, the nanostitch layer was equally hard to identify, discernable only from the difference in texture (confirmed at higher magnifications).

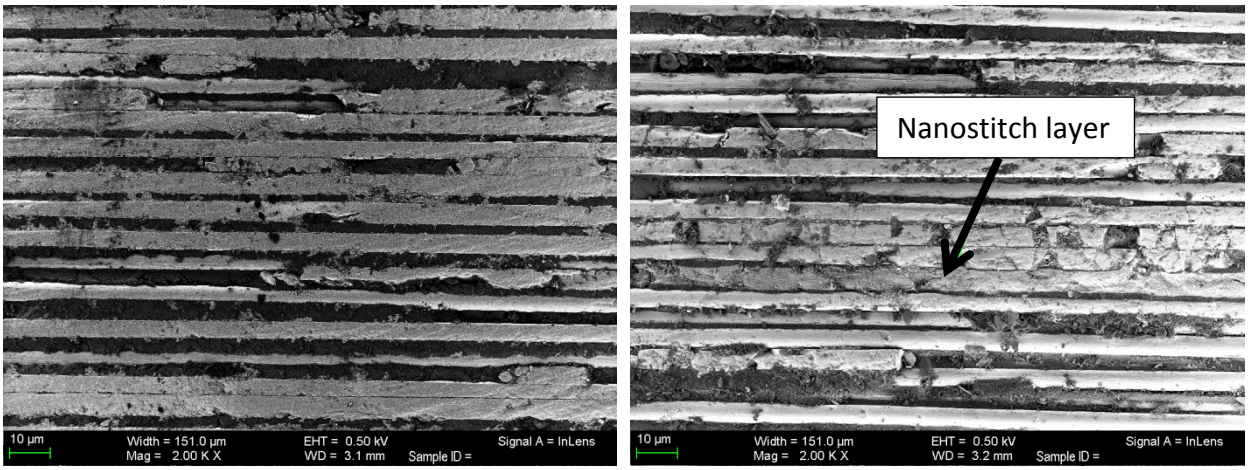

Figure 5-18: interfaces in unidirectional coupons (panel 2). Left, Reference - note that the 'interface' is within the image but cannot be distinguished. Right, nanostitched - note A-CNT layer in 'interface'.

The interfaces in the quasi-isotropic layup were easy to identify, as the reference as well as the nanostitch had distinct resin-rich regions between the plies. Figure 5-19 shows a representative image of both the reference and nanostitched samples. The interfaces in this preliminary (first sample set) study were highly variable in thickness and in conformation.

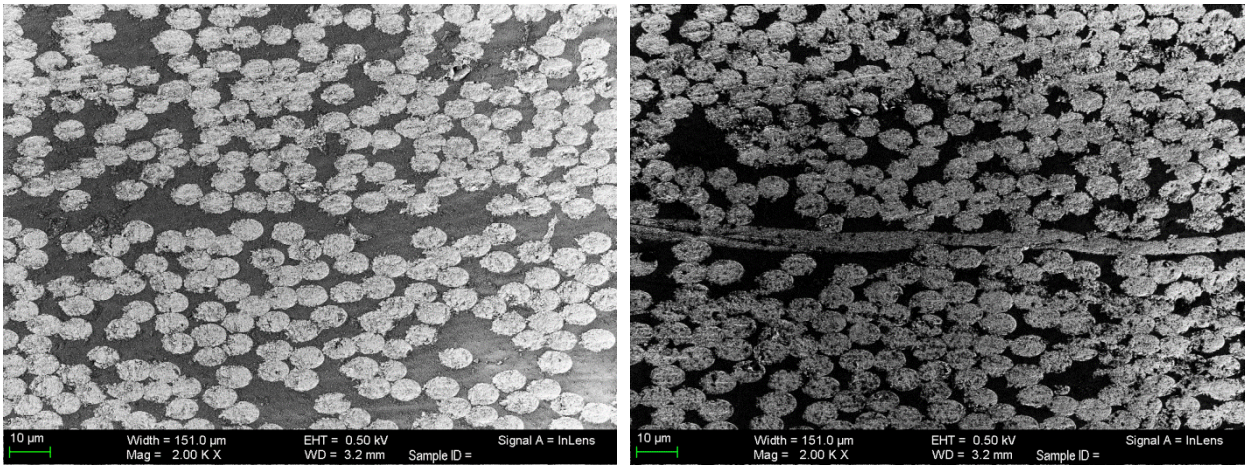

Figure 5-19: Average 8µm interface in reference, Panel 1, sample ref1 (left) and nanostitched, Panel 1, sample 4 (right).

Because the images only contained a 150µm–wide swath, these variations caused large standard deviations in the analysis of the interface characteristics. Figure 5-20 shows all interface images from a single sample, and exhibit the entire range of interface quality. Some images show nearly perfect interfaces (3 and 14), while some show large resin-rich regions (interfaces 2 and 12) and nanostitch defects such as a missing section (interface 4) and wavy regions (interface 10).

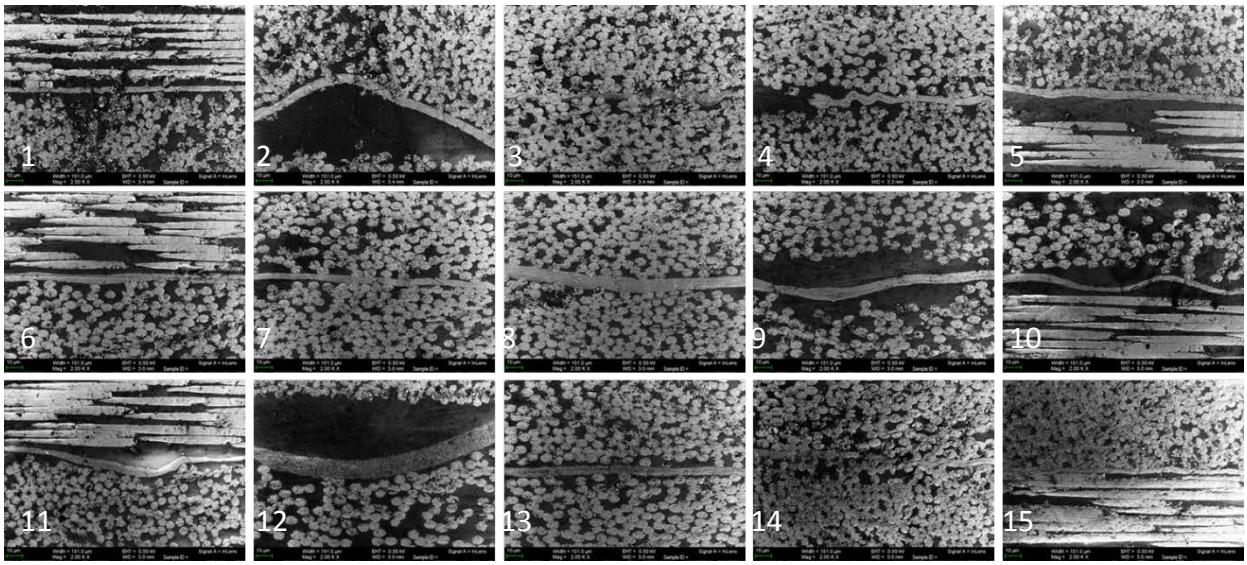

Figure 5-20: All interfaces in one sample (panel 1, sample 3), showing the range of interface quality.

For the first sample set quasi-isotropic samples, all calculated quantities had very large standard deviations due to the variability of the interfaces themselves. The interface thickness averaged 7µm for the reference sample, and while a trend of increasing thickness with forest height is noticed while looking at the graph, there is no statistically significant difference between the reference samples and any of the nanostitched samples due to the large variability. The height of the nanostitch was measured in the interface, and it was found that all forests 10-25 microns were compressed down to ~5µm in the interface. The 5µm starting forest height was compressed to a 3µm nanostitch layer. The percentage of the interface that was filled with CNTs was also measured, and averaged 60% across all samples with no statistical difference between them. See Figure 5-21 for visualization of percentage interface fills.

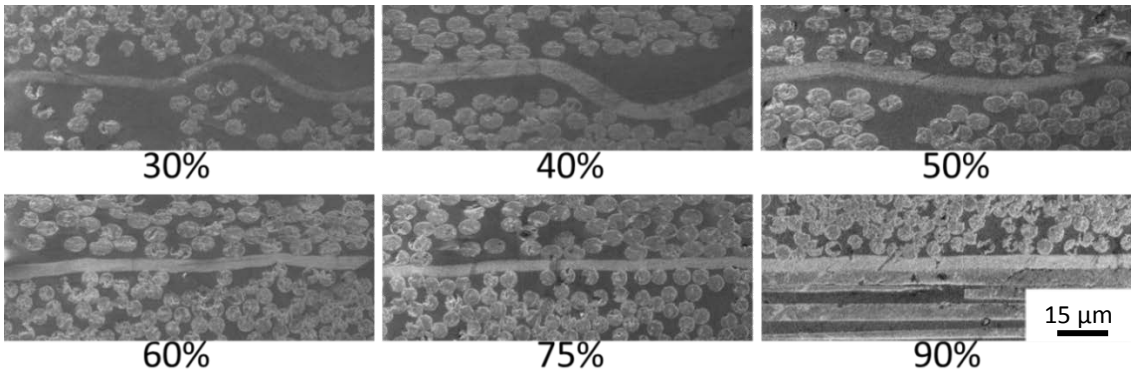

Figure 5-21: Visualization of different percentages of interface filled with nanostitch, Panel 5, sample F-nano.

In addition, the interface thickness was compared to the nanostitch height rather than the original forest height, however no trend could be discerned due to the compression of all of the forests down to at least 5µm. See Figure 5-22 for plotted data.

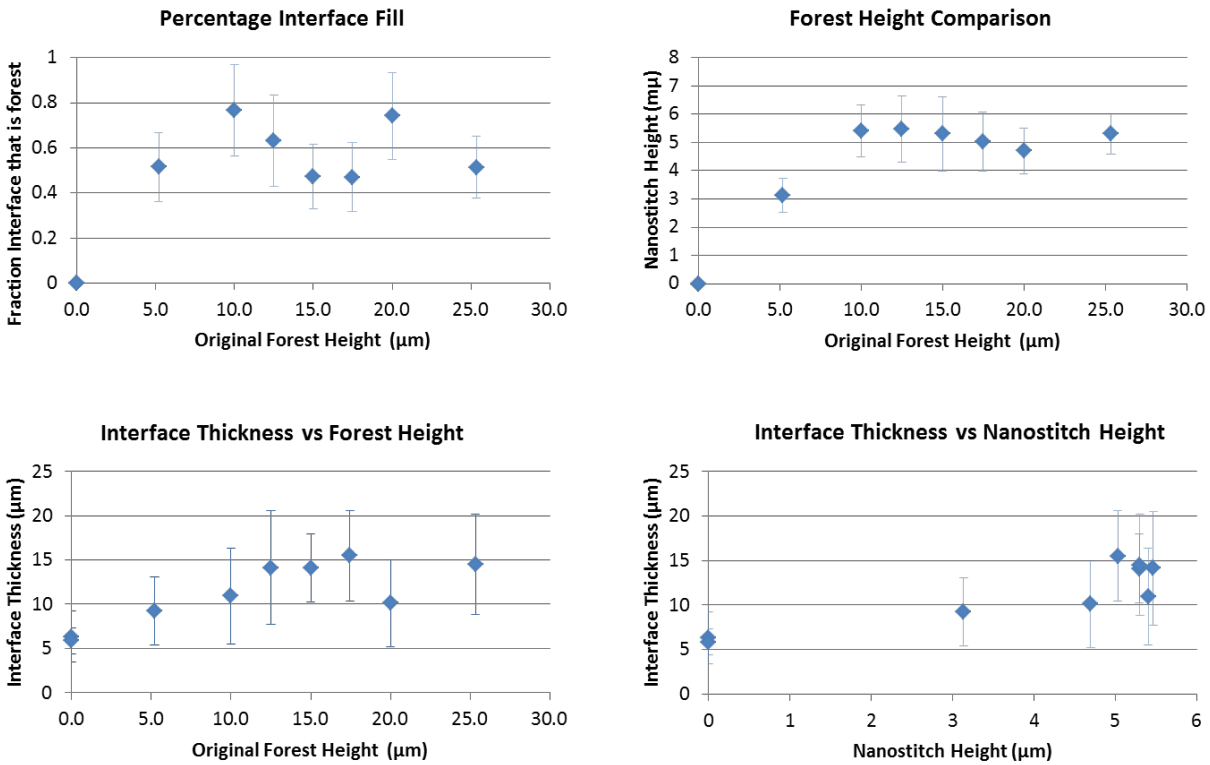

Figure 5-22: Interface statistics for first sample set (Method 1 transfer), plotted with 95% confidence (±2SE) on the means.

5.3.2 Second Sample Set

As mentioned in chapter 4, the second sample set consisted of two different layup techniques that resulted in distinct forest morphologies. Method 1 compresses the samples to a tight band in the interface, while Method 2 leaves the original forest height more conserved. See Figure 5-23 for an exemplary comparison of the two methods.

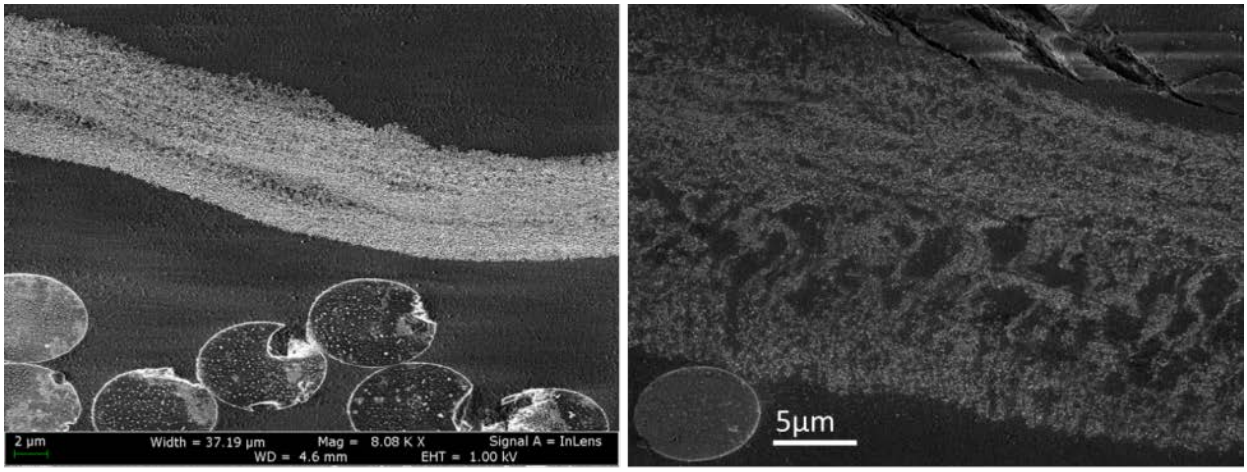

Figure 5-23: Nanostitch morphology difference between Method 1 (left) (panel 3, sample 1-2) and Method 2 (right) (sample 2-3). Left - 20µm forest compressed to 7µm in the interface. Right: 20µm forest measured at 19µm in interface.

The interface was again characterized for these sample sets. Wider SEM images (300µm vs. the previous 150µm) were taken to obtain more statistically significant data, however even with effectively double the data, some of the data points (especially for Method 2) were not statistically different from one another. However, the means do indicate possible trends, observed when the data is plotted. As can be seen from Figure 5-24, for the same forest heights (and overall), Method 1 – when compared to Method 2 - results in smaller interfaces, shorter nanostitch, but less interface filled with nanostitch. Method 2 results in three times taller nanostitch for the same original forest height, and an extra 27% interface filled for a 20µm tall forest.

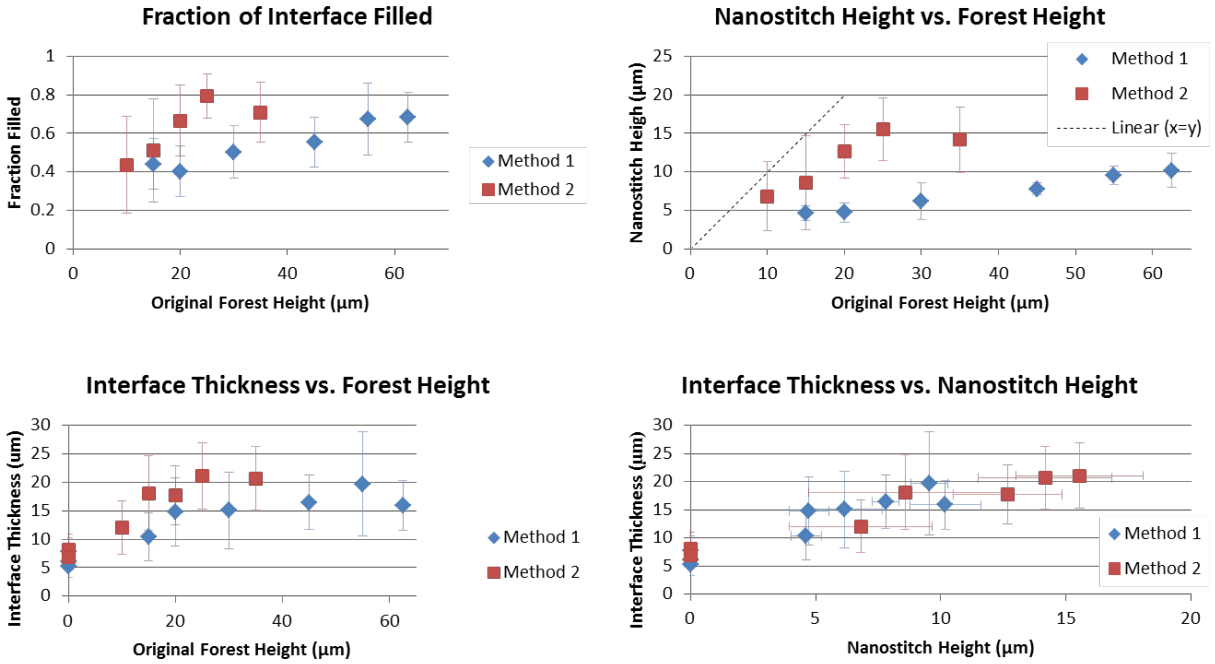

Figure 5-24: Interface statistics for Method 1 and Method 2 samples from sample set 2, plotted with 95% confidence on the means (±2SE).

To more easily see a difference between Method 1 and Method 2, the individual data points from the SEM images were plotted as interface thickness vs. original forest height. As shown in Figure 5-25, Method 2 can actually have a nanostitch height greater than the interface height, indicating that the CNT forest interdigitates with the carbon fibers on either side of the interface. This is not seen for any of the data points in Method 1; it is hypothesized that the nanostitch from this method is too densified to be able to interdigitate. In addition, it is noted that a final nanostitch height of 8-12 µm is most likely to fill the interface, which will result from an original forest height of 62.5 µm using Method 1 or 15-20 µm using Method 2.

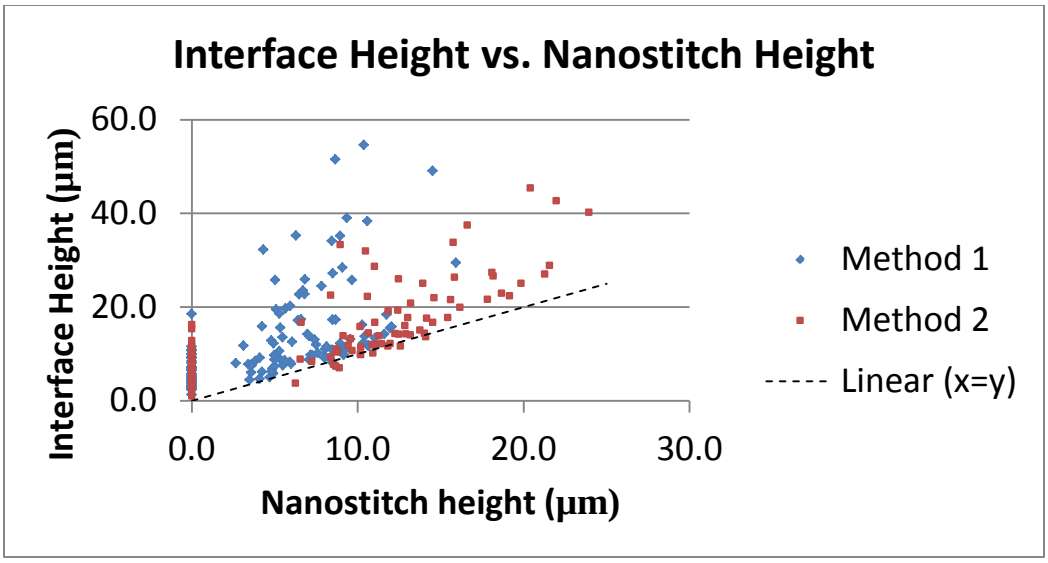

Figure 5-25: Individual data point plot for every SEM image analyzed. Interface height is compared to nanostitch height. Note that Method 2 has nanostitch heights greater than the interface height (points below the x=y line), indicating that the nanostitch is interdigitating with the carbon fibers in those instances.

The overall laminate thickness was seen to increase with increasing forest height for both Method 1 and Method 2, with differing trends as shown in Figure 5-14. To determine whether this is a result of the added interface thickness, the overall laminate thickness was plotted against the interface thickness for all samples in Figure 5-26. It was confirmed that the laminate thickness seems approximately linearly dependent on the interface thickness (regardless of transfer method) if one ignores statistical significance, however only 0.23 µm are added to the laminate thickness per µm of additional interface thickness. This indicates that much of the added thickness of the interface is resin migrating out of the ply and into the interface.

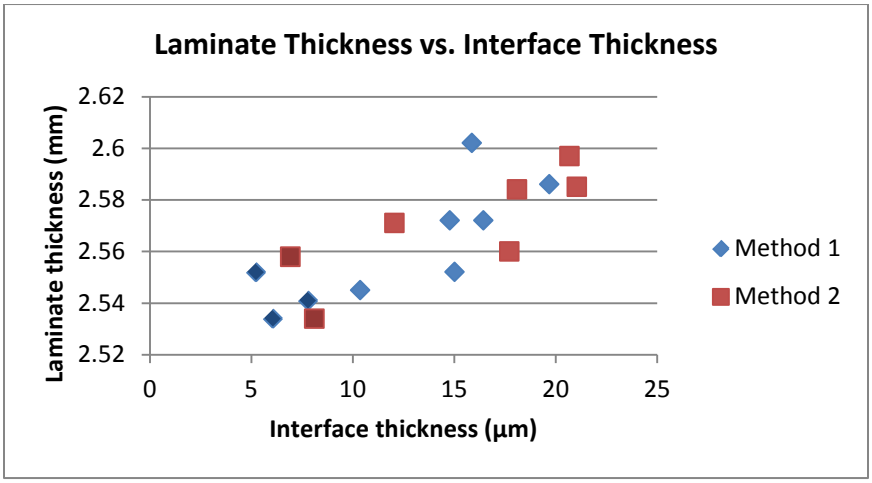

Figure 5-26: Laminate thickness vs. interface thickness for all samples in Set 2. Darker data points at 5-8 microns are the reference samples. Standard error not plotted due to the large values making the graph difficult to read.

It was noticed that this resin migration in the nanostitch samples occurred in localized regions, causing large variation in the data gathered from the SEM images. (This is the reason for the high standard deviations in the nanostitched sample interface data). These *resin pockets* appeared to be coming from areas in the ply that had a locally higher resin content as seen in the baseline specimens (see Figure 5-27). The resin-rich regions are thought to result from tow spreading inconsistencies in the prepreg manufacture. The resin-rich regions only agglomerated into interfacial resin pockets in the nanostitched samples, not the reference. It is hypothesized that the CNTs wick the epoxy from these resin-rich regions into the interface. More research will need to be conducted to determine the mechanism by which this happens; see section 5.3.4 for further discussion.

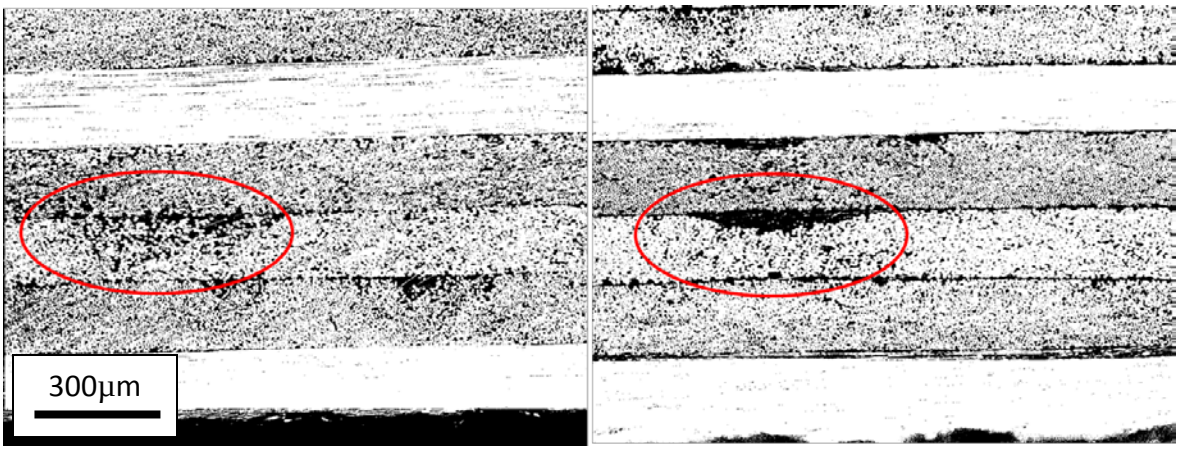

Figure 5-27: Tow-spreading inconsistencies in IM7/8552 prepreg leads to resin rich regions in plies (left). Resin agglomeration at the interfaces in nanostitched samples (right) appear to coincide with these resin-rich tow-tow junctions in the plies. Images from Panel 5, fatigue samples.

To quantify the size and number of resin pockets in the samples, it was determined that the narrow swaths from the SEM images could not be used to get an accurate picture of these resin pockets. Instead, images from an optical microscope that showed one-half of a coupon from Sample set 2 were analyzed in Image J. The images were contrast enhanced, despeckled, and converted to binary. The program was then asked to find all black (resin) areas larger than 20 pixels (chosen just large enough to automatically exclude most intra-ply resin areas). The number and size of the resin pockets from each image was recorded and the results shown in Figure 5-28. Interestingly, there was a difference between Method 1 and Method 2, as well as the noted difference between nanostitched samples and reference. For Method 1, regardless of forest height, there were an average of 116 identified resin pockets per sample. For Method 2, there was a lower average of 97 resin pockets, almost 20% fewer. The reference samples, in contrast, had only 63 resin pockets per sample, roughly half of what is found in Method 1.

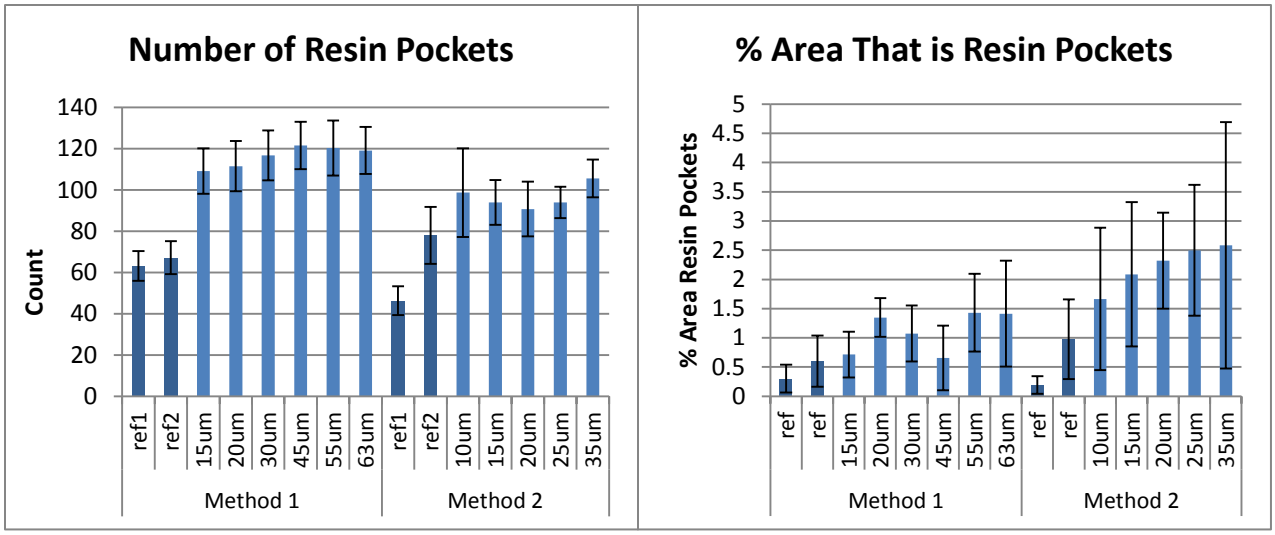

Figure 5-28: Resin pocket analysis. 95% confidence intervals on the mean (±2SE) are shown. Left: Number of resin pockets per coupon. Right: % area of sample that is included in resin pockets.

The area of the resin pockets was also quantified as a percentage of the total image size, however it is doubtful that the method used is accurate at determining resin pocket size. If a thick interface (as most often seen in Method 2) was connected to the resin pocket, this area was also included in the calculated size of the resin pocket. The area percentage correlates directly to the interface thickness calculated from the SEM images, and not as expected to the overall number of resin pockets. Visually, the resin pockets appeared much smaller in the reference samples and about the same size in Method 1 vs. Method 2.

5.3.3 Third Sample Set - Fatigue Samples

From the results of the prior sample set, it was noted that more SEM images were needed to obtain a statistically relevant data set. Three coupons were imaged instead of one, with an image width of 300µm; a total of 90 images analyzed. These images were analyzed in the same manner as the other samples, and resulted in a statistically significant difference between the interface thickness of the nanostitch and reference samples (z test shows 98% probability of a difference of 4µm). The nanostitch had an average interface thickness of 13.40µm, while the reference was only 7.47µm. The nanostitch height in these samples was 5.26µm, the same as reported for the Method 1 samples with 10-15 µm original heights of the forest (these forests were originally 12.5µm height average). It should be noted that while the interface thickness increased by 6 µm for the nanostitched samples, the overall laminate thickness did not increase (Table 5-1), indicating resin migration into the interface.

Table 5-2: Interface and nanostitch heights for fatigue samples

	Interface Thickness (µm)		Nanostitch Height (µm)		Percentage Fill	
	Average	St Dev	Average	St Dev	Average	St Dev
Nanostitched	13.40	5.98	5.26	1.82	47	19
Reference	7.47	5.24				

The resin pocket analysis was also conducted on the samples manufactured for fatigue testing. Again, images were taken with an optical microscope to obtain a wider image for analysis of these resin pockets. For this set, two 1.25mm-wide images were taken from each sample (to obtain an image for every interface). The images were converted to binary, despeckeled and black regions with areas larger than 2000 pixels (~2000µm^2) were captured as resin pockets. (The change in pixel area from the previous set is due to the change in image magnification; the previous set were imaged at 10x lower magnification.)

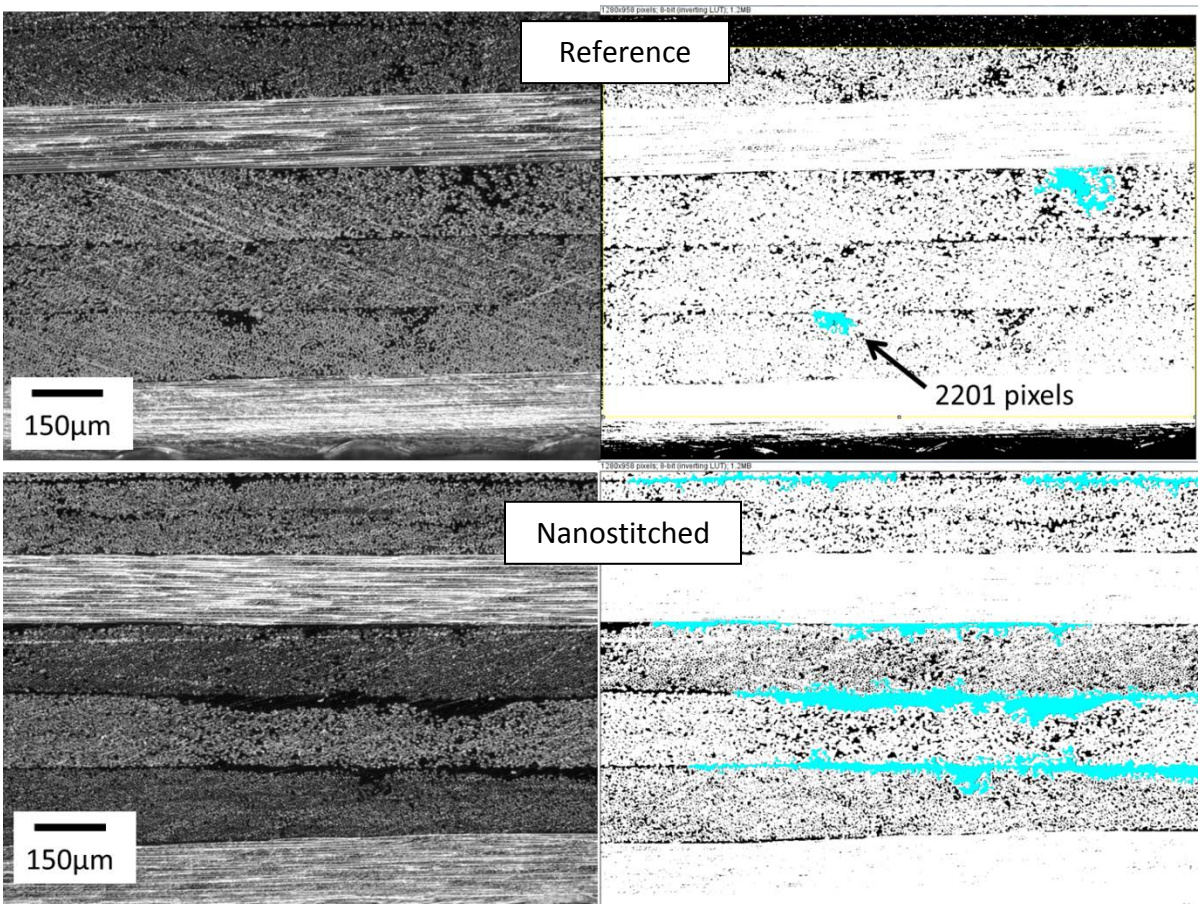

Figure 5-29: Resin pocket automated analysis using optical microscopy in fatigue samples (Method 1, 12.5µm nanostitches). Images from microscope (left) converted to binary, depseckled and resin pockets >2000 pixels counted (right). Top is a reference sample, bottom is a nanostitched sample: the nanostitched sample shows the error in size caused by resin in the interface being counted as part of the resin pockets.

The method again worked well for the reference, but overestimates the size of resin-rich regions in the nanostitch samples. Note that some very thin interface regions are connected to resin pockets, which skews the results. On average, the nanostitch coupons had 24 resin pockets per 1.25mm-wide swath, while the reference only had 9. Note that these numbers are higher than generated with the previous method (most likely due to the increased resolution), however the ratio between Method 1 samples and the reference is similar.

Table 5-3: Resin pocket analysis for fatigue samples

	Count		% Area	
	Average	St Dev	Average	St Dev
Nanostitch	24.4	8.5	12.1	5.5
Reference	9.3	5.5	8.4	14.1

5.3.4 Notes on Resin Migration to the Interface

Some interesting phenomena were observed with regard to the resin migration through the forest and into the interface. However, first and foremost, it should be acknowledged that this resin pocket formation is specific to the IM7/8552 CFRP system, and is not observed in the other system (AS4/8552) studied in previous work [69]. It is suspected to occur due to resin-rich regions present in the original prepreg due to tow-spreading inconsistencies during its manufacture. Second, it should be noted that while the resin pockets appear more plentiful in certain interfaces (notably the 90/+45 and +45/-45 interfaces), this is due to the 2D nature of the images: a resin pocket adjacent to a 0 degree ply would only appear as a thicker interface, for instance (the resin pocket is being cross-sectioned along its length rather than through its thickness).

It is noted that the resin fully infiltrates the forest region, regardless of the amount of compression (Method 1 vs. Method 2). This is thought to occur due to capillary wicking, and should occur regardless of the shape of the forest.

The phenomenon of resin pockets forming seems to be directionally dependent, and occurs on the *inner* interface of a particular ply, i.e., at an interface, the resin pockets come from the *exterior* ply. This makes it seem as if the pockets are pointing outward from the centerline (Figure 5-30). (Also note that at the centerline, the -45/-45 interface is wavy but does not contain as many of these resin pockets; this is most likely due to the ease of carbon fiber migration when unidirectional plies are placed adjacent to each other.) Note that the layup of the laminate is done with the same procedure for every ply, so the top/bottom of the ply is the same throughout the laminate and the resin pockets would be expected to always occur on the same side of the prepreg ply if the phenomenon was dependent on the orientation of the original ply.

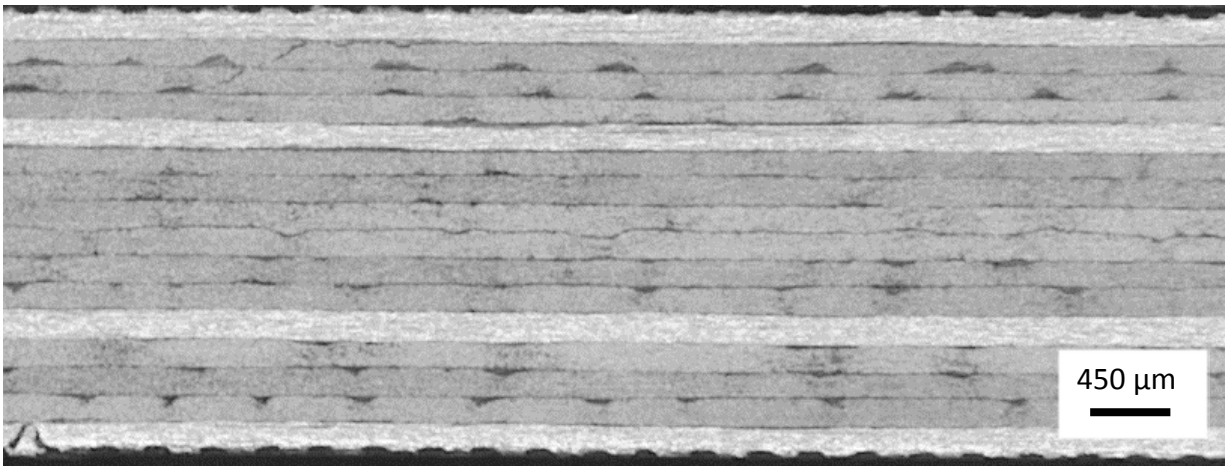

Figure 5-30: Directionally dependent resin pocket formation. Resin pockets form on the *inner* interface of a ply, looking like they point outward.

Second, it is noticed that the resin infiltrates *through* the forest to generate these pockets. In Figure 5-31 (left), it can be seen that the original location of the nanostitch was against the upper ply's carbon fibers (note the indentations in the top of the forest), but was transported away as the resin migrated through the forest. It can also be seen that the A-CNTs are always between the resin pocket and the resin's original location in the prepreg in Figure 5-31 (right). This means the nanotube forest is acting as a membrane, possibly causing the resin migration due to a chemical potential gradient across the forest. It is known that the epoxy used, 8552, is toughened, however the exact chemical composition is unknown. Future work should include studying the chemistry of the resin to determine if there is a difference in resin component concentration across the nanostitch.

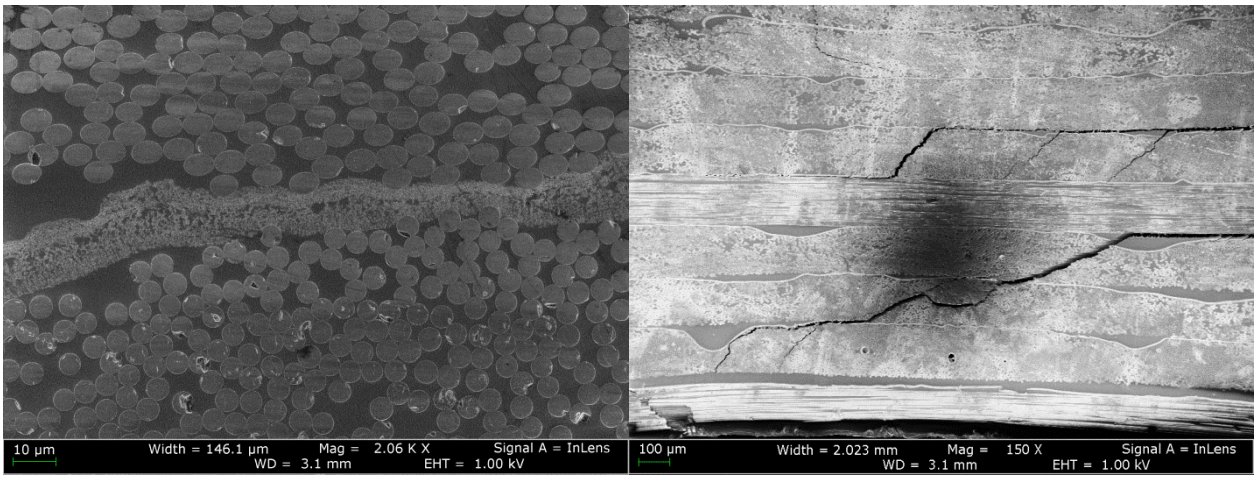

Figure 5-31: Resin infiltration *through* the CNT forests. The resin-rich regions appear on the opposite side of the nanotube forest to the region from where the resin originated. Left: Sample 2-3, The forest was originally compressed onto the top ply, then migrated away. Right: Sample 1-2, Nanostitch is between all resin pockets and the the original location of the resin (Note, the coupon was previously tested and cracks can be seen).

Due to an experiment that cured AS4/8552 in an oven rather than an autoclave, it was noticed that the nanostitched interfaces did not contain voids, while all others did. It is suspected that the resin-wicking property of the nanostitch pulls epoxy to the interface, displacing voids. Regions where forest defects occurred exhibited voids, just like the rest of the sample's interfaces. This suggests that nanostitch may have applications in out-of-autoclave work, including original curing of the material, joining composite parts, repair or patching, or any application where resin infiltration is critical to performance because the probability of voids will likely be reduced.

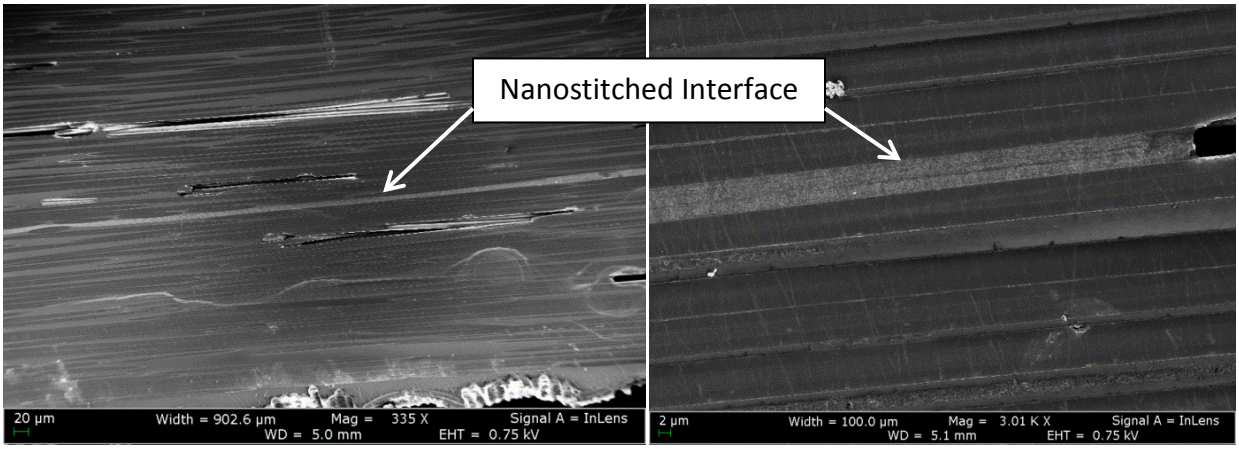

Figure 5-32: Nanostitch shown to eliminate voids at interfaces.

6 Short-Beam Strength (SBS) Test Results

The parameter space for carbon nanotube (CNT) morphology is very large. The approach that was followed in this thesis was to determine a range of interest from the two chosen parameters (A-CNT height and layup technique) using short-beam strength testing (SBS). The choice of SBS (ASTM D2344 [89]) as a screening test is twofold; first, it probes interlaminar properties, and second, the coupon size is very small, leading to an efficient use of CNT material. This testing explored forest height in the range of 5µm to 65µm and used both layup techniques. It was expected that the results from these tests would lead to a range of interest for the forest heights that could then be used in subsequent DOE testing with other parameters (such as A-CNT density, waviness, patterning and compression) and mechanical tests.

6.1 SBS Testing

The SBS test is a three-point bend test, using a span of 4.0x the coupon thickness. This dimension constraint induces large shear stress in the midplane of the beam. In laminated samples, shear failure is frequently in the interlaminar region, and as such this is generally considered an interlaminar shear strength (ILSS) test in industry. However, as noted in the ASTM standard D2344 [89], the strength reported by this test should only be considered a true ILSS value if the failure was verified to be in the interlaminar region. While all results are reported in this section as ILSS values, it will be shown that the majority of nanostitched samples fail in complicated ways that do not exclusively involve the central interface. Therefore these values should be considered as a lower limit to the ILSS that has been achieved for nanostitched laminates, and considered as SBS rather than a true ILSS.

6.1.1 Static Testing

A Zwick Mechanical Tester (model Z050) at the Institute of Soldier Nanotechnologies was used for all static SBS testing. ASTM D2344 [89] was followed precisely. A three point bend fixture was used with 3mm diameter cylindrical supports (origin unknown) and a 6mm diameter cylindrical loading nose from Wyoming Test Fixtures (Figure 6-1). The coupons tested were on average 2.55mm thick, so the three-point bend support span was set to 10.2mm (4.0x the coupon thickness). Parallelism was confirmed between the supports and loading nose, horizontally by affixing the loading nose to the upper support while it was sandwiched between the bottom support, and vertically with a glass slide spacer. The test was done in displacement control with speed set to 1mm/min. As noted previously (section 5.2), the width and length of the coupon were 2.0x and 6x the coupon thickness respectively. Each coupon was centered on the supports, and loaded to failure.

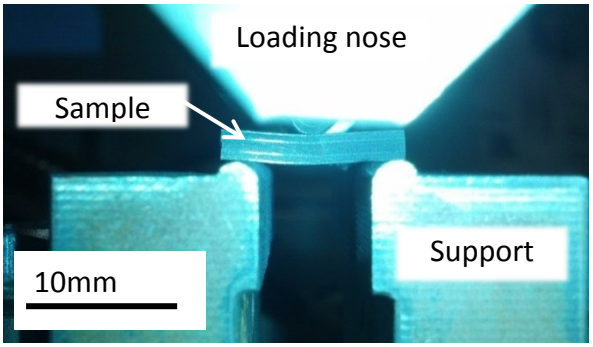

Figure 6-1: SBS test fixture with failed coupon.

The coupons failed randomly left/right of center for both unidirectional and quasi-isotropic coupons, indicating a well-aligned test fixture. Generally, no noise was heard until a loud snap as the sample failed.

The unidirectional samples were tested first. Ten coupons were tested for both the reference and nanostitched samples. It was not expected that the nanostitched sample would improve the strength over the baseline, because unidirectional plies merge during cure, leaving the interfaces indistinguishable from the plies themselves. In the nanostitch-reinforced sample, the interfaces existed only as the nanostitch layer. It was expected that the cracks would propagate outside of these reinforced regions, in the areas that were the same as the reference. As expected, the strength values were statistically similar. The reference coupons failed at an average of 125.9MPa, with a standard deviation of 2.3, while the nanostitched coupons failed at 128.4±5.4MPa (see Figure 6-2). Note that the samples had an ILSS only 7.3% lower than the unidirectional ILSS reported from the manufacturer (137MPa). Other literature reports values of ~100MPa for the same material [91] [92] in the unidirectional configuration.

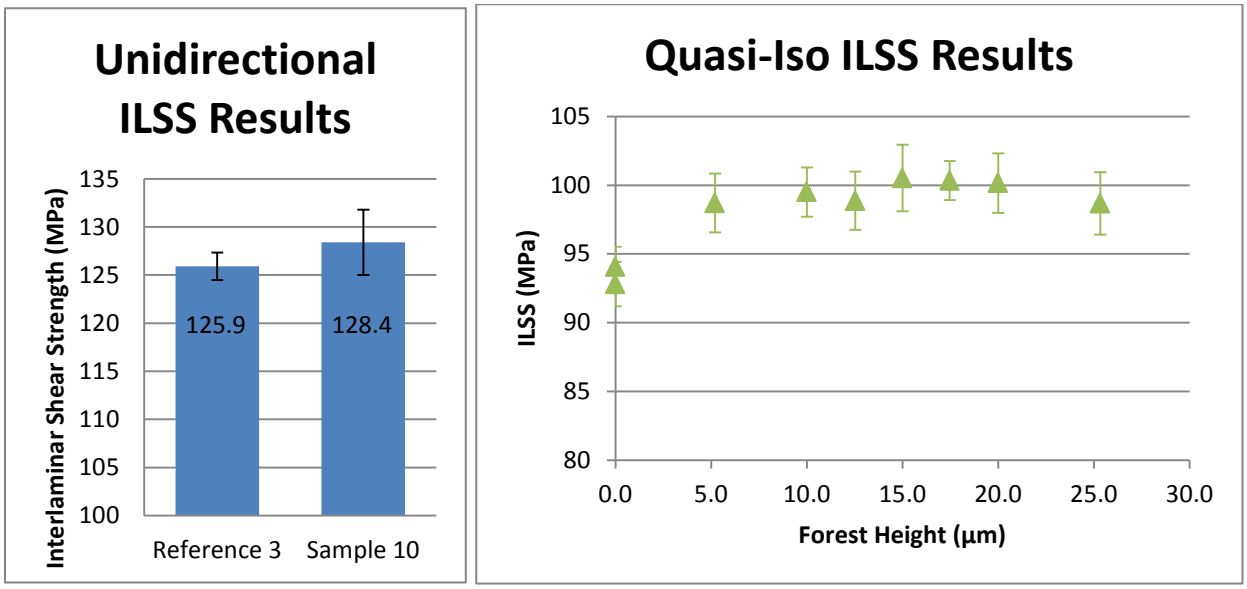

Figure 6-2: Unidirectional and quasi-isotropic first sample set Method 1 ILSS results, plotted with 95% confidence (±2SE) on the mean.

The first sample set, method 1 quasi-isotropic test panel's results are shown in Figure 6-2. The reference samples failed at 93.5±2.8MPa. All nanostitched samples showed an improvement in ILSS over the reference sample, averaging a 6.5% improvement. There was no statistically significant difference between the forest heights. It is suspected that this is due to the structure of the forests in the interface; regardless of initial height, the forests were compressed to ~5µm in the interface (section 5.3). This compressed morphology was the same throughout the samples, providing a rationale for why all the heights failed at the same ILSS

value. In addition, cracks frequently propagated outside of the interface regions, suggesting that the nanostitch sufficiently reinforces the interface regardless of height (see discussion in section 6.2).

The second sample set of ILSS testing again showed a surprising lack of dependence on forest height. In addition, the difference between Method 1 and Method 2 was negligible; i.e. the major difference in structure noted in section 5.3 did not have an effect on the strength improvement. With the exception of the sample with noted bad center-ply transfer, all nanostitched samples were statistically similar and showed an average 8.75±0.5% improvement over the reference samples. Again, the invariance is suspected to result from the nanostitched samples having failure modes outside of the interface.

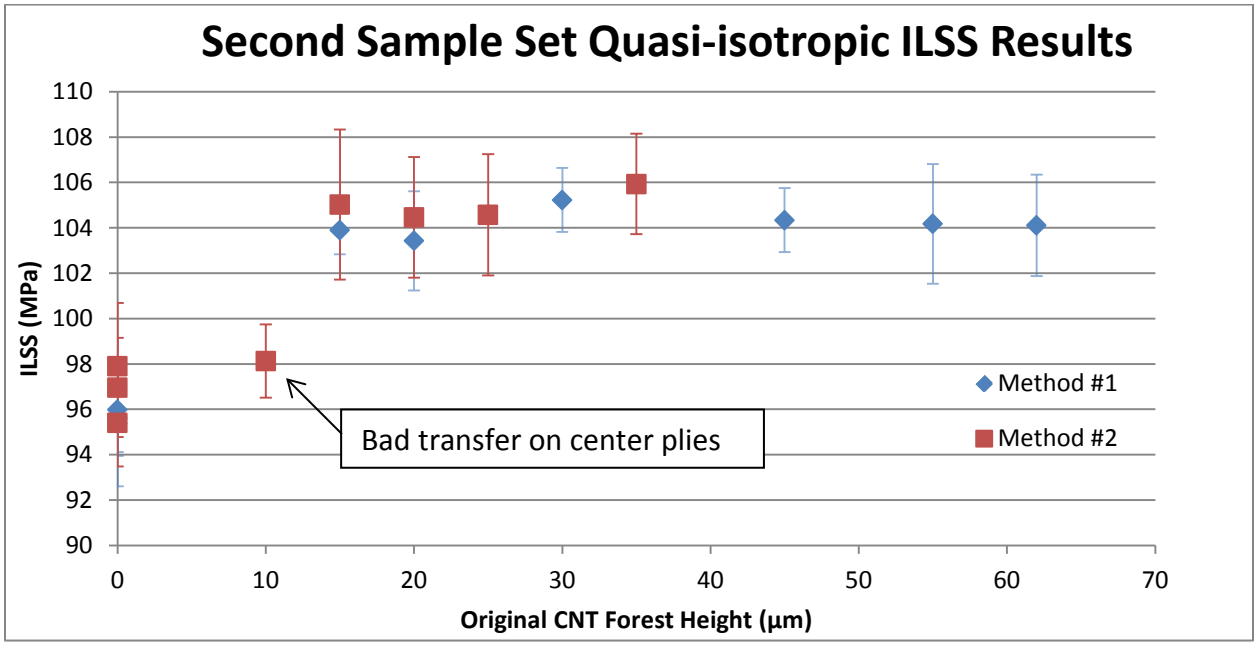

Figure 6-3: Second Round ILSS results comparing Method 1 and Method 2 transfer. All nanostitched samples averaged an 8.75% improvement over reference, regardless of forest height or transfer method.

The results from the quasi-isotropic second sample set were statistically similar to the first sample set, however a direct comparison between the first sample set and second sample set was not made due to different average values of the reference samples (93.5MPa vs. 96.2MPa) To make a comparison, results from both sets of tests were normalized to the average reference ILSS and plotted in Figure 6-4. It should be noted however that because of the different layups, the plot should be viewed as instructive only.

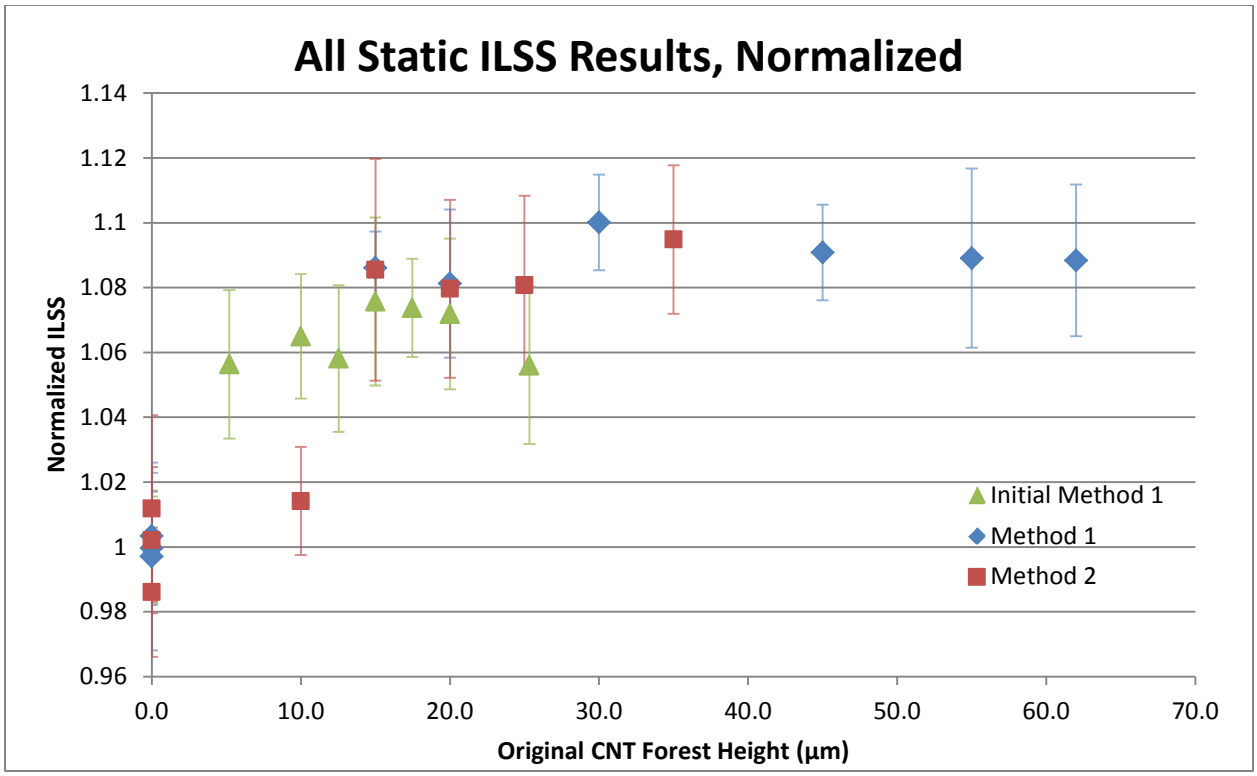

Figure 6-4: All Static Quasi-Isotropic ILSS Results, normalized and plotted with 95% confidence (±2SE) on means.

6.1.2 SBS Fatigue

To determine fatigue properties of the nanostitched material, the SBS test was used in fatigue (note, ASTM D2344 is a static test and there is no SBS fatigue standard). The Method 1 layup technique was used with 12.5µm tall A-CNTs. An Instron (1132 load frame) was used for fatigue testing. Because the Instron's load cell and grips were too large for the small samples, a smaller load cell (5kN capacity, Instron 2518-603) was installed on the lower grip. The load cell was calibrated using the auto-calibration function in the Instron's software. A fixture was designed and machined out of aluminum for the three-point bend test. Because the Instron's lower grip could rotate with respect to the upper grip (it is mounted on a hydraulic cylinder), the fixture's loading nose was a 6mm hardened steel rod that floated on the sample between support columns extending from the base; the upper grip held a simple aluminum cylinder to apply pressure to the rod (see Figure 6-6). The lower fixture seated two 3mm diameter hardened steel rods spaced 10.0mm apart. Note that the previous testing had a span of 10.2mm, however the fatigue fixture was designed with fixed-position supports, and 10mm was chosen due to the expected 2.496mm nominal thickness of the coupons. This

Figure 6-5: Instron used for fatigue testing.

difference in span is not expected to influence the results, however it should be noted that to follow the static ASTM D2344 standard, the span must be four times the coupon thickness with a tolerance of 0.3mm. The actual coupon thickness averaged 2.599, meaning that the span should have been a minimum of 10.1mm. The lower supports were seated such that there was a 2.7mm gap between the floor of the fixture and the coupon, ensuring that the sample could not touch the floor without exceeding the limits of the test (deforming more than one sample thickness [89]).

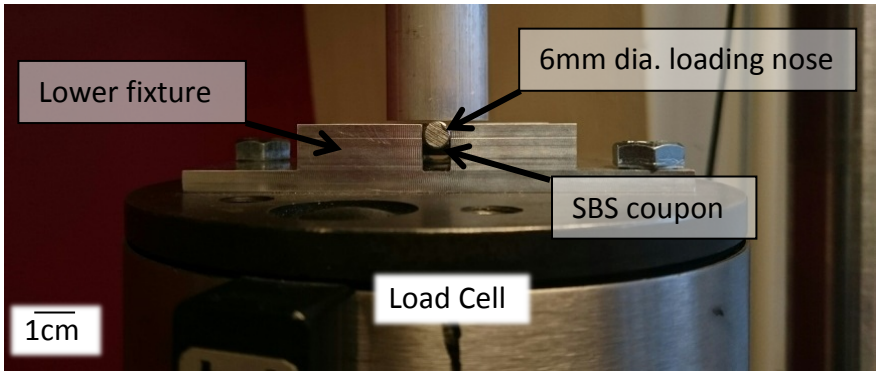

Figure 6-6: Fixture for SBS fatigue testing mounted on the 5kN load cell.

A static test was performed on the new instrument and fixture to ensure that the setup generated failures at the same loads. Three reference coupons and three nanostitched coupons were loaded under displacement control until failure. The reference mean ILSS was 96.4MPa and the nanostitch was 103MPa, a 6.8% improvement. Both samples failed in the same range as that from previous testing.

Fatigue testing was performed in load control at 10Hz, with an R ratio of 0.1. 10Hz was the maximum rate recommended for polymer samples (hysteretic heating and thermal softening can result from frequencies higher than this). Coupons were cycled to failure at peak loads of 100%, 90%, 80%, 70% and 60% of the reference static ILSS of 96.4MPa. The load was programmed to increase to the set value over the first ten cycles (1s) to prevent overshoot, however the recorded data indicates that the load overshot by a maximum of 5% on cycles 3-5 before decreasing to the set value by cycle 10. Failure was determined as a peak displacement increase of 0.1mm from the peak displacement at cycle 10. Unfortunately, when testing in load control, when the compliance of the sample suddenly decreases as it breaks, the load will cause excessive displacement as it completes its cycle. This caused most of the samples to be crushed at the end of the test.

The number of cycles to failure was averaged at each load level for both sets of specimens. On average over all load levels except the reference 100% load level (reference cycles to failure = 1), the nanostitch coupons took 3.2 times longer to fail (3x lifespan) than the

reference samples. The data was plotted in the standard S-N curve format, shown in Figure 6-7. The maximum improvement was for samples at the 95MPa (100%) load level (35x lifespan) and the minimum improvement was 2.2x lifespan for samples tested at 85MPa.

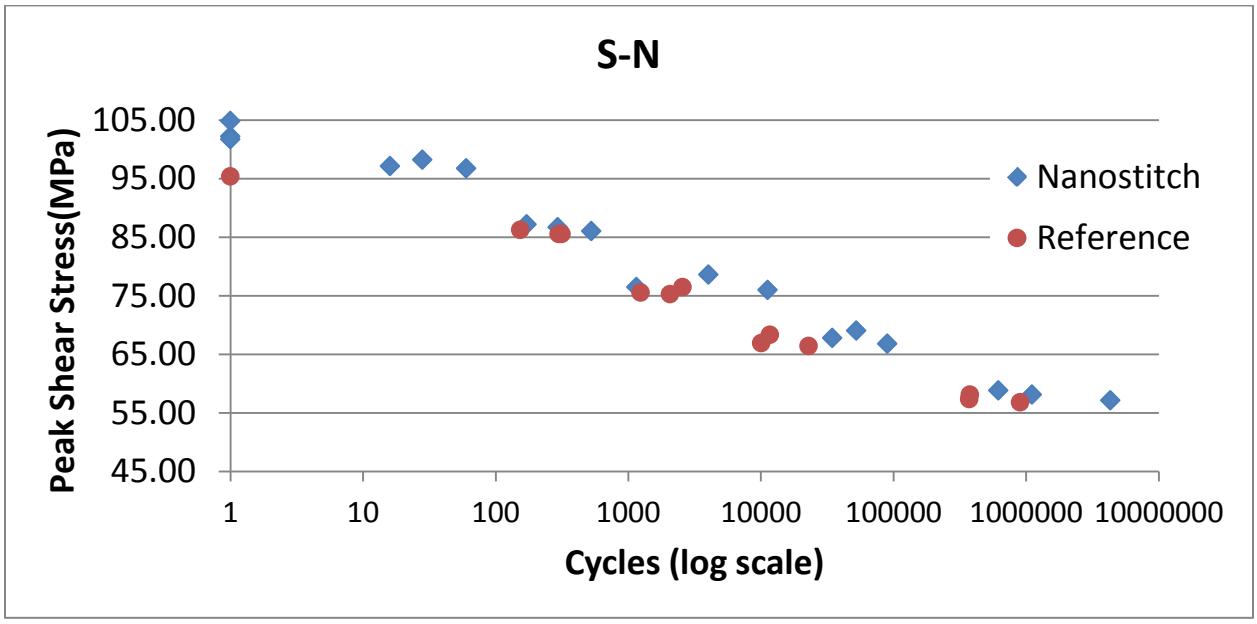

Figure 6-7: Cycles to failure in fatigue testing.

If this data is replotted as a percentage of the static strength of each type of coupon (nanostitch and reference), the curves can be seen to collapse onto one another (Figure 6-8). This suggests that the observed increase in lifespan of the nanostitch coupons is due to the static strength increase.

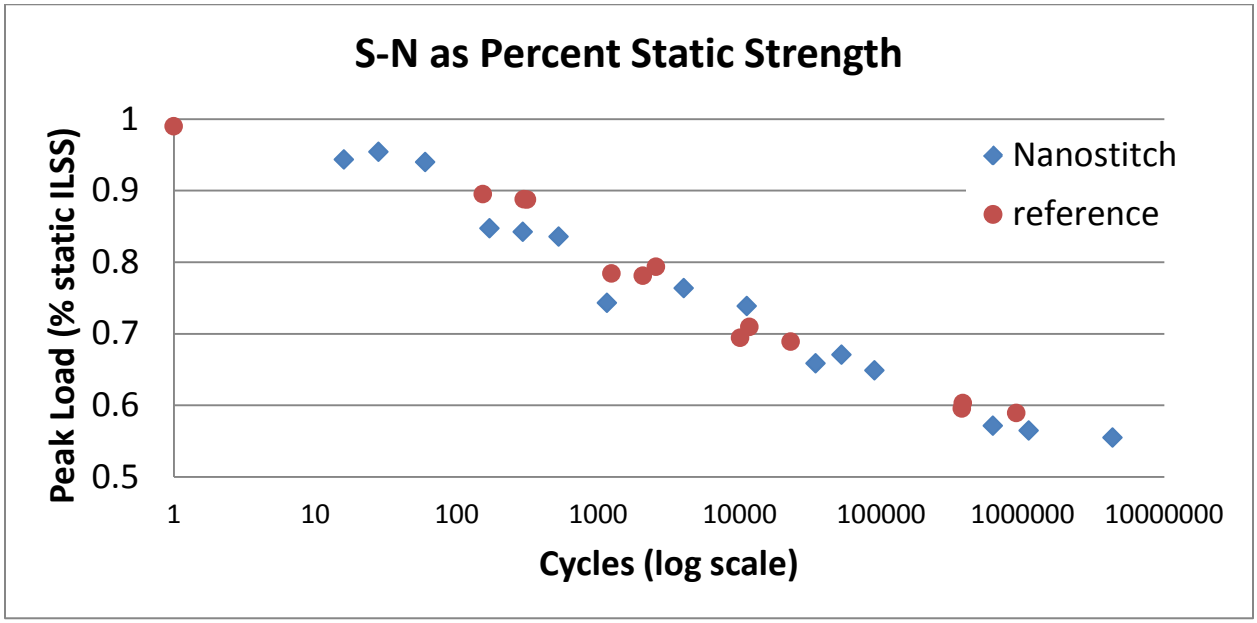

Figure 6-8: S-N as a function of percentage of static strength.

To determine the mechanism of fatigue life enhancement, the compliance for these coupons was plotted as well. The stiffness change, referenced to the stiffness at the 20th cycle, is plotted in Figure 6-9 for the set of nanostitch and reference coupons tested at the 70% peak load level. For all samples, there is a stiffness loss at ~100 cycles. This is due to non-propagating crack formation under the loading nose. May et al. [91] shows modeling results that indicate this crack formation should occur in every sample tested in SBS, due to the compressive stress present just under the loading nose. The crack does not propagate due to the localization of this stress. This crack formation was verified by optical images taken of the samples after failure. The timing of the crack formation in fatigue tests was verified by microCT analysis of two samples fatigued at 70% peak load for 1000 cycles (leaving them unbroken) as discussed later in section 6.2.

The stiffness decreases in the same manner for the nanostitch and reference samples, however the reference samples fail earlier than the nanostitch. This similarity in curve profiles suggests that the nanostitch does not prevent the initiation of microcracks that lead to a stiffness decrease; instead they most likely delay or arrest crack propagation. In Figure 6-9 , one can see the stiffness slope change at ~2000 cycles for the reference coupons, while this slope change (which indicates crack growth) does not occur until ~10,000 cycles in the nanostitch coupons.

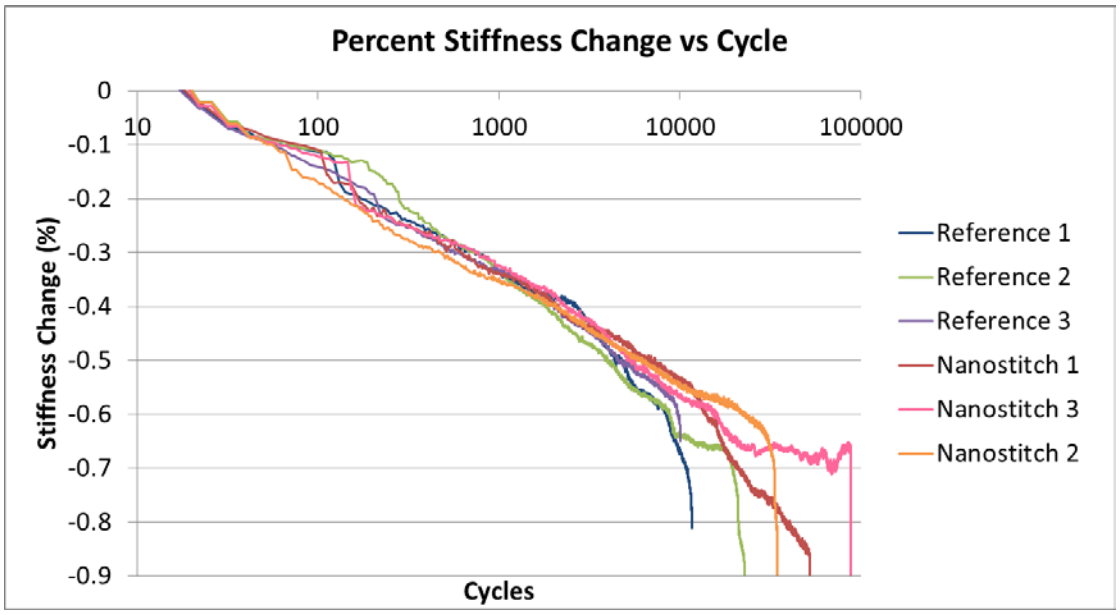

Figure 6-9: Stiffness change for 70% load case. Note, the first major stiffness change (~100 cycles) occurs due to the formation of a non-propagating crack under the loading nose.

6.2 Fractography

Damage generated in the static SBS testing that was visible on the coupon sides was imaged and analyzed for location, length and number of cracks. The highly polished samples

were also SEM imaged and analyzed for nanotube pullout behavior and crack propagation behavior. In fatigue testing, most of the samples were damaged by overshoot at the end of the test, and could not be analyzed in this way. Instead, the crack surfaces (exposed by breaking apart the sample at a major crack) near the center were SEM imaged for evidence of crack growth in fatigue cycling. In addition, microCT was employed for viewing internal damage in partially fatigued coupons.

6.2.1 Crack Number/Location Analysis from Optical Images of Static SBS Coupons

Five coupons from each sample in the Second Sample Set (static, quasi-isotropic samples utilizing both layup methods) were imaged with an optical microscope to visualize and understand the damage formation in the SBS test. The images were input into ImageJ and the cracks traced with the software tool NeuronJ. This program calculates the average length, total length, and number of traces in the image.

When comparing the reference and nanostitch in Method 1 (Figure 6-10), it is immediately apparent that the crack location is different. In the reference coupons, the majority fail from a single crack along one or both of the +45/-45 interface adjacent to the centerline. This is considered valid for determining an ILSS from the SBS test (see Figure 7 in ASTM D2344), and the numbers reported in 6.1.1 for the reference samples are ILSS. In contrast, the nanostitch coupons fail predominantly at the bottom 0/90 interface closest to the center, usually with a small number of secondary cracks (smaller cracks) elsewhere. Because of the propensity for samples to fail at the 0/90 interface, ANSYS modeling (section 6.3) was done to confirm that this is also a high-stress area in a $[0/90/+45/-45]_{2S}$ layup subjected to SBS testing.

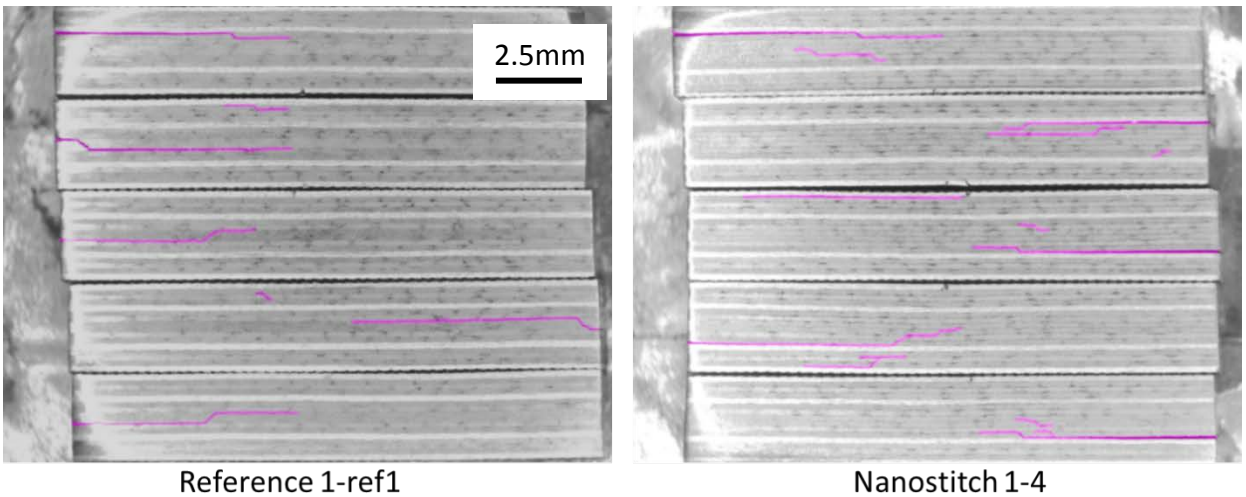

Figure 6-10: Five-coupon images of a reference and Method 1 nanostitched sample, showing crack location differences between reference and nanostitch. The reference coupons mostly fail at the +45/-45 interfaces near the centerline, while the Method 1 nanostitch coupons fail predominantly on the 0/90 interface closest to the centerline.

When looking at Method 2 samples (Figure 6-11), one notices a drastic difference between the reference and nanostitch. Again, the reference samples fail as expected; predominantly at a +45/-45 interface next to the centerline. The Method 2 samples, however, fail in a manner different from both the reference and Method 1 samples. The Method 2 samples fail with multiple cracks through both interlaminar and intralaminar regions; the damage is so widespread and diffuse that it is oftentimes impossible to determine a major crack. These coupons show cracks that have multiple ply jumps and many short, separate cracks throughout the thickness of the sample.

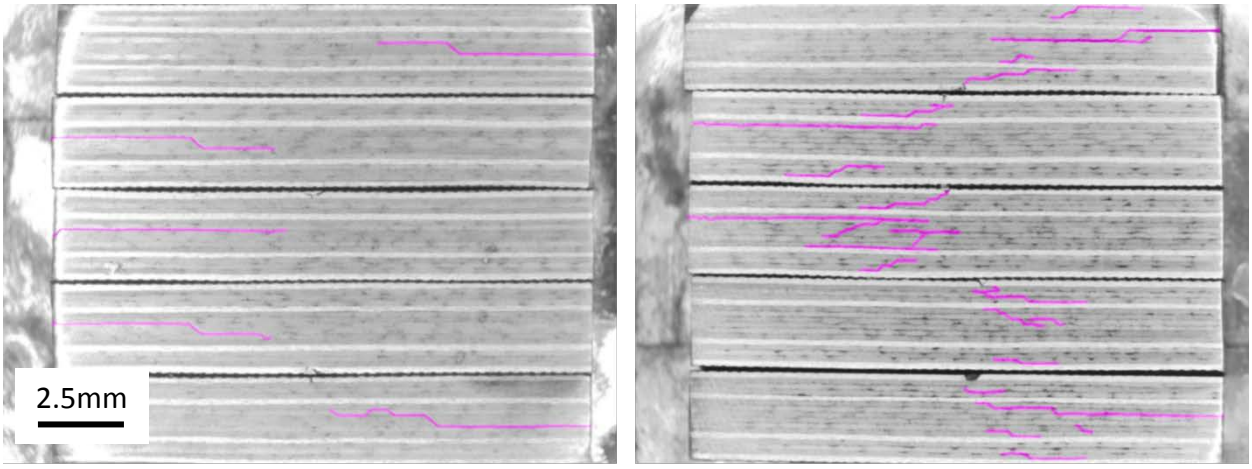

Figure 6-11: Five-coupon images of a Reference and Method 2 nanostitched sample with the cracks traced in NeuronJ, showing crack location differences between reference and nanostitch. The reference coupons fail predominantly on the +45/-45 interfaces near the centerline, while the Method 2 nanostitch coupons fail with crack paths in many locations.

The major crack locations (longest cracks) were recorded for five coupons in every sample. Closest to the midplane (under the loading nose) of the sample was considered the 'start' of the crack, and where the crack encountered the side of the sample was considered the 'end' of the crack. This nomenclature was adopted due to the small likelihood of cracks starting in the low stress regions at the outside edges of the sample (see section 6.3 and [91]), however it is recognized that the actual start/end locations of the cracks cannot be determined as this is a post-mortem analysis. Table 6-1 shows the interface at which the crack 'started' and if it propagated to another interface, the interface where the crack 'ended.' For the Method 2 samples, it was often impossible to determine a major crack, and if there were many cracks the start was labeled 'dist' for distributed. Table 6-1 is color coded; green indicates a valid interlaminar shear strength test due to the crack propagating in the +45/-45 interface near the centerline, yellow indicates the major failure was on the 0/90 interface, and red indicates a multitude of cracks that propagate throughout the exterior cross-section, not just the interface. There were three coupons (out of the 75 analyzed) that failed in a way that did not fit those categories – these three were left white in the table. Upon examining Table 6-1, the differences between reference, Method 1 and Method 2 samples becomes obvious. All but one of the

reference coupons failed in interlaminar shear at the interface near the centerline (a valid ILSS test). Most of Method 1 samples failed in interlaminar shear, however it propagated along the 0/90 interface rather than near the centerline. Note that with the taller 55µm and 63µm nanostitch, some of the Method 1 samples revert to breaking at the +45/-45 interface near the centerline. This may indicate that these nanostitch are past the optimum height, and the dichotomy in crack locations suggest a reason for the high standard deviation seen with the SBS on those samples (Figure 6-3). In Method 2, disregarding sample 2-1 (recall poor transfer at the center plies led to low strengths because the critical interfaces were not reinforced), half of the coupons failed in a combined inter- and intra- laminar 'distributed' mode. Of note is that the shorter 10µm nanostitch sample and half of the tallest 35µm nanostitch sample failed in the same manner as the Method 1 samples. This may indicate that the optimum interlaminar reinforcement comes from Method 2 nanostitch, in the 20-25µm range (because the cracks are propagating through the plies).

Table 6-1: Major crack locations in five coupons per sample. Green indicates a valid ILSS test (interlaminar failure near the centerline). Yellow indicates failure predominately on the 0/90 interface, and red indicates a multitude of cracks both inter- and intra-laminar.

	Coupon				
Sample (Height)	1	2	3	4	5
1-ref1	90/45→0/90	±45	±45	±45	±45
1-ref2	±45	±45	±45	±45	±45 and 0/90
1-1 (15µm)	±45→0/90	90/45→0/90	90/45→0/90	90/45→0/90	90/45→0/90
1-2 (20µm)	++45→0/90	90/45→0/90	±45→0/90	±45→0/90	±45→0/90
1-3 (30µm)	90/45→0/90	90/45→0/90	90/45→0/90	90/45→0/90	90/45→0/90
1-4 (45µm)	90/45→0/90	90/45→0/90	90/45→0/90	++45→0/90	90/45→0/90
1-5 (55µm)	90/45 and 0/45	0/90	90/45→±45	0/90	±45 and 90/45
1-6 (63µm)	±45 and 0/90	±45 and 0/90	±45 and outside 0/45	90/45→0/90	±45→0/90
2-ref1	±45	±45	±45	±45	±45
2-ref2	±45	±45	±45	±45	±45
2-1 (10µm)	±45→0/90	±45→90/45	±45	0/90	0/90→±45
2-2 (15µm)	90/45→0/90	90/45→0/90	90/45→0/90	dist→±45	±45→0/90
2-3 (20µm)	dist→±45	dist	dist→90/45	dist→90/45	±45→0/90
2-4 (25µm)	dist→0/90	dist→0/90	90/45	0/90	dist→±45
2-5 (35µm)	dist→±45	dist ±45 and 0/90	0/90	0/90	±45 and 0/90

To quantify the distribution of cracks in the Method 2 samples, all images were analyzed for total crack length and the number of plies through which the crack propagated ('ply-jumps'). The results are plotted in Figure 6-12, left. As expected, the average number of ply jumps is higher for Method 2, and is greatest in the sample 2-3 coupons: more than twice as many ply jumps occur in that sample as the corresponding height sample 1-2 from Method 1. Despite this increase in ply jumps, the total crack length in each sample is independent of the nanostitch transfer method (Figure 6-12, right). Because all five coupons for each sample were

analyzed in the same image, only one number was obtained for the total crack length of all coupons together (no standard deviation was calculated).

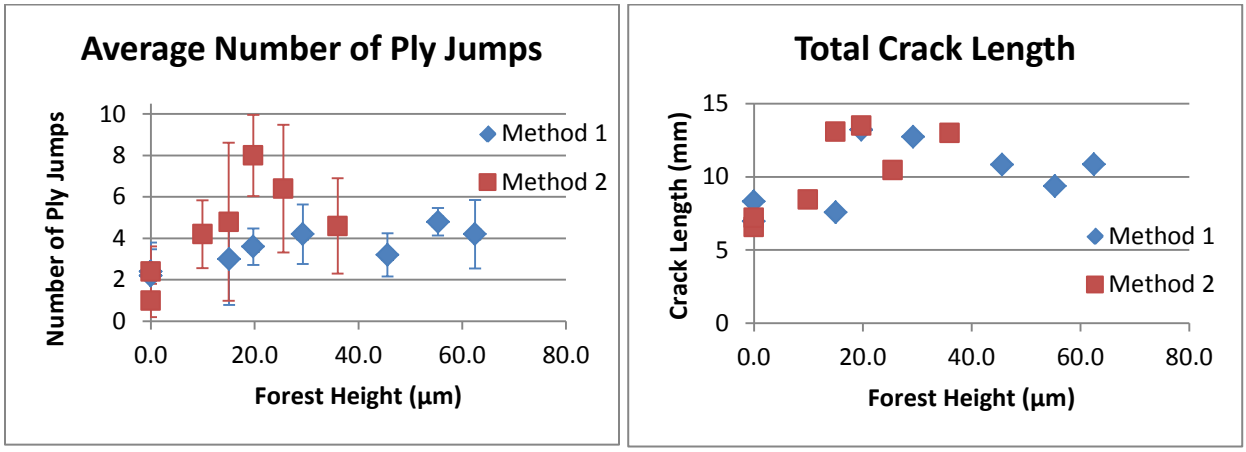

Figure 6-12: Comparison of Method 1 and Method 2 cracks. Left: average number of ply jumps in a coupon is higher for Method 1 than Method 2 (plotted with 2SE). Right: Total crack length is similar between methods.

Because the short beam strengths (SBSs) of the samples were similar between the two methods, it is suspected that the total crack length rather than the deviations through the plies matters with regards to the SBS of the composite. The SBS vs. total crack length is plotted in Figure 6-13, and shows that the SBS is independent of crack length, however there is a clear difference between the reference samples and the nanostitch samples that indicate a change in failure mechanism. Note that this is also reflected in the change in crack locations noted in Table 6-1. A strong caveat on all the analyses in this section is that these are post-mortems from uncontrolled final failure. All specimens did not see the same maximum applied deflection after load is lost in the static test.

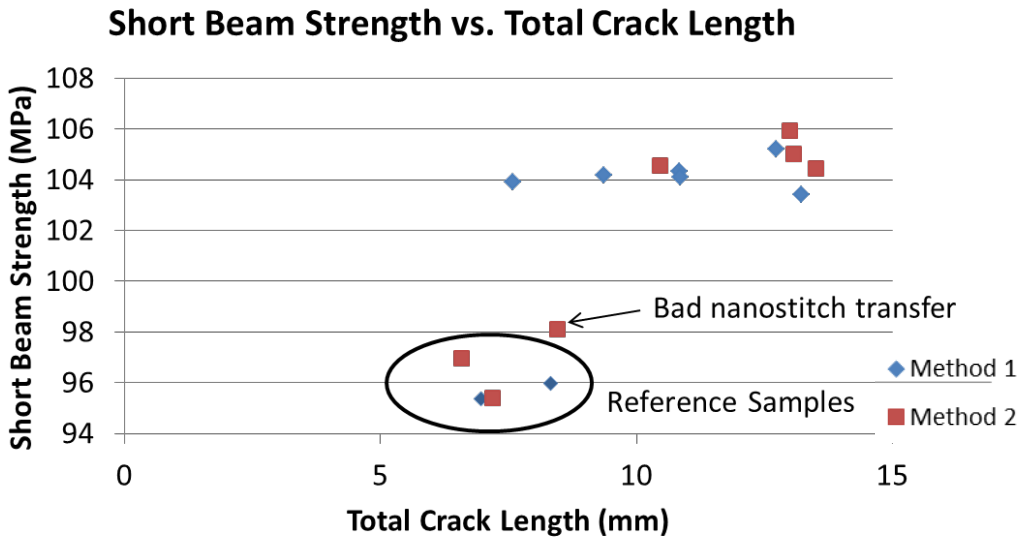

Figure 6-13: SBS vs. Total Crack Length. Plot shows SBS is independent of total crack length, however the nanostitch reinforcement improves SBS over the reference samples for the same crack length.

It was hypothesized that the resin pockets (see discussion in section 5.3.2) may be causing the divergence of cracks into the intra-ply region due to their shape. To investigate this, the five-sample images were again analyzed and the number of ply jumps emanating from (or ending in) resin pockets as well as the total ply jumps were counted. A percentage was calculated and compared to twice the percentage of interface that involves a resin pocket (the factor of two was used due to the ply jumps having two ends). The results are plotted in Figure 6-14, and show that the ply jumps occur independently of the resin pockets. Note however that the counts are somewhat subjective; e.g. in Figure 6-14b, the circled ply jump was not considered to be involved with a resin pocket. Ply jumps that emanated from an area of the interface that contained a resin pocket but propagated in the opposite ply (see circled region in Figure 6-14c), were counted to make an accurate comparison to the interface percentage.

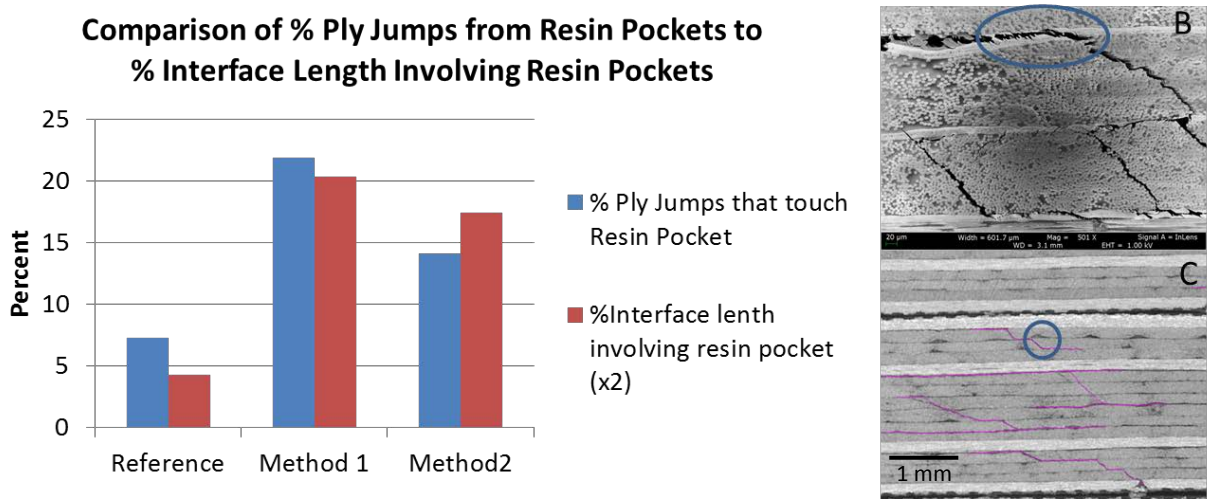

Figure 6-14: Percentage of ply jumps that occur near resin pockets, compared to percentage of the interface that touches a resin pocket. The percentage of ply jumps involved with a resin pocket is correlated with the percentage of interface that contains a resin pocket, indicating that the ply jumps occur independently of the resin pockets. It should be noted that these numbers are somewhat subjective; for instance, in B) the ply jump circled was not counted, while in C) it was.

6.2.2 Improvement Mechanisms

To determine mechanisms of SBS improvement in nanostitched samples, a closer look was taken at the broken coupons. Optical microscope and SEM images were taken of cracks to determine how they formed around the A-CNT nanostitch.

In the optical microscope images, the reference coupons have much straighter cracks than the nanostitched ones (see Figure 6-15). When a macroscopically straight crack in an interface in the nanostitch is viewed at 50x, the cracks are seen to be microscopically wavy, and wander from one side of the interface to the other, even migrating outside of it for significant portions of the length. This is evidence of both strengthening and toughening of the interface, and is interpreted as driving crack formation and propagation away from the A-CNT-reinforced interlaminar regions, and into the intralaminar regions. Also, because the crack frequently

propagates outside of the interface, it may explain why all nanostitch samples fail at approximately the same value; the particular morphology of the nanostitch does not matter if the interface is sufficiently reinforced such that it causes the crack to propagate elsewhere (in the intralaminar regions).

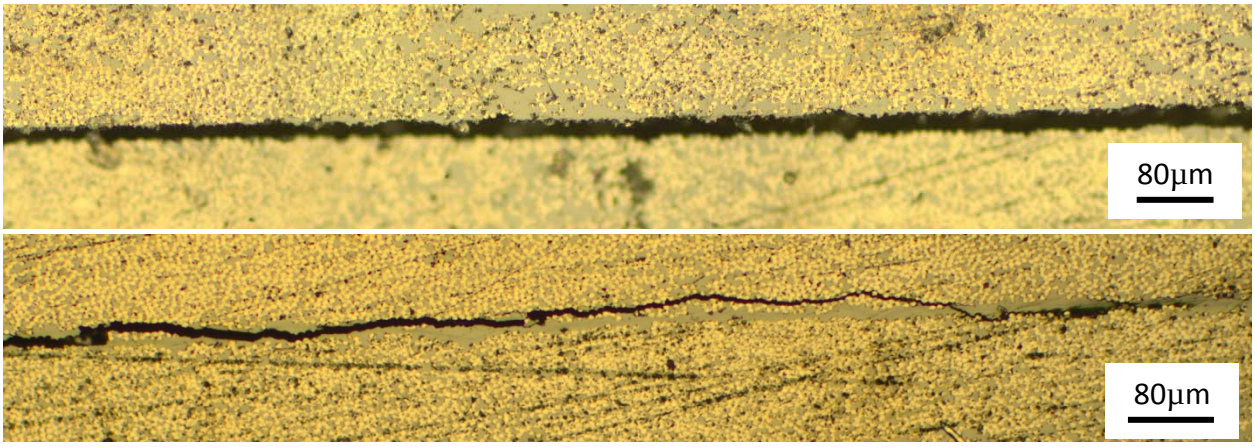

Figure 6-15: Difference in crack morphology along an interface. Top - reference sample, crack propagates straight along an interface. Bottom – Method 1 nanostitched sample (note, nanostitch cannot be seen in this image), where crack wanders in and out of interface and through the nanostitch. Both are fatigue samples from Panel 5.

Two coupons from Method 1 and Method 2 were SEM imaged to compare cracks at the microscopic and nanoscopic level. Qualitatively, cracks in Method 1 and Method 2 appear different in these two samples (it is unknown if they are representative). In Method 1, the nanostitch does not completely fill the interface and the crack appears to wander along the interface, alternating sides and splitting the A-CNT forest in multiple locations. In Method 2, the major crack appears to stay on one side of the nanostitch, while bifurcated cracks are arrested within the forest (Figure 6-16). Both result in longer microscopic crack lengths with more generated surface area than the reference samples.

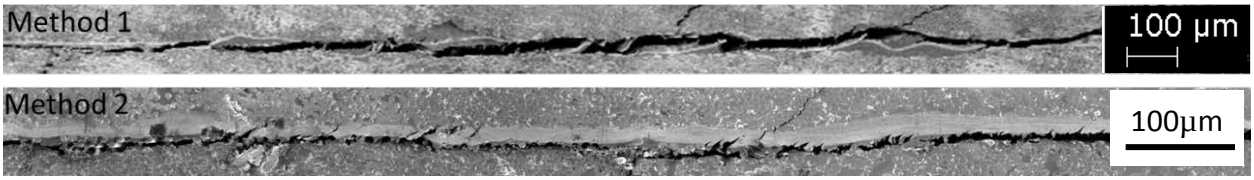

Figure 6-16: Failure regions from Method 1, sample 1-2 (top) and Method 2, sample 2-5 (bottom) coupons.

It should be noted, however, that the overall qualitative differences observed in the crack morphology is from two coupons from each layup method. Even within those coupons, areas can be found in Method 2 where the crack alternates sides of the forest, areas can be found where cracks propagate along one side of the forest in Method 1, and both can show areas where the crack propagates through the center of the reinforced nanostitched region (Figure 6-17). Future studies should quantitatively explore these differences.

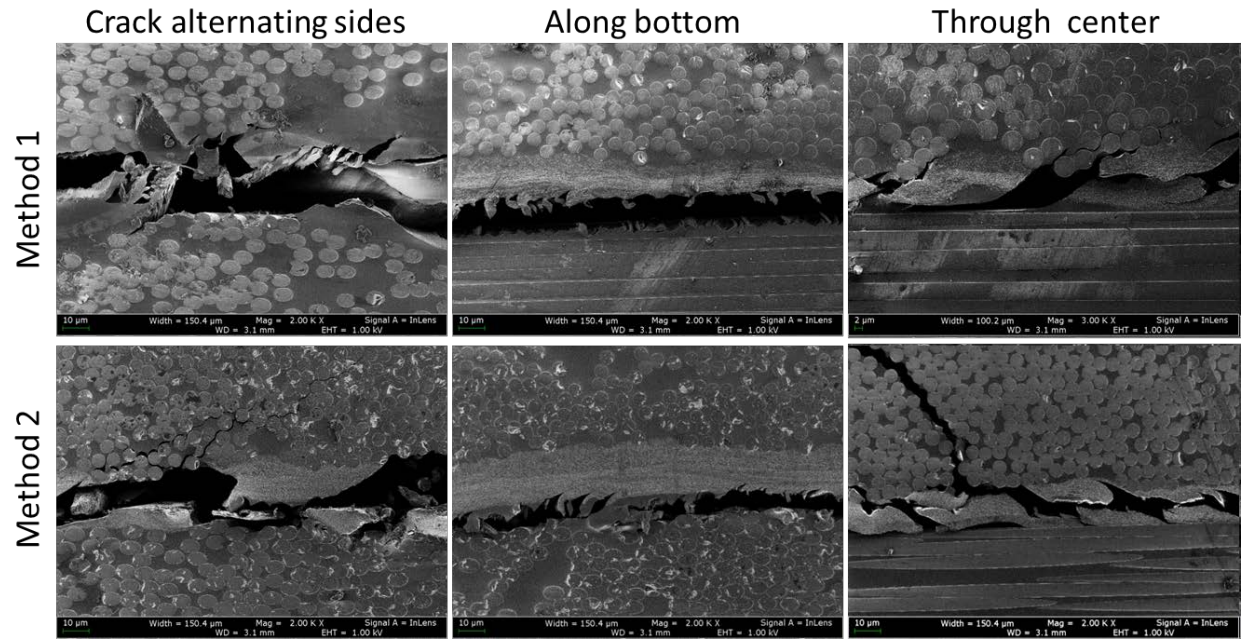

Figure 6-17: SEM images of failure regions in Method 1 (sample 1-2) and Method 2 (sample 2-5) coupons showing examples from all types of crack trajectories.

Areas where cracks propagated through the forest were SEM imaged at higher magnifications (50kx) to observe the fracture surface. It was shown in earlier work [68] that nanotube pullout would result in an increase in Mode 1 (crack opening) fracture toughness because the crack has to overcome the additional frictional force of the nanotubes (that bridge the crack) being pulled out of the matrix to open the crack. This toughness increase (G_{ss}/G_0) is dependent on the length of CNT pullout (L_{CNT}), CNT radius (r), the volume fraction (v_{CNT}), and the interfacial shear strength (τ_c), and the original toughness of the material (G_0) as shown in Equation 4.

Equation 4 [68]:

$$\frac{G_{ss}}{G_0} = 1 + \frac{1}{2}\left(\frac{L_{CNT}}{r}\right)\frac{v_{CNT}\tau_c L_{CNT}}{G_0}$$

Many regions showed clearly observable pullout, up to 1µm in length (Figure 6-18). While the SBS test fails coupons in Mode 2 (in-plane shear without the presence of crack initiators), the Mode 1 fracture toughness model can be used for instructive purposes, and may be representative at some locations in the sample where a crack is locally opening in Mode 1. Using the Mode 1 fracture toughness enhancement model from [68] with a CNT pullout length of 500nm and 8nm diameter, an interfacial shear strength of 100MPa (35-376 MPa reported in [93], average 150: 100MPa chosen to be less than the tensile and shear strength of 8552 of 120MPa [88]) and a 200 J/m^2 fracture toughness for 8552 [94], the increase in Mode 1 fracture toughness would be ~23%. It is interesting to note that this is on the same order as the SBS

increase due to the nanostitch (8.8%). A strong caveat to this analysis is that crack growth as modeled applies to the propagation of cracks after they have initiated, whereas SBS strives to assess strength without any initiated or developed cracks.

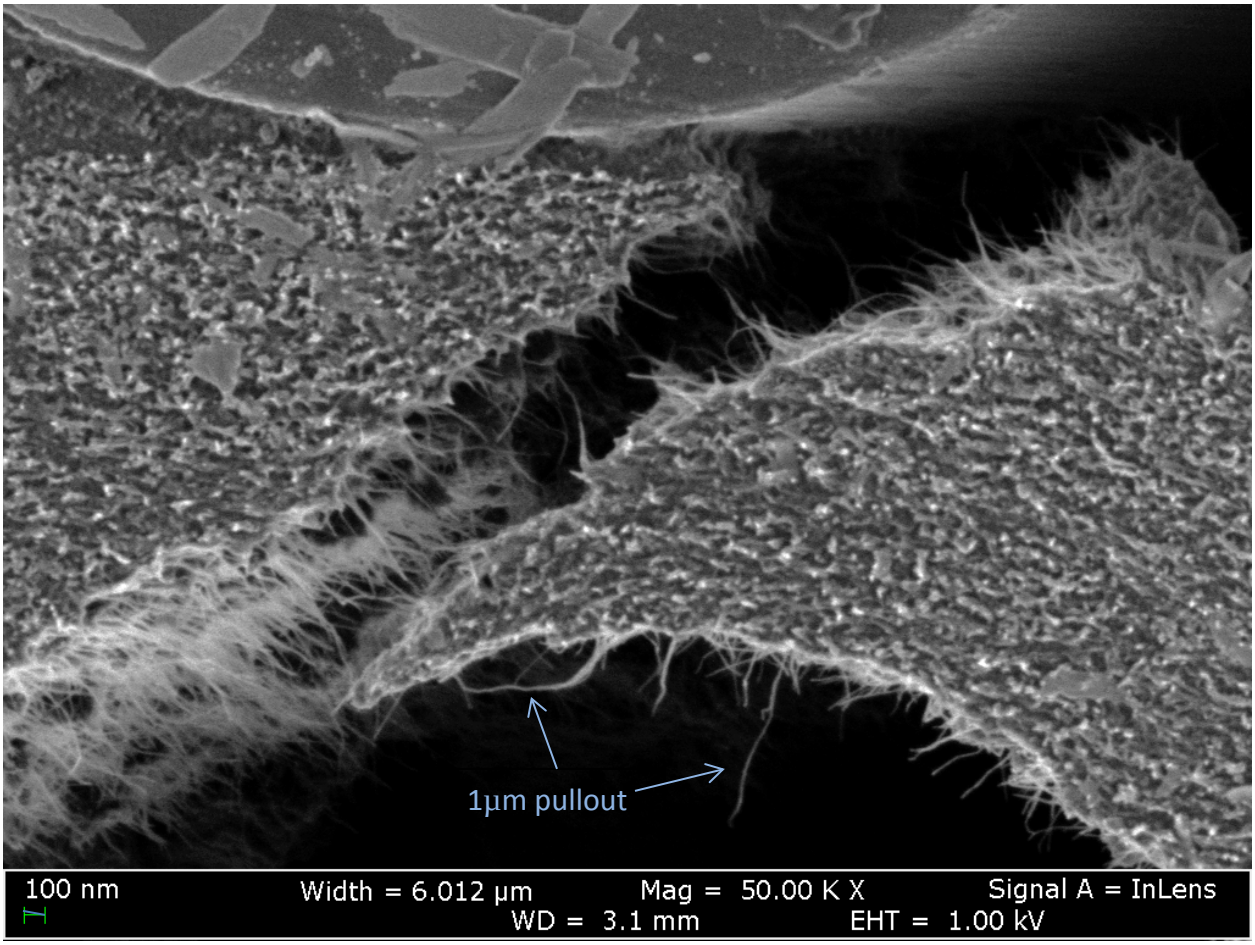

Figure 6-18: Zoomed in image of crack propagating through nanostitched region, showing up to 1µm nanotube pullout. Image from sample panel 3, sample 1-5.

Another interesting phenomenon was observed in many of the nanostitched samples, involving an extra layer of polymer/nanotubes on carbon fibers exposed by cracks. Frequently cracks propagate from one carbon fiber surface to the next along one side of the interface. This is due to the carbon fiber interfacial shear strength being lower than the matrix shear strength. However, in areas where the nanostitch touched the carbon fibers, this occurrence left a uniform layer of polymer/carbon nanotubes covering the carbon fiber (Figure 6-19). Because the images from the

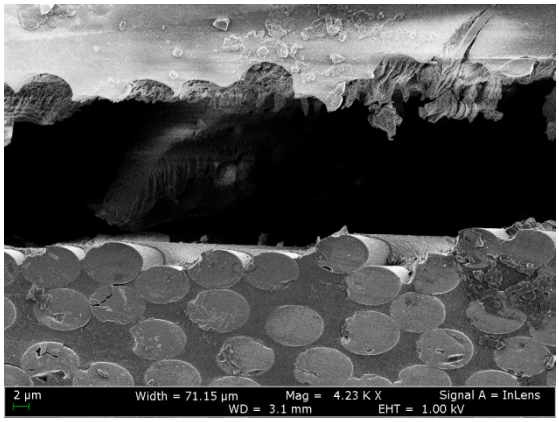

Figure 6-19: Layer of polymer/nanotubes covering exposed carbon fibers in nanostitched coupon (panel 3, sample 1-2).

static coupons rarely show a three-dimensional view, it is difficult to quantify this phenomenon from this sample set. However, images from fatigue surfaces (discussed subsequently along with Figure 6-21) show that this phenomenon is widespread. It is suspected that this layer is at least partially carbon nanotubes (a careful inspection of Figure 6-18 reveals some CNTs coated in polymer adhering to the carbon fiber). It is unknown why this phenomenon is occurring, however due to the uniform thickness of the CNT/polymer coating, it is speculated that the carbon fiber sizing may be playing a role.

6.2.3 Fatigue Analysis

Fatigue samples were difficult to analyze post-mortem due to overshoot at the end of the fatigue test that crushed most of the samples after the test completed. Regardless, optical microscope images were obtained of the failed coupons, and one each of nanostitch and reference was opened to a major crack formed at the 0/90 interface to SEM the crack surfaces in search of beachmarks and other fatigue indicators. In addition, MicroCT was employed to view internal damage of six (three reference, three nanostitch) fatigued coupons that have not been failed.

While it cannot be determined which cracks formed during the test vs. during the overshoot afterwards, the location of all of the cracks can be viewed and compared to the static case. As seen in Figure 6-20, the coupons again had predominant cracks at the +45/-45 interface near the centerline and the 0/90 interface, confirming that these coupons failed in the expected locations. In addition, they frequently had major cracks towards the top/bottom of the coupon and many smaller cracks through the center of the sample under the loading nose – both of these are suspected to have occurred in the load overshoot at the finish of the test.

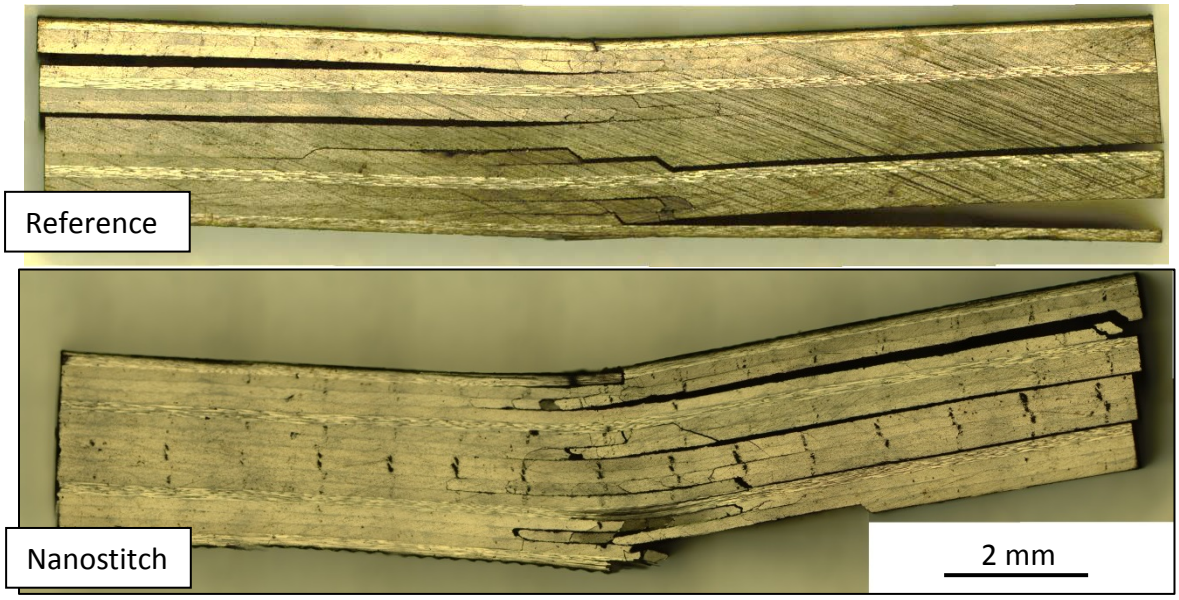

Figure 6-20: Optical images of reference (top) and nanostitched (bottom) fatigued coupons.

SEM imaging of the 0/90 crack surface near the centerline in the nanostitch coupon revealed the presence of a thin polymer/CNT layer covering the carbon fibers (see Figure 6-21). This layer is less than a micron thick, indicating that if there are CNTs in that area (Figure 6-18 suggests that possibility), the nanotubes are being broken at a uniform height. Regardless, the resulting nanostitched crack surface is much rougher than the reference's, and resembles a ductile fracture surface. This nanoscale roughness adds to the surface energy required to advance the crack, and as such is a possible toughening mechanism. Also seen in Figure 6-21 is that microscale crazing (observable by the remnant protrusions from the bridging fibrils) that occurs in the polymer happens on a smaller, more frequent scale in the nanostitched samples, indicating that the microcracking is also occurring on a smaller scale, probably due to the CNTs limiting the size of the voids.

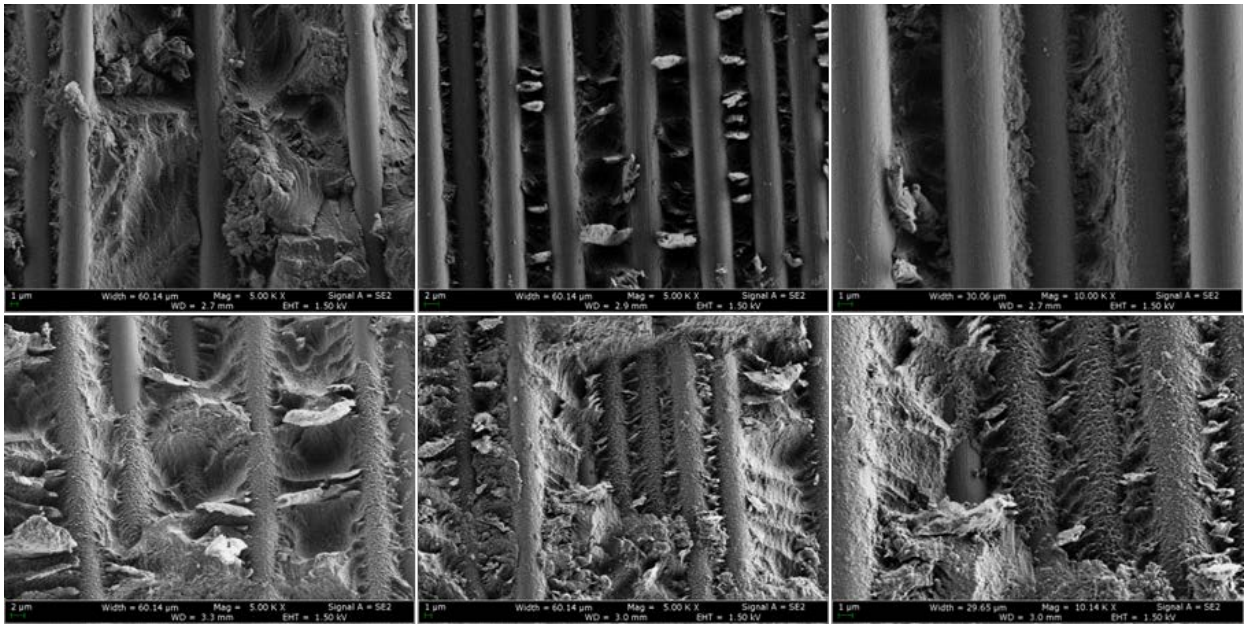

Figure 6-21: SEM images of fracture surfaces on the 0 degree ply from failed fatigue specimens for (top) reference and (bottom) nanostitched specimens. Can see in all images that the carbon fibers (CFs) are bare in the reference coupon but are covered by a thin layer of polymer/CNTs in the nanostitched coupon.

Cracks that form during fatigue testing frequently show 'beachmarks' [95], ridges that indicate crack growth cessation between cycles. A set of SEM images were taken from the start of the crack face on the 0 degree ply and stitched together (Figure 6-22) in an attempt to find beachmarks and quantify the incremental cyclic crack growth if possible. The reference sample displayed periodic beachmarks in about half of the image, with a consistent 190-200 μm spacing. The nanostitched sample showed many more beachmarks, with a few major ones (large ridges) spaced at approximately 200 μm, however in between those were many smaller ridges that indicate shorter crack growth and arrest during cycling, with spacing as small as 30 μm. This indicates that the nanostitch is shortening cyclic crack growth.

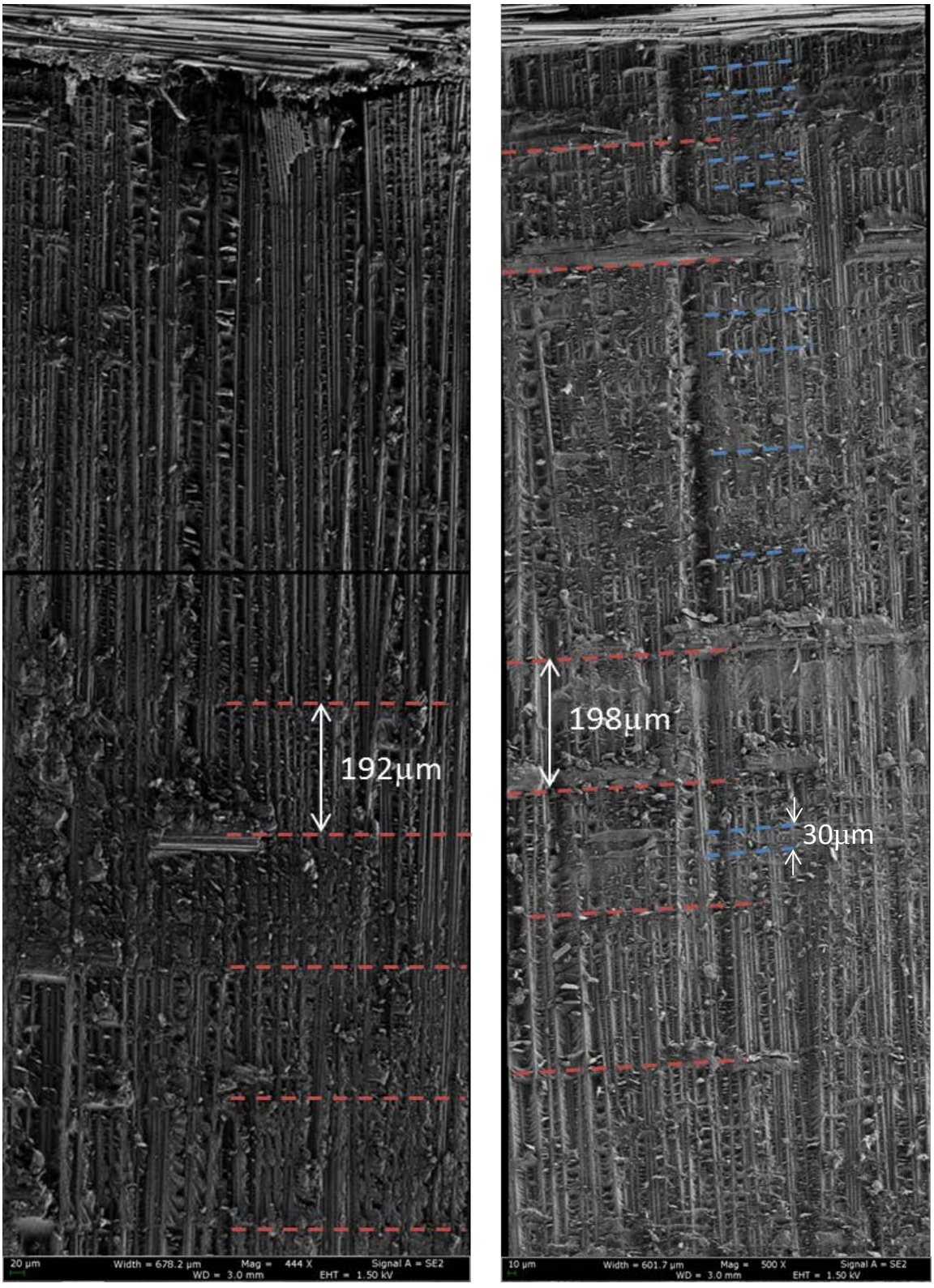

Figure 6-22: Stitched SEM images of the 0/90 crack surface of fatigued coupons. Left –reference, showing periodic beachmarks in a part of the sample. Right – nanostitch, showing some major (red) and many minor (some indicated in blue) beachmarks in the nanostitch sample.

Because of the desire to study crack propagation behavior in the SBS test, two sets of coupons, nanostitch and reference, were partially fatigued, then imaged in a X-Ray Micro-Computed Tomography System (MicroCT) to find where the cracks were initiating. One reference and one nanostitch sample were fatigued at a peak load of 1155N (70% reference strength, ~12,000 cycle life for reference) for 5,000 cycles, then scanned in a MicroCT (Nikon Metrology (X-Tek) HMXST225) at Harvard Center for Nanoscale Systems, then fatigued for another 5000 (total of 10,000) and re-scanned. The second set of coupons was fatigued at 60% reference strength for 100,000 cycles. There was difficulty finding cracks in all images from the first set, so the second set of coupons was soaked with an iodine solution (Benetrac, an old mixture found in the lab), with the understanding that the iodine would penetrate the cracks and the heavier element would illuminate these areas. Dye-penetrant has historically been used to image damage in planar x-ray composite damage investigations, and is in use for CT imaging as well, e.g., [95]. All MicroCT scans were done with the Molybdenum target, 70V, 115µA, with a 1.4s image time, at a 50-54x magnification, with 'minimize ring artifacts' enabled. The scans reconstruct a 3D volume, and from that a 2D image stack was made by slicing this 3D image every 0.003 mm (a total of ~1800 images).

No cracks were visible in the samples fatigued to 5,000 cycles, except one found under the loading nose. It is concluded that this crack is responsible for the sudden compliance increase at ~100 cycles in the samples loaded to 70% of the static reference strength (see Figure 6-9). The 5,000-cycle fatigued coupons were then put back on the Instron and cycled to a total of 10,000 cycles, then re-imaged. It was expected to see microscopic but visible cracks in at least the reference coupon, however no cracks (besides under the loading nose) could be found in either coupon.

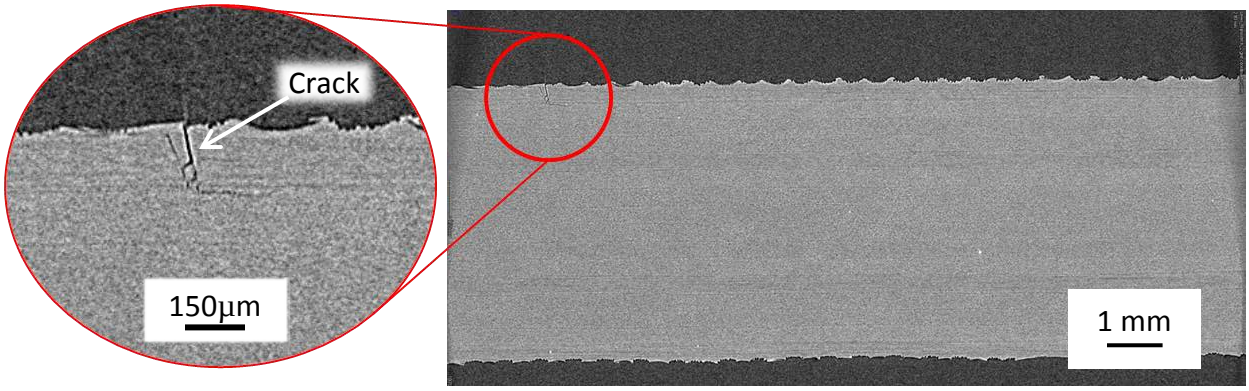

Figure 6-23: Micro-CT image of nanostitched coupon fatigued to 5000 cycles. Only one crack was found, located where the loading nose contacted the sample (see inset), and caused by the compressive stress in that area.

The second set of coupons (reference and nanostitch) was fatigued at 60% of the reference static SBS for 100,000 cycles. Again, only the crack under the loading nose was visible in both samples. The coupons were taken back to the lab and an iodine solution found in the

lab, labeled “Benetrac” was painted onto the outside of the coupons in hopes that the dye would penetrate the cracks, making the areas much brighter in the microCT. The iodine solution was painted onto the coupon surfaces continuously for 20 minutes, then the sample was rinsed in water to remove the penetrant from the surface. The coupons were then re-imaged. Results (Figure 6-24) were no better than before: no internal cracks could be easily seen. The loading nose crack did not appear to have wicked in any iodine, and was not highlighted. However, one more crack was identified near the corner of the sample, and this one was highlighted in the manner expected from the iodine dye penetrant. A more aggressive soaking procedure based on current literature with proper dye penetrant is recommended.

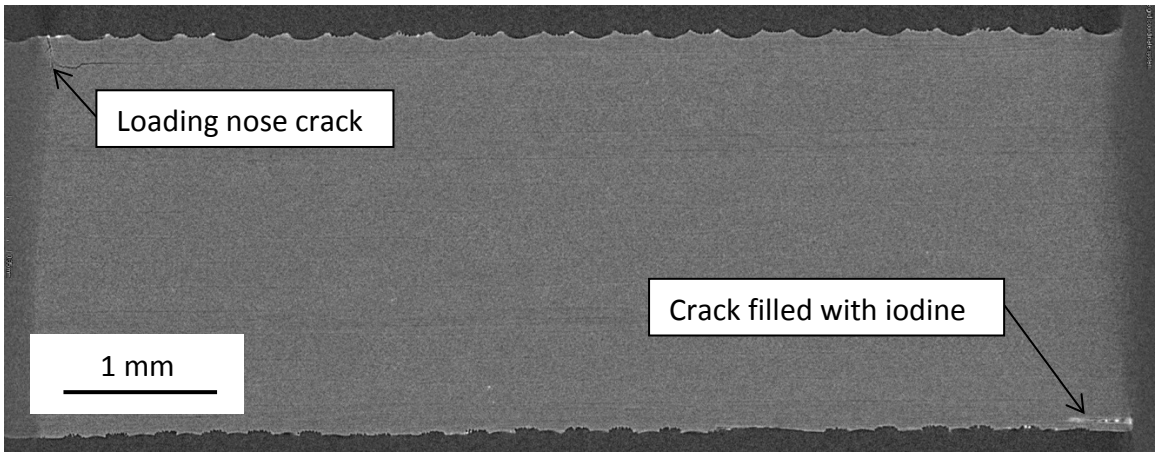

Figure 6-24: Nanostitch sample (Fnano) fatigued to 100,000 cycles. No cracks visible except one at the loading nose and one at the corner (filled with iodine).

Because microscopic cracks were expected in the 10,000 cycle coupons and 100,000 cycle coupons but were unable to be detected, it is suspected that the resolution of the microCT used is not high enough for this application. The resolution at 50x is ~3-5 microns, which means that a crack must have opened by at least this amount to be discernable. While some lines in the images were suspected to be cracks, they were not visible upon inspection of the next image in the stack, and were probably an aberration in the data. See Appendix D for a visualization of a suspected crack. In addition, there was further difficulty in detecting cracks in the nanostitched coupons due to the nanostitch being marginally visible as an interfacial layer. This appears as lines between every layer in the laminate (see the blown up section of Figure 6-23). In an attempt to see the nanostitch layer clearly, a coupon from sample 1-6 (63µm forest) was scanned. To best view the nanostitch layer (~5 µm in the interface, the resolution limit of the instrument), the reconstructed 3D volume was sliced at a shallow diagonal such that the plane passing through each layer would be largest. In this way, the nanostitch layer becomes easily visible (Figure 6-25). The reference coupons do not have visible interfaces.

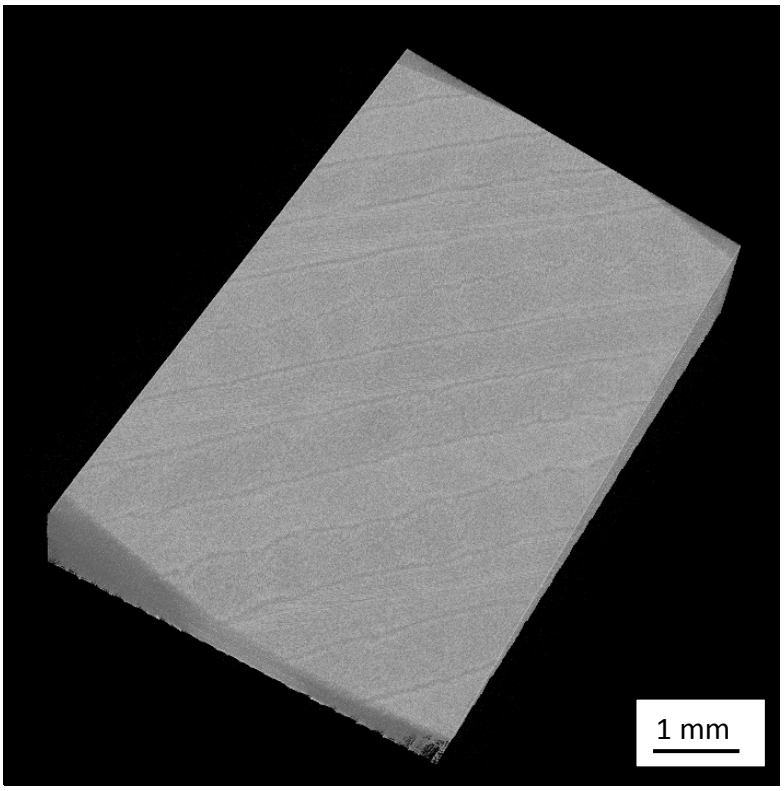

Figure 6-25: 3D view of nanostitch coupon 1-6 (63 micron nanostitch), cut at a shallow angle so that the nanostitch layers can be readily discerned.

6.3 Modeling Short Beam Strength (SBS) Tests in ANSYS

The failures at the +45/-45 interface near the centerline in the reference samples and the failures predominantly in the 0/90 interface nearest the centerline in the nanostitch samples prompted modeling work to confirm that these are high-stress areas. ANSYS Composite Prepost was used in conjunction with Mechanical to analyze the stress distribution in a $[0/90/+45/-45]_{2S}$ layup.

To make the composite model, a 2D geometry on which to build a ply stack was input into Composite Prepost. For the short beam strength (SBS) coupons, the nominal thickness was 2.496mm, so the footprint input was 5mm x 15mm (due to the ASTM standard requirement of 2x and 6x the thickness). The engineering data for IM7/8552 (eg, Young's modulus and strength) was input from Hexcel's datasheet [88] to define a UD ply material. The ply thickness was specified to be 0.156mm, and a $[0/90/+45/-45]_{2S}$ stackup (16 layers) was defined. Because these models simulated 3-point bend, and the standard composites module assumes membrane stresses (no z-directional, ie. through-the-thickness, forces), the model was converted to a solid model before being exported to ANSYS mechanical (a simple option in Composite Prepost - "solid model prefix" is selected to use Solid185 element type in Mechanical).

The mesh was a 0.125mm x 0.125mm x-y element and a 4-micron thick z-element, for a total of 2,995,200 elements. Mesh edge sets were defined where the supports and loading nose would be, in a 3-element wide (0.375mm) swath. Y-direction and Z-direction nodal displacement on the support nodes were set to zero, and a 1200N nodal load on the loading nose edge set (divided amongst all nodes) was defined as the applied force. This force was set to be 80% of the load that failed the coupons in static testing (~1500N).

Once the ANSYS Mechanical solver completed the computation, the results were opened in Composite Prepost. As expected, the x-z shear stress (the expected interlaminar shear failure stress) distribution generally resembled the one reported for the unidirectional SBS coupons [91], however the maximum stress was shown to be in the 0 degree layers closest to the centerline, and the 0 and 90 layers had the highest disparity in stress intensity ply-to-ply. See Figure 6-26 for visualization of the model. It is interesting to note that there is a small anti-symmetry in the model; there is a slightly smaller high stress area in the right-hand side in Figure 6-26. When looking at the opposite face (rotate the model 180 degrees), the smaller stress area is still on the right-hand side. It is unknown why the model produced this anti-symmetry.

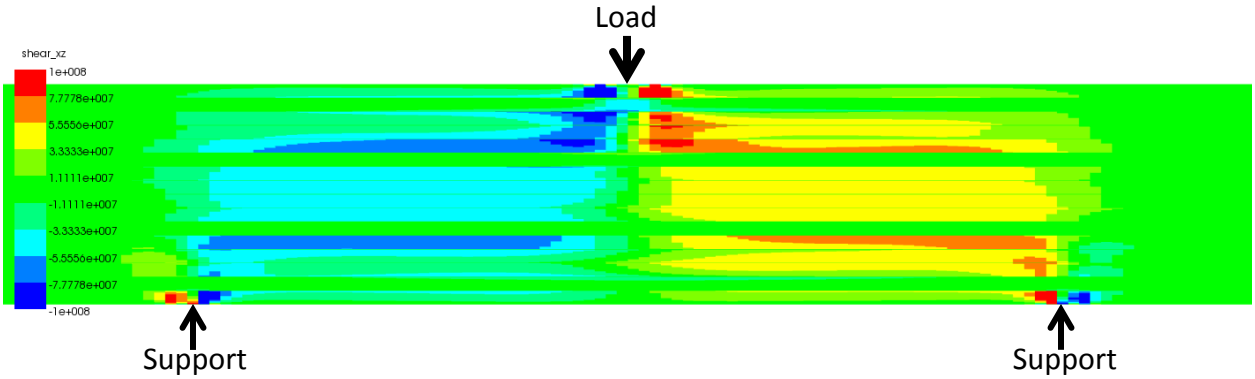

Figure 6-26: Shear x-z stress distribution in Pa. Green is negligible stress; blue and red are high stress regions.

Due to compressive stresses under the loading nose and other possible failure modes, the likelihood of failure, as measured by Tsai-Wu criterion, maximum principle stress and maximum shear stress, as well as Puck criterion (that specifically accounts for delamination), was plotted as well. All showed the same pattern of failure areas; the Tsai-Wu criterion failure map is plotted in Figure 6-27 as a function of the margin of safety. The area under the loading nose and at the supports has the highest likelihood of failure; this is where non-propagating cracks are seen to form first in the SBS coupons. Secondary areas of failure (orange) are in the 90 degree ply and in interlaminar regions at the +45/-45 interfaces near the centerline.

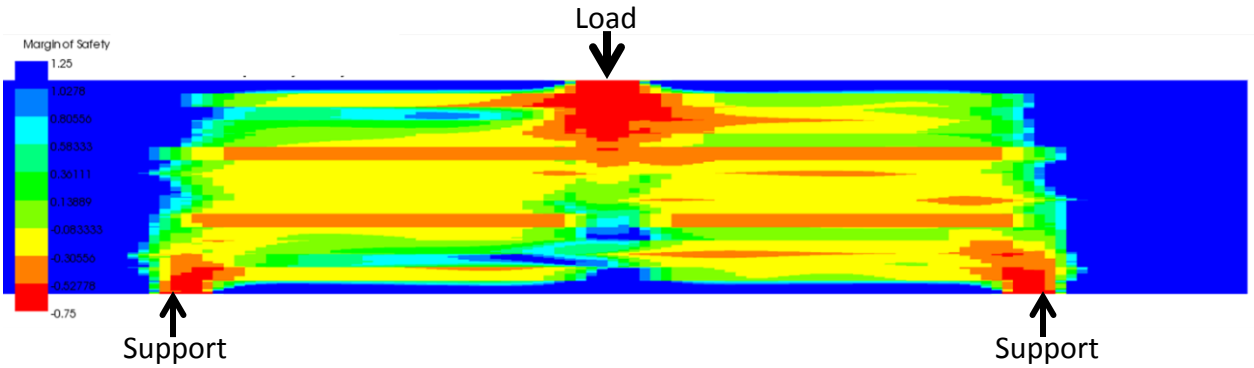

Figure 6-27: Failure likelihood map based on Tsai-Wu criterion, colored by margin of safety - red is most likely to fail, blue is least likely.

When comparing these images to the failed coupons, it becomes immediately apparent that the reference samples failed precisely at the areas of high stress in the +45/-45 interfaces. In fact, if one overlaps the crack in the reference sample with the model, the two interlaminar areas of high stress are linked by a single ply jump (Figure 6-28). In the reference samples, it is reasonable to assume that the crack began as two separate cracks in the high stress areas and connected as the sample failed.

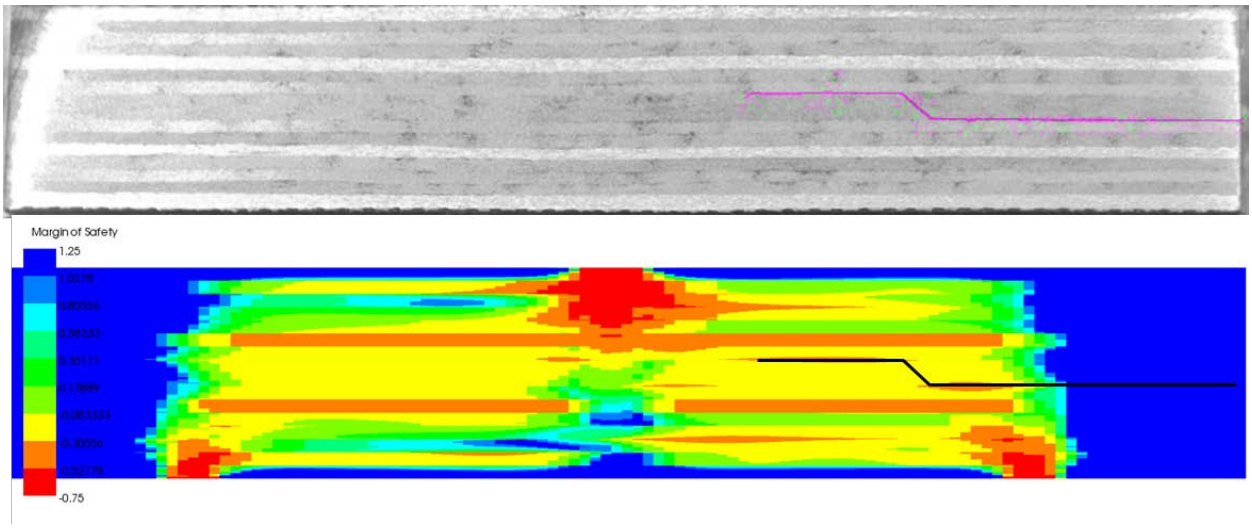

Figure 6-28: Reference sample (1-ref1) comparison to model. Dashed line is crack from reference sample, showing that it overlaps the two areas of high stress concentration at the interfaces.

The nanostitched coupons tended to fail in a multitude of locations, many linked to high stress areas. The major crack tends to appear at the 0/90 interface, a region between high and low stress concentrations within the layers, however others appear in somewhat random locations. It is suspected that as the sample begins to fail, stresses redistribute in ways that cannot be predicted by the model.

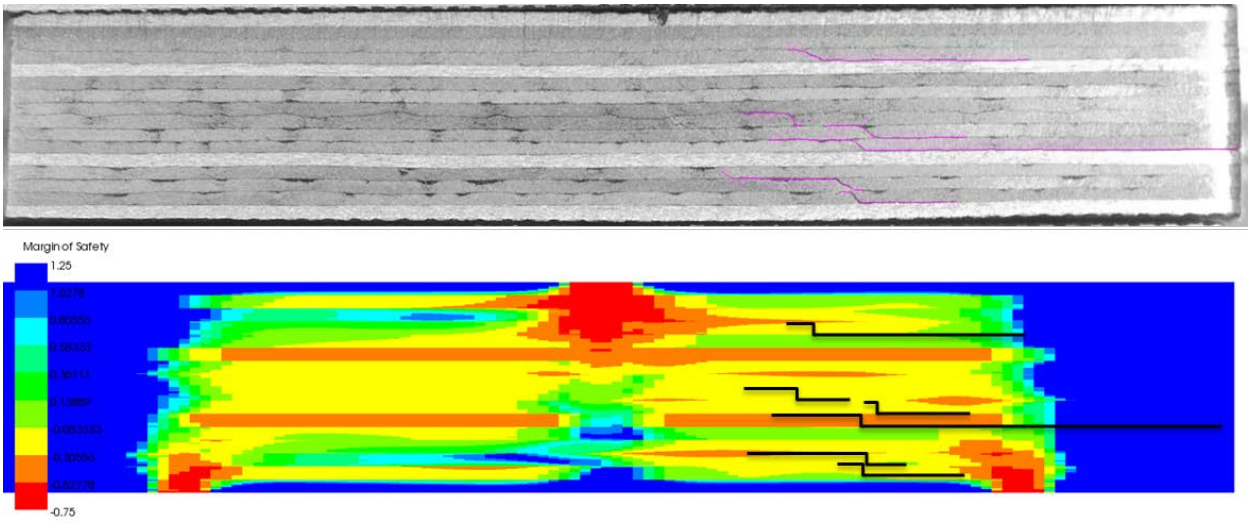

Figure 6-29: Method 2 nanostitched sample (2-3) compared to model.

7 Conclusions and Recommendations

A-CNTs for the purpose of reinforcing composite materials have been grown at MIT for many years with a well-established method, but the resulting A-CNT forest height from that process was highly variable (3-30μm at a 20μm target height). This variability was reduced by instituting control of parameters that were previously unexploited or unknown. Chip position in the furnace was known to be a significant factor in the resulting A-CNT heights. A quartz boat was designed to hold multiple chips and restrict the growth region to ±100mm from the centerline of the furnace. The A-CNT height vs. position (both vertical and horizontal) using this boat was then quantified. Ambient humidity was thought to affect the heights of the A-CNT forest; a procedure was established to bake out the tube before growth to remove the majority of the adsorbed water, and a water bubbler was installed on the furnace to input known ppmv-level amounts of water back into the system during growth. A ~600ppmv water level produces A-CNTs similar to previously grown A-CNTs, as quantified by diameter (8nm), number of walls (3-5), density and waviness (quantified by analyzing SEM images of the forests). It had been known that there was a temperature offset between the furnace thermocouple reading and the temperature on the inside of the growth tube (~80°C), however it was previously unknown what the startup transient specifics were. It was established that the furnace would overshoot the setpoint by up to 120°C, and that the amount of overshoot correlated to the starting temperature of the furnace. The growth occurs as the furnace temperature is decreasing towards its steady-state value, and as a result the growth temperature is 10-40°C hotter than previously though (dependent on the starting temperature of the furnace). Control of the position, water content and starting temperature of the furnace reduced variability to such a degree that 87.4% of A-CNT forests could be produced within ±2μm of the target. For this thesis, target heights ranged from 5 to 65μm; this extended variation was achieved by adjusting only the growth time.

A-CNT forest heights were measured with a new in-house technique that utilized an optical microscope. This technique allowed every A-CNT forest to be non-destructively measured with a repeatability of ±0.78μm. While this method is significantly better than using an SEM to destructively test a few representative forests, it is time consuming and the accuracy is likely user dependent. For future work, an optical microscope with an automated z-stage is recommended so that the ease and repeatability of the measurement increase. A more expensive option could be to use a laser profilometer, however it would greatly increase the speed and accuracy of the measurement.

In addition to stabilizing the growth position, yield per growth was increased by utilizing a quartz boat to hold multiple wafer chips during a single run. The orientation of these chips was preliminarily explored in ANSYS FLUENT; it is expected that a vertical orientation will yield more uniform growth. To further increase yield, it is recommended to use a hot-load system

where the furnace is kept at high temperature at all times. This will allow the ~30-second growths to take place in between 2-minute purges instead of 20-minute heatup and cooldown steps, and increase the throughput approximately tenfold. In addition, the furnace temperature will be stable and a thermocouple can be used as the push rod to measure the temperature at the quartz boat. A water sensor and a new pass-through endcap were purchased for this purpose, but have not been installed. A new safety system will need to be programmed into the controller, and the growth process adjusted to account for the reduction in anneal time. For producing the amount of forests needed for larger composite tests, this new system will be invaluable.

Hexcel IM7/8552 UD prepreg was used to produce composite panels for short beam strength (SBS) testing in shear. To incorporate the A-CNTs into the composite panels, two layup methods were devised that resulted in different nanostitch morphologies. Method 1 used a lower 40°C temperature and pressure to cause a compressed morphology in the resultant nanostitch; Method 2 used a higher 60°C temperature with almost no pressure and a longer wait time to allow the A-CNTs to wick into the prepreg epoxy and maintain their aligned morphology. Seven A-CNT heights ranging from 5-65µm were used in four panels made with Method 1 (one initial panel, one UD panel, one panel for direct comparison to Method 2, and one panel for fatigue testing); Five A-CNT height samples ranging from 10-35µm were made in a Method 2 panel to compare to Method 1.

SEM analysis of the interfaces from these samples showed distinct morphological differences between Method 1 and Method 2. Method 1 forests were all compressed into a tight band in the interface, for example reducing a 63µm tall forest to an average 10µm tall nanostitch. Method 2 more effectively retained the original A-CNT structure, and resulted in nanostitched heights that were close to the original A-CNT height. In addition, Method 2 filled a higher fraction of the interface and was shown to interdigitate with the carbon fibers on either side of the interface.

In addition to the differences seen between Method 1 and Method 2, there were difference noted between the nanostitched samples and the reference samples. First, the interface thickness was spatially variable, resulting in a thickness increase of 8µm on average in the nanostitched samples. This was found to be due to resin pockets that form at the interfaces in the nanostitch samples. These resin pockets formed due to resin migrating out of the plies from resin rich regions at tow-tow junctions inherent in the IM7/8552 prepreg, but form much more frequently (about twice as likely in Method 1) in the nanostitch samples as the reference. The number of resin pockets found in Method 1 was about 20% higher than in Method 2. It was found that the resin that migrated to the interface was doing so by migrating *through* the nanostitch, as if the nanostitch was acting as a membrane. It is noted that no voids were found

in the nanostitched samples, even in a sample cured out-of-autoclave (OOA) in which the rest of the interfaces were riddled with voids. This ability of the nanotubes to wick resin in and through its structure makes the nanostitch of interest in applications where voids can manifest, such as OOA work that includes repair or patching, joining composite parts or just simply curing material. In addition, nanostitch could be used to reinforce and pull resin into ply drops, T joints and other resin-rich areas. Future work should explore these particular areas of interest. For these applications, it is recommended to use Method 1 as the transfer method; it is hypothesized that the increased density of the nanotubes may promote the capillary or membrane forces that move the resin (supported by the increased number of resin pockets seen in the Method 1 samples).

Despite the ability to see significant morphological differences between nanostitch made with Method 1 vs. Method 2, and despite the use of a wide range of forest heights, the resulting short beam strength (SBS) was independent of A-CNT height and layup technique but averaged an 8.75% improvement over the reference samples. This is a significant number that shows the potential for nanostitch use in composite materials. In addition, fatigue testing revealed that the nanostitch had a 3x lifespan of the reference. Again, this is significant; while many things done to increase strength decrease toughness (and therefore fatigue life), nanostitch has improved both properties.

Analysis of the failed specimens reveals both the mechanisms of improvement as well as an explanation of the insensitivity of the results to the nanostitch morphology. Macroscopically, the use of the nanostitch pushes the failure away from the central interface: while the reference coupons fail predominantly at a +45/-45 interface next to the centerline, the nanostitch coupons in Method 1 fail primarily at a 0/90 interface closest to the center, and the Method 2 coupons fail in a mixture of intralaminar failure as well as some similar 0/90 interface failures. ANSYS modeling of the SBS coupons confirm the 0/90 layer closes to the center to be a high-stress area. These away-from-centerline failures mean that the reported strength, though usually given as an interlaminar shear strength value, can only be reported as a short beam strength.

Given the differences in damage morphology between Method 1 and Method 2, one would expect differences in the resulting strength. However, upon closer inspection of the cracks in both methods, it is revealed that even when it appears that a crack forms along an interface, it actually migrates in and out of the interface, spending much of the time in an intra-ply region (Figure 7-1). The resulting strength insensitivity to height or layup technique is thought to be

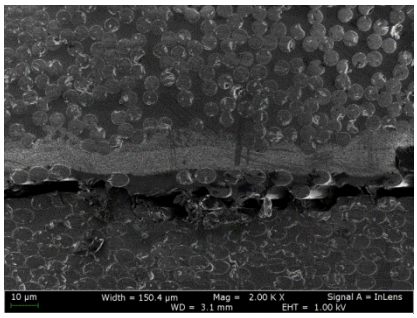

Figure 7-1: Crack migrating just outside of the reinforced interface (sample 2-5).

caused by the major crack migrating in unreinforced areas the majority of the time. I.e., all morphologies of nanostitch seem to be reinforcing the interface well enough to force the fracture elsewhere. It is thought that by decreasing the density of the A-CNT forest, the resulting nanostitch would be able to interdigitate with the carbon fibers more easily (using Method 2 layup), and that there will be a lower density at which the crack will more often propagate in the reinforced region. It is thought that this route would more easily elucidate the differences between A-CNT heights and layup techniques, however it is noted that the true ideal would be to reinforce the entirety of the matrix (such as in a fuzzy fiber architecture [96]) rather than just the interface.

Areas where the crack propagates through the nanostitch were SEM imaged at high magnification to determine mechanisms of reinforcement. Multiple crack paths were seen within the forest, again dissipating energy by generating more surface area. Significant nanotube pullout (up to 1μm) was observed, and is known to increase toughness by increasing the energy required to open the crack. And finally, in some areas of the nanostitch, a thin (<500nm) layer of CNTs/polymer was left behind covering the carbon fibers (frequently cracks propagate along the carbon fiber surfaces due to the lower interfacial shear strength in that area), which generated a nanoscopically rough surface (Figure 7-2). Such a toughening mechanism has also been observed recently for A-CNTs grown in the fuzzy fiber architecture tested in Mode 1 static fracture [97]. Crack surfaces from fatigued samples were also imaged, and verified the abundance of the CNT/polymer layer covering the carbon fibers, as well as indicated a smaller cyclic crack growth by the reduction in spacing of the beachmarks. MicroCT scanning of fatigued samples was attempted, but cracks could not be seen at the resolution of the machine.

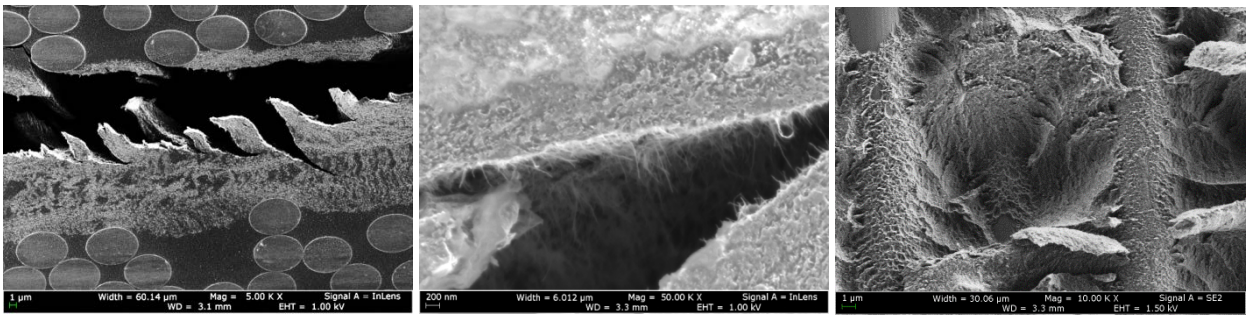

Figure 7-2: Images of nanostitch improvement mechanisms. Left – (sample 2-3) multiple crack paths caused by arrests within the nanostitch, dissipating energy by generating more surface area. Middle – (sample 1-2) nanotube pullout. Right – (sample Fnano) nanoscopically rough layer of CNT/polymer covering the carbon fiber on a crack surface.

In conclusion, nanostitching has been shown to increase short beam strengths and improve fatigue life, however the magnitude of improvement was shown to be insensitive to the forest morphology (height, compression) due to the cracks forming outside of the reinforced interfaces the majority of the time. While the resulting strength was insensitive to

forest height or layup technique, it is interesting to note the differences in crack location and behavior between the two methods, and taking all data together, the author believes that there may be an optimum forest height around 20μm using Method 2 for enhancing SBS. Future work should explore other morphological parameters of the forest, particularly density as it is suspected that decreasing the density will result in better interdigitation with the carbon fibers. In addition, the author notes that while the ideal would be to reinforce the entirety of the matrix with A-CNTs, nanostitching would still have applications in areas such as ply drops, joints and OOA applications such as repair work, and it is suggested that future work explore these applications.

Appendix

A. Old Growth Recipe

Below is an example of the Ansari natural language recipe used to grow prior to starting this work. See section 4.2 for more details.

```
'2008/04/17 Roberto Guzman standard process
'based on standard_growth_1min_andEZD_old.txt with shortened purges
turn log on
' Purge the lines and the tube
set helium to 2070 sccm
set hydrogen to 400 sccm
set ethylene to 400 sccm
turn helium on
turn hydrogen on
turn ethylene on
wait for 2 min
turn ethylene off
wait for 1 min
turn hydrogen off
wait for 5 min
' growing process
set hydrogen to 1040 sccm
set ethylene 400 sccm
turn hydrogen on
turn helium off
sync zones
set zone 1 to 680 deg C
turn zone 1 on
wait for 15 min
turn ethylene on
wait for 50 seconds
turn ethylene off
'delamination
set helium to 500 sccm
turn helium on
wait for 5 minutes
turn hydrogen off
turn zone 1 off
set helium to 1200 sccm
turn hydrogen off
turn zone 1 off
wait 10 minutes
set helium to 300
wait until zone 1 temperature < 225 deg C
turn helium off
turn log off
```

B. New Growth Recipe

Below is an example of the new Ansari natural language program, used in this work. The change from previous recipe is highlighted in yellow. Note that water is added manually to this growth cycle (at 'turn log on'), which allows for the shorter delamination time. See section 4.3 for details.

```
turn log on
' Purge the lines and the tube
set helium to 2070 sccm
set hydrogen to 400 sccm
set ethylene to 400 sccm
turn helium on
turn hydrogen on
turn ethylene on
wait for 2 min
turn ethylene off
wait for 1 min
turn hydrogen off
wait for 5 min

' growing process
set hydrogen to 1040 sccm
turn hydrogen on
turn helium off
sync zones
set zone 1 to 680 deg C
turn zone 1 on
wait for 15 min
set ethylene 400 sccm
turn ethylene on
wait for 50 seconds
turn ethylene off

'delamination
set helium to 500 sccm
turn helium on
wait for 0.5 minutes
turn hydrogen off
turn zone 1 off
set helium to 1200 sccm
turn hydrogen off
turn zone 1 off
wait 10 minutes
set helium to 300
wait until zone 1 temperature < 225 deg C
turn helium off
turn log off
```

C. OrientationJ Coherency Determination

The numbers generated from analyzing the coherency of the nanotube forest was highly variable and seemed to depend on the quality of the image. After searching documentation, it was noted that the program calculates the coherency based on the amount of pixels that are in a line in a particular direction. For horizontal and vertical lines, this method works perfectly:

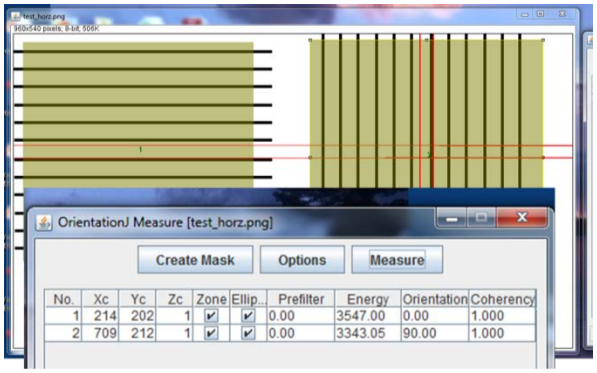

Figure C- 1: Screenshot of OrientationJ plugin showing its ability to calculate coherency for horizontal and vertical lines.

For angled lines, despite the lines actually being perfectly oriented, the program initially calculates a coherency of 0.73. This is due to white pixels being directly in line with black pixels. The program documentation advises using the 'smooth' function and iterating until the coherency converges. On the angled lines, the coherency converged to a final value of 0.994 in five iterations:

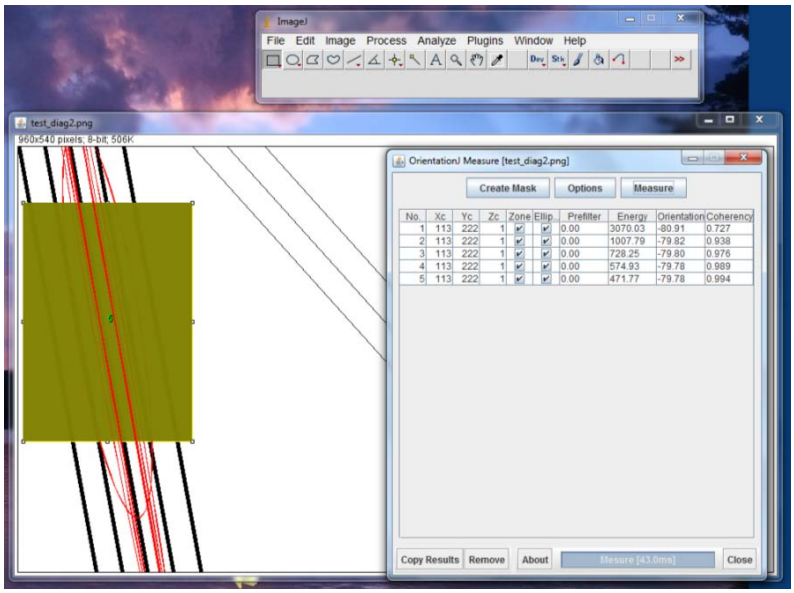

Figure C- 2: Screenshot of OrientationJ converging to the correct coherency after 5 iterations on diagonal lines.

This iteration process was performed on the SEM images, however the convergence wasn't as obvious for the A-CNT images, so five iterations were made on each image and the value reported after the fifth iteration.

D. MicroCT Crack Search

The search for microscopic cracks in fatigued short beam strength samples was difficult at best. The cracks, if there were any, were on the same order as the resolution limit of the microCT used at Harvard CNS. Things that look like cracks but aren't include 0-degree oriented fibers (appear as lines), and abberations in a single image in the stack that also appear as lines, but disappear in the next image in the stack. Things that are *probably* cracks also appear as lines, but smaller and harder to see than the things that are not cracks (see blue circle in image below). These were difficult to spot, but would be visible in the same location for multiple images in a row. These lines were not able to be seen in the nanostitch sample if they coincided with an interface, due to the A-CNT layer also appearing as lines between plies. Unfortunately, the difficulty with finding the cracks meant that every analysis of a set of images resulted in drastically different estimates of where cracks were, and how many. Also, due to the nanostitch layer, no cracks could be found at interfaces in those samples, leading to the highly increased probability of finding cracks in the reference vs. nanostitch sample. The analysis was discarded due to these difficulties.

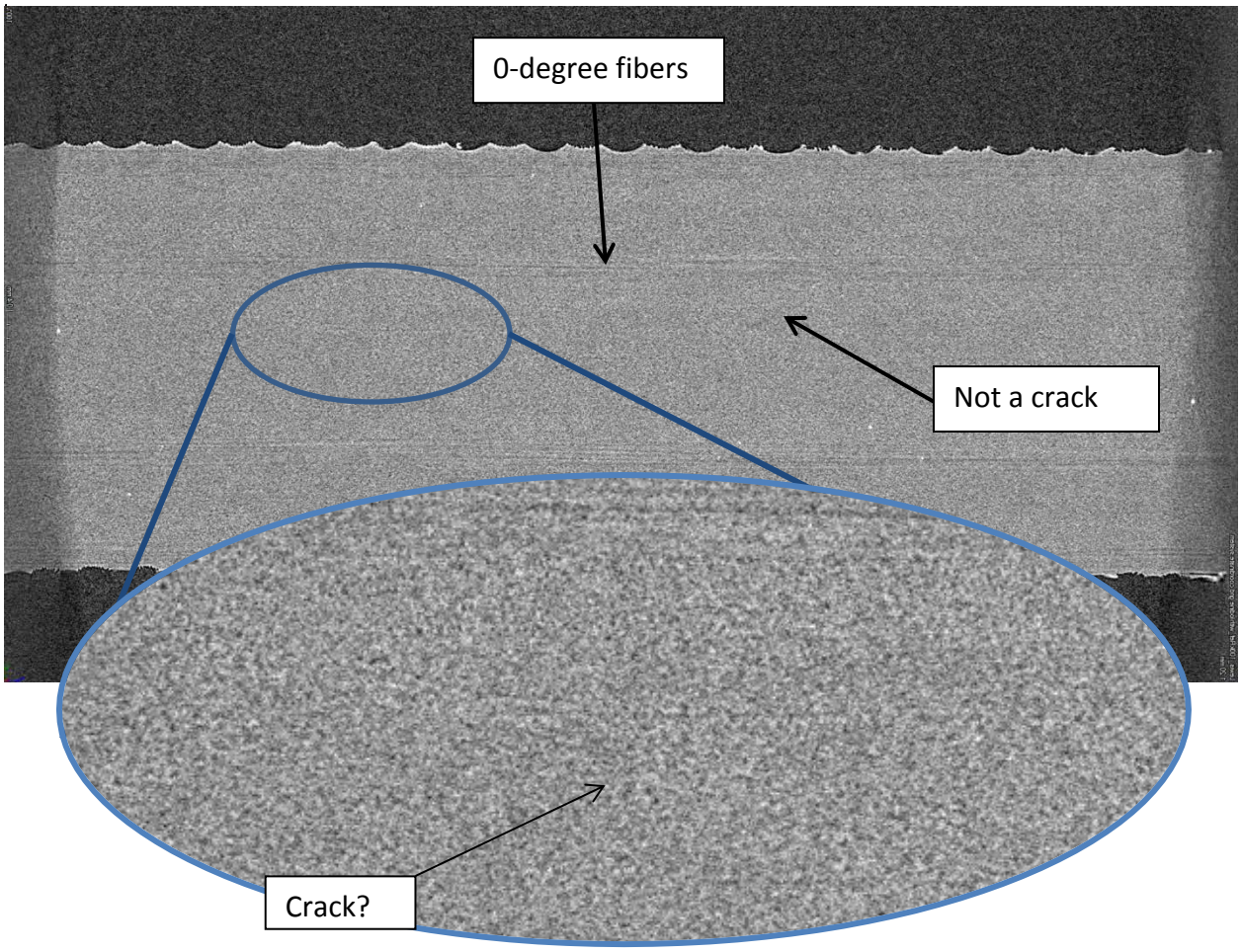

Figure D- 1: A cross-section image from a MicroCT scan showing the difficulty in locating cracks.

References

[1] C. Kassapoglou, Design and Analysis of Composite Structures: With Applications to Aerospace Structures (Aerospace Series), Second edition, West Sussex, UK: Wiley, 2013.

[2] A. Mouritz, "Review of z-pinned composite laminates," *Composites Part A: Applied Science and Manufacturing,* vol. 38, no. 12, pp. 709-728, 2010.

[3] A. Mouritz, K. Leong and I. Herszberg, "A review of the effect of stitching on the in-plane mechanical properties of fibre-reinforced polymer composites," *Composites Part A: Applied Science and Manufacturing,* vol. 28, no. 12, pp. 979-991, 1997.

[4] L. Tong, A. Mouritz and M.K.Bannister, 3D Fibre Reinforced Polymer Composites, Oxford, 2002.

[5] J. T. Vazquez, B. Castanie, J.-J. Barrau and N. Swiergiel, "Multi-Level analysis of low-cost Z-pinned composite joints: Part1: Single Z-pin Behaviour," *Composites Part A: Applied Science and Manufacturing,* vol. 42, no. 12, pp. 2070-2081, 2011.

[6] A. H. Barber, R. Andrews, L. S. Schadler and H. D. Wagner, "On the tensile strength distribution of multiwalled carbon nanotubes," *Applied Physics Letters,* vol. 87, no. 20, p. 203106, 2005.

[7] W. Ding, L. Calabri, K. Kohlhaas, X. Chen, D. Dikin and R. Ruoff, "Modulus, Fracture Strength, and Brittle vs. Plastic Response of the Outer Shell of Arc-grown Multi-walled Carbon Nanotubes," *Experimental Mechanics,* vol. 47, pp. 25-36, 2007.

[8] E. Byrne, M. McCarthy, Z. Xia and W. Curtin, "Multiwall Nanotubes Can be Stronger than Single Wall Nanotubes and Implications for Nanocomposite Design," *Physical Review Letters,* vol. 103, no. 045502, pp. 1-4, 2009.

[9] M.-F. Yu, O. Lourie, M. J. Dyer, K. Moloni, T. F. Kelly and R. S. Ruoff, "Strength and Breaking Mechanism of Multiwalled Carbon Nanotubes Under Tensile Load," *Science,* vol. 287, no. 5453, pp. 637-640, 2000.

[10] S. L. Mielke, D. Troya, S. Zhang, J.-L. Li, S. Xiao, R. Car, R. S. Ruoff, G. C. Schatz and T. Belytschko, "The role of vacancy defects and holes in teh fracture of carbon nanotubes," *Chemical Physics Letters,* vol. 390, no. 4-6, pp. 413-420, 2004.

[11] Hexcel, *HexTow AS4 Carbon Fiber Data Sheet,* Hexcel, 2014.

[12] L. Guan, K. Suenaga and S. Iijima, "Smallest Carbon Nanotube Assigned with Atomic Resolution Accuracy," *Nano Letters,* vol. 8, no. 2, pp. 459-462, 2008.

[13] R. Zhang, Y. Zhang, Q. Zang, H. Xie, W. Qian and F. Wei, "Growth of half-meter long carbon nanotubes based on Schultz-Flory Distribution," *ACS Nano,* vol. 7, no. 7, pp. 6156-6161, 2013.

[14] E. J. Garcia, B. L. Wardle and A. J. Hart, "Joining prepreg composite interfaces with aligned carbon nanotubes," *Composites: Part A,* vol. 39, pp. 1065-1070, 2008.

[15] J. Blanco, E. J. García, R. Guzman de Villoria and B. L. Wardle, "Limiting Mechanisms of Mode I Interlaminar Toughening of Composites Reinforced with Aligned Carbon Nanotubes," *Journal of Composite Materials,* vol. 43, no. 8, pp. 825-841, 2009.

[16] R. Guzman de Villoria, L. Ydrefors, P. Hallander, K. Ishiguro, P. Nordin and B. L. Wardle, "Aligned Carbon Nanotube Reinforcement of Aerospace Carbon Fiber Composites: Substructural Strength Evaluation for Aerostructure Applications," in *AIAA 53rd annual SDM*, Honolulu, HI, April, 2012.

[17] US Department of Energy, "Top 9 Things you didn't know about carbon fiber," US Department of Energy, [Online]. Available: http://energy.gov/articles/top-9-things-you-didn-t-know-about-carbon-fiber. [Accessed 19 12 2015].

[18] Toray Carbon Fibers America, "TORAYCA T1000G Technical Data Sheet CFA-008," Toray Carbon Fibers America, Santa Ana, CA.

[19] Hexcel, "Hextow IM7 Carbon Fiber Product Data," Hexcel, 2014.

[20] Hexcel, "Hextow AS4 Carbon Fiber Product Data Sheet," Hexcel, 2014.

[21] M. Hojo, S. Matsuda, M. Tanaka, S. Ochiai and A. Murakami, "Mode I delamination fatigue properties of interlayer toughened CF/epoxy laminates," *Composite Science and Technology,* vol. 66, pp. 665-675, 2006.

[22] Y. Tang, L. Ye, Z. Zhang and K. Friedrich, "Interlaminar fracture toughness and CAI strength of fibre-reinforced composites with nanoparticles - A review," *Composite Science and Technology,* vol. 86, pp. 26-37, 2013.

[23] C. Kostagiannakopoulou, T. Loutas, G. Sotiriadis, A. Markou and V. Kostopoulos, "On the interlaminar fracture toughness of carbon fiber composites enhanced with graphene nano-species," *Composite Science and Technology,* vol. 118, pp. 217-225, 2015.

[24] S. Meguid and Y. Sun, "On the tensile and shear strength of nano-reinforced composite interfaces," *Materials & Design,* vol. 25, no. 4, pp. 289-296, 2004.

[25] G. G. Tibbets, M. L. Lake, K. L. Strong and B. P. Rice, "A review of the fabrication and properties of vapor-grown carbon nanofiber/polymer composites," *Composites Science and Technology,* vol. 67, no. 7-8, pp. 1709-1718, 2007.

[26] S. Roy, N. Hayes and A. Akepati, "A concurrently coupled multi-scale model for predicting properties of thermoplastic and thermoset polymer nanocomposites," *Mechanics of Nano, Micro and Macro Composite Structures,* pp. 18-20, 2012.

[27] V. Kostopoulos, A. Baltopoulos, P. Karapappas, A. Vavouliotis and A. Paipetis, "Impact and after-impact properties of carbon fiber reinforced composites enhanced with multi-wall carbon nanotubes," *Composite Science and Technology,* vol. 70, no. 4, pp. 553-563, 2010.

[28] M. Hersam, "Progress Towards Monodisperse Single-Walled Carbon Nanotubes.," *Nature Nano,* vol. 3, no. 7, pp. 387-394, 2008.

[29] I. Y. Stein and B. L. Wardle, "Morphology and Processing of Aligned Carbon Nanotube Carbon Matrix Nanocomposites," *Carbon,* vol. 68, pp. 807-813, 2014.

[30] J. Lee, I. Y. Stein, M. E. Devoe, D. J. Lewis, N. Lachman, S. S. Kessler, S. T. Buschorn and B. L. Wardle, "Impact of Carbon Nanotube Length on Electron Transport in Aligned Carbon Nanotube Films," *Applied Physics Letters,* vol. 106, p. 053110, 2015.

[31] L. Schadler, S. Giannaris and P. Ajayan, "Load transfer in carbon nanotube epoxy composites," *Applied Physics Letters,* vol. 73, p. 3824, 1998.

[32] D. Qian, E. Dickey, R. Andrews and T. Rantell, "Load transfer and deformation mechanisms in carbon nanotube polystyrene composites," *Applied Physics Letters,* vol. 76, p. 2868, 2000.

[33] E. Thostenson, "Carbon nanotube/carbon fiber hybrid multiscale composites," *Journal of Applied Physics,* vol. 91, no. 9, pp. 6034-6037, 2002.

[34] J. N. Coleman, U. Khan, W. J. Blau and Y. K. Gun'ko, "Small but strong: A review of the mechanical properties of carbon nanotube-polymer composites," *Carbon,* vol. 44, no. 9, pp. 1623-1652, 2006.

[35] R. Andrews and M. Weisenberger, "Carbon nanotube polymer composites," *Current Opinion in Solid State and Materials Science,* vol. 8, no. 1, pp. 31-37, 2004.

[36] J. Qiu, C. Zhang, B. Wang and R. Liang, "Carbon nanotube integrated multifunctional multiscale composites," *Nanotechnology,* vol. 18, no. 27, 2007.

[37] Y.-K. Yang, L.-J. Yu, R.-G. Peng, Y.-L. Huang, C.-E. He, H.-Y. Liu, X.-B. Wang, X.-L. Xie and Y.-W. Mai, "Incorporation of liquid-like multiwalled carbon nanotubes into an epoxy matrix by solvent-free processing," *Nanotechnology,* vol. 23, no. 22, 2012.

[38] A. M. Esawi and M. M. Farag, "Carbon nanotube reinforced composites: Potential and current challenges," *Materials & Design,* vol. 28, no. 9, pp. 2394-2401, 2007.

[39] G. Lubineau and A. Rahaman, "A review of strategies for improving the degradation properties of laminated continuous-fiber/epoxy composites with carbon-based reinforcements," *Carbon,* vol. 50, no. 7, pp. 2377-2395, 2012.

[40] C. A. Dyke and J. M. Tour, "Covalent Functionalization of Single-Walled Carbon Nanotubes for Materials Applications," *Journal of Physical Chemistry A,* vol. 108, no. 51, pp. 11151-11159, 2004.

[41] J. Zhu, J. Kim, H. Ping, J. L. Margrave, V. N. Khabashesku and E. V. Barrera, "Improving the Dispersion and Integration of Single-Walled Carbon Nanotubes in Epoxy Composites through Functionalization," *Nano Letters,* vol. 3, no. 8, pp. 1107-1113, 2003.

[42] S. Wang, Z. Liang, T. Liu, B. Wang and C. Zhang, "Effective amino-functionalization of carbon nanotubes for reinforcing epoxy poymer composites," *Nanotechnology,* vol. 17, no. 6, 2006.

[43] Z. Yaping, Z. Aibo, C. Qinghua, Z. Jiaoxia and N. Rongchang, "Functionaization effect on carbon nanotube/epoxy nano-composites," *Materials Science and Engineering: A,* Vols. 435-436, pp. 145-149, 2006.

[44] X. Gong, J. Liu, S. Baskaran, R. D. Voise and J. S. Young, "Surfactant-Assisted Processing of Carbon Nanotube/ Polymer Composites," *Chemistry of Materials,* vol. 12, no. 4, pp. 1049-1052, 200.

[45] P.-C. Ma, S.-Y. Mo, B. Z. Tang and J.-K. Kim, "Dispersion, interfacial interaction and re-agglomeration of functionalized carbon nanotubes in epoxy composites," *Carbon,* vol. 48, no. 6, pp. 1824-1834, 2010.

[46] E. T. Thostenson and T.-W. Chou, "Processing-structure-multi-functional property relationship in carbon nanotube/epoxy composites," *Carbon,* vol. 44, no. 14, pp. 3022-3029, 2006.

[47] X.-L. Xie, Y.-W. Mai and X.-P. Zhou, "Dispersion and alignment of carbon nanotubes in polymer matrix: a review," *Materials Science and Engineering: R: Reports,* vol. 49, no. 4, pp. 89-112, 2005.

[48] P. Potschke, T. Fornes and D. Paul, "Rheological behavior of multiwalled carbon nanotube/polycarbonate composites," *Polymer,* vol. 43, no. 11, pp. 3247-3255, 2002.

[49] Zyvex Technologies, "Arovex Prepreg," [Online]. Available: http://www.zyvextech.com/arovex/. [Accessed 24 11 2015].

[50] Zyvex Technologies, "Aerovex SC Prepreg System Zyvex Nano Engineered Composite," Zyvex Technologies, 2014.

[51] J. Chen, H. Liu, W. A. Weimer, M. D. Halls, D. H. Waldeck and G. C. Walker, "Noncovalent Engineering of Carbon Nanotube Surfaces by Rigid, Functional," *JACS Communications,* vol. 124, no. 31, pp. 9034-9035, 2002.

[52] W. Downs and R. Baker, "Modification of the surface properties of carbon fibers via the catalytic growth of carbon nanofibers," *Journal of Materials Research,* vol. 10, no. 3, pp. 625-633, 1995.

[53] Z.-G. Zhao, L.-J. Ci, H.-M. Cheng and J.-B. Bai, "The growth of multi-walled carbon nanotubes with different morphologies on carbon fibers," *Carbon,* vol. 43, pp. 651-673, 2005.

[54] F. Cesano, S. Bertarione, D. Scarano and A. Zecchina, "Connecting Carbon Fibers by Means of Catalytically Grown Nanofilaments: Formation of Carbon-Carbon Composites," *Chemistry of Materials,* vol. 17, no. 20, pp. 5119-5123, 2005.

[55] K. Kepple, G. Sanborn, P. Lacasse, K. Gruenberg and W. Ready, "Improved fracture toughness of carbon fiber composite functionalized with multi walled carbon nanotubes," *Carbon,* vol. 46, no. 15, pp. 2026-2033, 2008.

[56] Q. Zhang, J. Liu, R. Sager, L. Dai and J. Baur, "Hierarchical composites of carbon nanotubes on carbon fiber: influence of growth condition on fiber tensile properties," *Composite Science and Technology,* vol. 69, pp. 594-601, 2009.

[57] E. J. Garcia, B. L. Wardle, A. J. Hart and N. Yamamoto, "Fabrication and multifunctional properties of a hybrid laminate with aligned carbon nanotubes grown In Situ," *Composites Science and Technology,* vol. 68, no. 9, pp. 2034-2041, 2008.

[58] E.J. Garcia, A.J. Hart, B.L. Wardle and A.H. Slocum, "Fabrication of composite microstructures by capillarity-driven wetting of aligned carbon nanotubes with polymers," *Nanotechnology,* vol. 18, no. 16, p. 165602, 2007.

[59] H. Qian, A. Bismarck, E. S. Greenhalgh and M. S. Shaffer, "Carbon nanotube grafted carbon fibres: A study of wetting and fibre fragmentation," *Composites Part A: Applied Science and Manufacturing,* vol. 41, no. 9, pp. 1107-1114, 2010.

[60] F. An, C. Lu, J. Guo, S. He, H. Lu and Y. Yang, "Preparation of vertically aligned carbon nanotube arrays grown onto carbon fiber fabric and evaluating its wettability on effect of composite," *Applied Surface Science,* vol. 258, no. 3, pp. 1069-1076, 2011.

[61] R. Sager, P. Klein, D. Lagoudas, Q. Zhang, J. Liu, L. Dai and J. Baur, "Effect of carbon nanotubes on the interfacial shear strength of T650 carbon fiber in an epoxy matrix,"

Composite Sciene and Technology, vol. 69, no. 7-8, pp. 898-904, 2009.

[62] J. Abot, Y. Song, M. Schultz and V. Shanov, "Novel carbon nanotube array-reinforced laminated composite materials with higher interaminar elastic properties," *Composites Science and Technology,* vol. 68, no. 13, pp. 2755-2760, 2008.

[63] Y. Zeng, L. Ci, B. J. Carey, R. Vajtai and P. M. Ajayan, "Design and Reinforcement: Vertically Aligned Carbon Nanotube-Based Sandwich Composites," *ACS Nano,* vol. 4, no. 11, pp. 6798-6804, 2010.

[64] M. Kim, Y.-B. Park, O. I. Okoli and C. Zhang, "Processing, characterization, and modeing of carbon nanotube-reinforced multiscale composites," *Composite Science and Technology,* vol. 69, pp. 335-342, 2009.

[65] V. P. Veedu, A. Cao, X. Li, K. Ma, C. Soldano, S. Kar, P. M. Ajayan and M. N. Ghasemi-Nejhad, "Multifunctional composites using reinforced laminae with carbon-nanotube forests," *Nature Materials,* vol. 5, pp. 457-462, 2006.

[66] S. U. Khan and J.-K. Kim, "Impact and Delamination failure of Multiscale Carbon Nanotube-Fiber Reinforced Polymer Composites: A Review," *International Journa of Aeronautical & Space Science,* vol. 12, no. 2, pp. 15-133, 2011.

[67] E. J. Garcia, B. L. Wardle and A. J. Hart, "Joining prepreg composite interfaces with aligned carbon nanotubes," *Composite Part A: Applied Sciene and Manufacturing ,* vol. 39, no. 6, pp. 1065-1070, 2008.

[68] J. Blanco, E. J. Garcia, R. Guzman de Villoria and B. L. Wardle, "Limiting Mechanisms of Mode I Interlaminar Toughening of Composites Reinforced with Aligned Carbon Nanotubes," *Journal of Composite Materials,* vol. 43, no. 8, pp. 825-841, 2009.

[69] R. G. d. Villoria, L. Ydrefors, P. Hallander, K. Ishiguro, P. Nordin and B. Wardle, "Aligned Carbon Nanotube Reinforcement of Aerospace Carbon Fiber Composites: Substructural Strength Evaluation for Aerostructure Applications," in *53rd AIAA/ASME/ASCE/AHS/ASC Structures, Structural Dynamics and Materials Conference*, Honolulu, HI, 2012.

[70] C. Mattevi, C. T. Wirth, S. Hofmann and R. Blume, "In-situ X-ray Photoelectron Spectroscopy Study of Catalyst-Support Interactions and Growth of Carbon Nanotube Forests," *Journal of Physical Chemistry C,* vol. 112, p. 12207–12213, 2008.

[71] R. Guzman de Villoria, A. Hart and B. Wardle, "Continuous high-yield production of vertically aligned carbon nanotubes on 2D and 3D substrates," *ACS Nano,* vol. 5, no. 6, pp. 4850-4857, 2011.

[72] S. A. S. III, *Carbon nanotube growth on challenging substrates : applications for carbon-fiber composites,* Cambridge, MA: Massachusetts Institute of Technology, 2012.

[73] K. Hata, D. N. Futaba, K. Mizuno, T. Namai, M. Yumura and S. Iijima, "Water-Assisted Highly Efficient Synthesis of Impurity-Free Single-Walled Carbon Nanotubes," *Science,* vol. 306, no. 5700, pp. 1362-1364, 2004.

[74] S. Patolea, P. Alegaonkarb, H.-C. Leeb and J.-B. Yoo, "Optimization of water assisted chemical vapor deposition parameters for super growth of carbon nanotubes," *Carbon,* vol. 46, no. 14, pp. 1987-1993, 2008.

[75] D. N. Futaba, K. Hata, T. Yamada, K. Mizuno, M. Yumura and S. Iijima, "Kinetics of Water-

Assisted Single-Walled Carbon Nanotube Synthesis Revealed," *Physical Review Letters,* vol. 95, no. 056104, pp. 1-4, 2005.

[76] P. B. Amama, C. L. Pint, L. McJilton, S. M. Kim, E. A. Stach, P. T. Murray, R. H. Hauge and B. Maruyama, "Role of Water in Super Growth of Single-Walled Carbon Nanotube Carpets," *Nano Letters,* vol. 9, no. 1, pp. 44-49, 2009.

[77] C. R. Oliver, E. S. Polsen, E. R. Meshot, S. Tawfick, S. J. Park, M. Bedewy and A. Hart, "Statistical Analysis of Variation in Laboratory Growth of Carbon Nanotube Forests and Recommendations For Improved Consistency," *ACS Nano,* vol. 7, no. 4, pp. 3565-3580, 2013.

[78] S. Noda, K. Hasegawa, H. Sugime, K. Kakehi, Z. Zhang1, S. Maruyama and Y. Yamaguchi, "Millimeter-Thick Single-Walled Carbon Nanotube Forests: Hidden Role of Catalyst Support," *Japanese Journal of Applied Physics,* vol. 46, no. 2, pp. 17-19, 2007.

[79] M. Carr, "extreme chemical o-rings," [Online]. Available: http://www.mcmaster.com/#kalrez-o-rings/=10hh5b1. [Accessed 30 12 2015].

[80] J. S. C. Kim, "The Role of Hydrogen in the Growth of Carbon Nanotubes:A Study of the Catalyst State and Morphology," MIT , Cambridge, MA, 2007.

[81] A. J. Hart and A. H. Slocum, "Rapid Growth and Flow-Mediated Nucleation of Millimeter-Scale Aligned Carbon Nanotube Structures from a Thin-Film Catalyst," *J. Phys. Chem. B,* vol. 110, pp. 8250-8257, 2006.

[82] I. Y. Stein and B. L. Wardle, "Coordination number model to quantify packing morphology of aligned nanowire arrays," *Physical Chemistry Chemical Physics,* vol. 15, pp. 4033-4040, 2013.

[83] I.Y. Stein, N. Lachman, M. E. Devoe and B. L. Wardle, "Exohedral Physisorption of Ambient Moisture Scales Non-monotonically with Fiber proximity in Aligned Carbon Nanotube Arrays," *ACS Nano,* vol. 8, no. 5, pp. 4591-4599, 2014.

[84] D. Handlin, I. Y. Stein, R. Guzman de Villoria, H. Cebeci, E. M. Parsons, S. Socrate, S. Scotti and B. L. Wardle, "Three-Dimensional Elastic Constitutive Relations of Aligned Carbon Nanotube Architectures," *Journal of Applied Physics,* vol. 114, p. 224310, 2013.

[85] B. Natarajan, N. Lachman, T. Lam, D. Jacobs, C. Long, M. Zhao, B. L. Wardle, R. Sharma and A. J. Liddle, "The Evolution of Carbon Nanotube Network Structure in Unidirectional Nanocomposites Resolved by Quantitiative Electron Tomography," *ACS Nano,* vol. 9, no. 0, pp. 6050-6058, 2015.

[86] I. Y. Stein, D. J. Lewis and B. L. Wardle, "Aligned Carbon Nanotube Array Stiffness from Stochastic Three-Dimensional Morphology," *Nanoscale,* pp. 19426 - 19432, 2015.

[87] H. Cebeci, R. Guzman de Villoria, A. J. Hart and B. L. Wardle, "Multifunctional properties of high volume fraction aligned carbon nanotube polymer composites with controlled morphology," *Composites Science and Technology,* vol. 69, no. 15-16, pp. 2649-2656, 2009.

[88] Hexcel Composites, *FTA-072e Hexply 8552 Epoxy Matrix Product Data,* Hexcel Composites, 2013.

[89] ASTM International, *ASTM D2344 Standard Method for Short Beam Strength of Polymer Matrix Composite Materials and Their Laminates,* ASTM International, 2006.

[90] ASTM International, *ASTM D5687 - Standard Guide for Preparation of Flat Composite Panels with Processing Guidelines for Specimen Preparation,* ASTM International, 2007.

[91] M. May and S. Hallot, "An assessment of through-thickness shear tests for initiation of fatigue failure," *Composites: Part A,* vol. 41, pp. 1570-1578, 2010.

[92] A. Makeev, "Interlaminar shear fatigue behavior of glass/epoxy and carbon/epoxy composites," *Composites Science and Technology,* vol. 80, pp. 93-100, 2013.

[93] C. A. Cooper, S. R. Cohen, A. H. Barber and H. D. Wagner, "Detachment of nanotubes from a polymer matrix," *Applied Physics Letters,* vol. 81, p. 3873, 2002.

[94] P. Hansen and R. Martin, "DCB, 4ENF and MMB Delamination Characterisation of S2/8552 and IM7/8552, Final Technical Report," United States Army, European Research Office of the United States Army, London, England, 1999.

[95] B. Yu, R. Bradley, C. Soutis, P. Hogg and P. Withers, "2D and 3D imaging of fatigue failure mechanisms of 3D woven composites," *Composites: Part A,* vol. 77, pp. 37-49, 2015.

[96] E. Garcia, A. Hart, B. Wardle and A. Slocum, "Fabrication and Testing of Long Carbon Nanotubes Grown on the Surface of Fibers for Hybrid Composites," in *47th AIAA Structures, Structural Dynamics, and Materials Conference*, Newport, RI, 2006.

[97] S. Wicks, W. Wang, M. Williams and B. Wardle, "Multi-scale interlaminar fracture mechanisms in woven composite laminates reinforced with aligned carbon nanotubes," *Composites Science and Technology,* vol. 100, pp. 128-135, 2014.

[98] K. Ishiguro, R. Guzman de Villoria, S. S. Wicks, N. Yamamoto and B. L. Wardle, "Processing and Characterization of Infusion-Processed Hybrid Composites with In Situ Grown Aligned Carbon Nanotubes," in *50th AIAA/ASME/ASCE/AHA/ASC Structures, Structural Dynamics, and Materials Conference*, Palm Springs, CA, 2009.